NASA Contractor Report 4174

NASA-CR-4174 19880017784

Theoretical/Numerical Study of Feasibility of Use of Winglets on Low Aspect Ratio Wings at Subsonic and Transonic Mach Numbers To Reduce Drag

LIBRARY COPY

LANGLEY RESEARCH CENTER
LIBRARY, NASA
HAMPTON, VIRGINIA

John M. Kuhlman, Paul Liaw,
and Michael J. Cerney

GRANT NAG1-625
AUGUST 1988

FOR REFERENCE

NOT TO BE TAKEN FROM THIS ROOM

NF01798

NASA

NASA Contractor Report 4174

Theoretical/Numerical Study of Feasibility of Use of Winglets on Low Aspect Ratio Wings at Subsonic and Transonic Mach Numbers To Reduce Drag

John M. Kuhlman, Paul Liaw,
and Michael J. Cerney
West Virginia University
Morgantown, West Virginia

Prepared for
Langley Research Center
under Grant NAG1-625

National Aeronautics
and Space Administration

Scientific and Technical
Information Division

1988

THEORETICAL/NUMERICAL STUDY OF FEASIBILITY OF USE OF WINGLETS ON LOW ASPECT RATIO WINGS AT SUBSONIC AND TRANSONIC MACH NUMBERS TO REDUCE DRAG

SUMMARY

A numerical design study has been conducted to assess the drag reduction potential of winglets installed on a series of low aspect ratio wings at a high subsonic Mach number cruise design point of $M = 0.8$, $C_L \cong 0.3$. Wing-winglet and wing-alone design geometries have been obtained for wings of aspect ratios between 1.75 and 2.67, having a taper ratio of 0.2 and leading edge sweep angles ranging from 45° to 60°. Winglet length has been fixed at 15% of the wing semispan.

To assess the relative performance between wing-winglet and wing-alone configurations at the selected design point, the PPW nonlinear extended small disturbance potential flow analysis code has been utilized. This numerical model has proven in the present study to yield plausible transonic flow field simulations for the series of low aspect ratio wing and wing-winglet configurations selected. Predicted decreases in pressure drag coefficients for the wing-winglet configurations relative to the corresponding wing-alone planform are about 15% at the design point of $M = 0.8$, $C_L \cong 0.3$. Predicted decreases in wing-winglet total drag coefficients are about 12%, relative to the corresponding wing-alone design. Wing-winglet root bending moment coefficients are increased 5-7% relative to wing-alone cases. Longer winglets (25% of the wing semispan) yielded decreases in the pressure drag of up to

22% and total drag of up to 16.4%.

The predicted drag coefficient reductions in percent are comparable to reductions already demonstrated by actual winglet designs installed on higher aspect ratio transport type aircraft. Since low aspect ratio configurations have much lower lift-to-drag ratios, the overall drag force reduction for a low aspect ratio wing at fixed lift should be significantly larger than at higher aspect ratio. If realized, these reductions would significantly improve range or payload capability of a low aspect ratio configuration fitted with properly designed winglets. Also, the wing-winglet designs may be advantageous for supersonic flight, relative to a higher aspect ratio wing, since the winglet can be oriented to remain behind the Mach cone, and because the wing-winglet wing designs have less twist than the wing-alone configurations.

SYMBOLS

a	chordwise loading shape function parameter
A	aspect ratio, b^2/S
b	wing span
c	local chord
c_{av}	mean geometric chord
c_ℓ	section lift coefficient
C_B, C_{RBM}	wing root bending moment coefficient
C_D	drag coefficient
C_{Df}	friction drag coefficient
C_{Di}	induced drag coefficient
C_{Dp}	pressure drag coefficient
C_{Dtot}	total drag coefficient
C_L	lift coefficient
C_m	pitching moment coefficient
C_p	pressure coefficient
D	drag force

D_i	induced drag force
k	induced drag efficiency factor
L	lift force
ℓ	winglet length
q	dynamic pressure
S	wing area
x	chordwise coordinate
y	spanwise coordinate
z	vertical coordinate
α	angle of attack
ε	local geometric incidence angle
λ	taper ratio
Λ	wing leading edge sweep angle
ξ	fractional spanwise distance on winglet
Φ	velocity potential, or wing trailing edge sweep angle

INTRODUCTION

The winglet concept originally developed by Whitcomb[1] has proven to be an effective means of reducing aircraft induced drag through use of a nonplanar lifting system. The wing-tip mounted, nearly vertical winglet develops a normal force which alters the configuration spanload to diffuse the total circulation in the rolled up wing tip vortex and reduce the total energy of the vortex[2]. Also, toe out of the winglet allows the winglet normal force to develop a thrust component to reduce drag. Asai[3] has also shown the importance of the relatively short chord of the winglet to minimize the increased wetted area and resulting skin friction penalty.

The winglet concept has, to date, primarily been applied to relatively high aspect ratio, transport-type configurations (e.g., refs. 1,2,4). However, an early numerical study by Cary[5] indicated that larger reductions in induced drag force were obtainable at fixed lift for a given winglet as the aspect ratio

of the wing on which it was installed was reduced. In addition, increased wing sweep resulted in larger predicted reductions in induced drag. Another theoretical parametric study by Heyson, et al.,[6] found that winglet benefits, relative to a wing tip extension having the same bending moment increase, increased as the wing aspect ratio decreased for a series of straight and swept, tapered and untapered wings. That is, the induced drag efficiency factor was increased as aspect ratio decreased, while holding the percent increase in bending moment fixed. These early numerical results indicate that there should be a greater potential for induced drag force reduction and improvements in the cruise performance for the low aspect ratio, high-sweep wings typical of fighter aircraft than for the transport-type wings which have been emphasized previously. The present work has been undertaken based on the premise that the drag reduction capability of winglets which has been proven at high aspect ratio should logically carry over to winglets designed for wings of lower aspect ratio.

One existing wing-winglet design for a relatively low aspect ratio wing is that of the HiMAT research aircraft[7]. This configuration has an aspect ratio 3.85 wing fitted with wing tip fins, or winglets, which are 23 percent of the wing semispan in length. The winglet root chord is equal to wing tip chord. These winglets were found to reduce induced drag, but not by the amount predicted by the design method employed, which was based upon linear theory. Also, performance was degraded at the high lift, transonic maneuver design point, apparently due to extensive flow separation on the winglets. This is at least partially the result of the linear design methods which were utilized in the winglet design[7]. More recent nonlinear analyses[8] using the PPW code[9-11] for the HiMAT configuration have matched actual flight test data

quite well. Also, Hackett[12] has recently presented results of a preliminary study wherein a simple untwisted, vertical vane was used to reduce drag of a low aspect ratio delta wing. Thus, there appear to be very few previous instances where winglets have been utilized on low aspect ratio wings.

The present effort is a preliminary design study to further assess the potential for winglets to reduce drag of low aspect ratio, high sweep fighter-type wings at a high subsonic Mach number. The nonlinear transonic potential flow analysis code PPW, developed by Boppe[9,10,11], has been utilized to predict transonic performance for several wing-winglet and wing-alone planforms at a Mach number of 0.8 and lift coefficient of 0.3. Initial wing-winglet and wing-alone design geometries have been generated for attached flow using two existing linearized theory aerodynamic design codes[13-15]. Winglet and wing tip geometries have then been altered to reduce wing tip incidence and increase winglet toe out in an effort to improve the predicted performance by weakening shocks on the winglet and wing tip. To date no assessment has been made of performance of these configurations at supersonic Mach numbers, or of the effects of winglets on configuration stability or agility. Also, the present work has investigated only a relatively small number of variations of winglet planform, over relatively limited ranges of Mach number and lift coefficient. For example, performance of a downward-pointing winglet has not been studied due to concerns about ground clearance. Pylons have not been studied because they have significantly less potential to reduce induced drag.

DESIGN APPROACH

General Philosophy

The present work has been conducted as an initial step to better determine the potential for winglets to reduce the drag of low aspect ratio fighter type wings at a high subsonic Mach number. The basic philosophy of the work was to use as simple a set of configuration geometries and analysis tools as were practical to still allow meaningful conclusions to be drawn.

At the simplest level, consider the induced drag efficiency factor, k, defined as the ratio of induced drag coefficient for an elliptically loaded planar wing to the induced drag coefficient of the optimal nonplanar wing-winglet configuration having an equal projected span at equal lift coefficient. The induced drag efficiency may be calculated for a planar wing fitted with a vertical winglet or endplate using a Trefftz plane model, as shown in Fig. 1a. These results have been taken from refs. 16 and 13, and are identical to results of another numerical model by Lundry and Lissaman[17]. The Trefftz plane model predicts the efficiency factor increases linearly with winglet height, ℓ. To a good approximation, k-1 is equal to the ratio of winglet length to semispan. Thus, for typical winglet lengths of 10-20% of the wing semispan, the potential percentage reduction in induced drag coefficient, 1-1/k, is 9-17%. In Fig. 1a, k has been calculated assuming that the nonplanar configuration has the same projected span as the planar wing; hence the nonplanar configuration will have a longer actual length. For results of the present study comparisons between wing-alone and wing-winglet performance have instead been made by holding the wing area fixed, and allowing the wing-winglet projected span to increase slightly (3.9%). The Trefftz plane model predicts k to be independent of both C_L and wing aspect

ratio.

Assuming then that wing-winglet geometries could be designed to develop the required spanload independent of wing aspect ratio, the following simple discussion demonstrates why a winglet would have a larger impact for a low aspect ratio wing. The optimum induced drag coefficient, including nonplanar effects, is given by

$$C_{Di} = C_L^2/(\pi A k) \qquad (1)$$

Thus, ignoring the dependence of lift curve slope on A, and holding C_L fixed, it is seen that C_{Di} will vary inversely with Ak. Applying the far field results of Fig. 1a, where k is predicted to be independent of wing aspect ratio, it is seen that the percent reduction in induced drag coefficient for a fixed value of $\ell/(b/2)$ should not vary with wing aspect ratio. This leads to the conclusion that the actual reduction in induced drag force at fixed lift would be significantly larger for a winglet installed on a low aspect ratio wing, since the lift-to-drag ratio would be smaller.

Equation (1) may also be written in dimensional form as

$$D_i = (L/b)^2/(\pi\, qk) \qquad (2)$$

where q is dynamic pressure. Thus it is seen that the induced drag is dependent on the square of the ratio of lift-to-span. This equation may be interpreted as indicating that the induced drag is independent of aspect ratio. However, additional structural considerations would indicate that a lower aspect ratio wing of equal structural weight could safely develop a higher wing loading than a high aspect ratio wing. Even ignoring this structural advantage, and simply requiring a constant wing loading, it is seen that for a

given configuration weight, as aspect ratio is decreased, span must decrease, thereby increasing induced drag by the span ratio squared at fixed lift (equn. (2)).

In Fig. 1b, these simple arguments have been carried one step further, where the potential effect of winglets on the drag polar has been estimated for a fighter configuration[18]. Wing aspect ratio is 2.2, and the configuration drag data are for M = 1.6; these drag data have been used for illustration purposes. The actual configuration drag data have been approximated by $0.028 + 0.3\ (C_L)^2$ in Figure 1b. Also shown in Fig. 1b are three estimated drag polars for winglets which reduce the induced drag by 10, 20, and 30%, corresponding approximately to $\ell/(b/2) = 0.11$, 0.25, and 0.43, respectively. Percent total drag reductions at $C_L = 0.2$ are approximately 3, 6, and 9% for the three different winglet lengths. These percent drag reductions increase to 6, 13, and 19% at $C_L = 0.4$ and 9, 18, and 27% at $C_L = 1.0$.

It should be noted that the potential drag reductions predicted in this example are expected to be optimistic, especially at high lift, since no additional drag penalties were included for the added wetted area or added wave drag due to any shocks on the winglets or adverse mutual interference between wing and winglet. In addition, it is expected that any fixed winglet geometry would be unable to develop the required loading at a configuration lift coefficient of 1.0, but would instead experience separated flow. Further, winglets must also require a stiffer wing structure. However, this application of a simple far field minimum induced drag calculation highlights the very significant potential of properly designed winglets to reduce drag. In particular, the potential percentage reduction in total configuration drag coefficient at high lift coefficients approaches the percentage reduction in

induced drag coefficient (Fig. 1b), which is directly proportional to winglet length (Fig. 1a).

In light of this very large potential for drag reduction, for the present preliminary study, existing linear theory design methods[13-15] have been selected as being adequate for a preliminary study. These initial linear designs have then been modified as required in areas of high loading. Similar methods were used previously in the design of a high aspect ratio transport wing-winglet wind tunnel model[19-20].

Planform Choices

Choices of both wing and winglet planform in the present study have been influenced by four basic considerations. First, an effort has been made to study a range of wing-winglet planforms that might be representative of typical wing aspect ratio and leading edge sweep values for present generation fighter aircraft[21-23] and next generation fighter aircraft[24-27]. Second, concerns over the ability of the linear design methodology utilized to generate wing-winglet geometries which developed realistic enough wing and winglet loadings to permit converged, essentially attached flow solutions to be obtained from the PPW code at the selected high subsonic Mach number cruise design point also influenced the range of wing and winglet planforms selected. Third, difficulties encountered in obtaining converged transonic flow solutions with an early version of the PPW code for a wing of aspect ratio three[23] influenced early wing planform choices. It has since been learned that this early problem has been alleviated by implementation of a different crude grid developed by Waggoner[28]. Related to this issue, limitations of the PPW code have influenced the range of winglet geometries studied. Finally, it has also been possible to investigate trends in the predicted induced drag reduction

versus wing aspect ratio or leading edge sweep.

Based on these considerations, an initial series of design studies have focused on the series of 8 trapezoidal wing planforms defined in Table 1. These wings have aspect ratios ranging from 1.75 to 2.67, leading edge sweep angles between 45°-60°, and a constant value of taper ratio of 0.2. These wing planform values were believed to bracket current and next-generation fighter configurations[21-27]. Also, the range of wing aspect ratios selected was believed to be adequate to judge trends in the predicted drag coefficient levels.

Table 1. Wing Planform Configurations

	A	Λ	Φ	λ
A	2.63	50°	10°	0.2
B	2.67	45°	0°	0.2
C	1.75	50°	-18.4°	0.2
D	1.75	55°	- 5.5°	0.2
E	1.75	60°	11.8°	0.2
F	2.20	45°	-12.0°	0.2
G	2.20	50°	- 1.2°	0.2
H	2.20	55°	12.2°	0.2

For this initial study, a trapezoidal winglet planform was selected for each wing, where winglet length, cant, taper ratio, and leading edge sweep were the same for all configurations. Winglet trailing edge sweep was varied as required to maintain a constant ratio of winglet area to wing area. Winglet length was fixed at 15% of the wing semispan, so that the far field drag analysis predicts each configuration should have the potential to achieve nominally a 13% reduction in induced drag when configuration projected span

is held fixed. Winglet leading edge sweep was fixed at 50°; wing leading edge sweep angles bracket this value. All winglets so defined have total areas equal to 2.25% of the basic wing area. These chosen winglet length and area values are consistent with those used in previous winglet applications[1,3,4,7,21]. Other winglet planform details have been selected primarily based upon Whitcomb's original recommendations[1], aimed at reducing adverse mutual interference effects. Thus, winglets have been located in an aft position, behind the wing tip airfoil shoulder. Since all wing and winglet configurations have utilized an NACA 64A006 thickness distribution, winglet root chord was fixed at 60% of the wing tip chord. Cant was fixed at 15° and has not been varied in the present study because the version of PPW used utilizes a rectangular intermediate grid and a vertical winglet computational orientation. Winglet taper ratio has been fixed at 0.5 in the current work due to concerns about inadequate grid resolution in the PPW code for smaller winglet tip chords. (Essentially, a minimum of 2 or 3 crude grid points must fall on each computational airfoil station for accurate interpolation between the different embedded grids.)

Design Point

Actual fighter aircraft designs are the result of tradeoffs between a number of competing design points or mission requirements[29], which have not been addressed in the present study. Instead, for the present work, a cruise condition at a high subsonic Mach number has been selected for all designs, based on the belief that existing fighter aircraft typically cruise at as high a Mach number as possible without a significant drag-rise penalty (i.e., $0.7 \leq M \leq .9$ at cruise). Thus, a single value of $M = 0.8$ has been selected as the design Mach number value. Also, based on typical and maximum wing loadings

and wing areas for existing lightweight fighters[21], typical configuration lift coefficients at M = 0.8 at an altitude of 30,000 feet range from about 0.2 for a lightly loaded, "clean" configuration, to about 0.4 for a very heavily loaded configuration. Thus, a single design value of lift coefficient of $C_L = 0.3$ has been selected for the present study since it falls in the appropriate range, but is also high enough so that a significant potential for total drag reduction exists (an order of magnitude of 10% including the fuselage, estimated from Fig. 1b).

Design Methodology

An overview of the numerical design process and design tools utilized in the present work will now be given. Additional details may be found in the thesis by Liaw[30]. First, for each configuration of interest the wing planform, design point, and winglet orientation and planform are fixed as described above. Then, a linear aerodynamic design code is utilized to generate initial attached flow theory wing and winglet geometry input for the more sophisticated nonlinear transonic analysis code. Also, cylindrical fuselage definition is added at this point, where fuselage diameter is 25% of the wing semispan. Fuselage length is 10.5 times the wing semispan, to approximate an infinite cylinder. The PPW analysis code[9-11], which includes modeling capability of body, thickness, viscous, and weak shock effects, is then utilized to analyze configuration performance at the transonic design point. The original linear theory winglet design geometry is also modified to improve the configuration performance as predicted by the PPW analysis code. In particular, wing tip and winglet root incidence values have been altered to weaken shocks predicted by the nonlinear analysis code, to reduce wave drag.

One of the linear design codes[13,14] utilizes a vortex lattice near field

model and a high order panel wake model to obtain the wing-winglet camber surface for minimum induced drag at the chosen design point Mach number and lift coefficient. Wing and winglet planforms, as well as winglet cant are specified, as is an assumed chordwise loading shape function. For preliminary designs presented herein, a rectangular chord loading has been assumed. The formulation utilized in this program requires a continuous spanwise chord distribution; hence, a high-sweep panel is required on the winglet near the root. Otherwise the resulting camber surface is not smooth.

The second design code[15] yields twist distributions for up to ten symmetrical or asymmetrical planforms for minimum total drag at the chosen design point. This code uses a vortex lattice model (ref. 31), and experimental profile drag data at appropriate Reynolds numbers for the chosen wing and winglet airfoils, along with sweep theory. The assumed linearly lofted geometries are simpler and more representative of actual wing fabrication techniques than those generated by the first design code. Also, this code permits design of geometries which have discontinuous changes in chord, such as would be of interest at a wing-winglet juncture.

Both design programs have been modified to generate output files of linear theory optimum wing and winglet upper and lower surface coordinates in the format required for the PPW nonlinear analysis code. A second file in Hess format is also generated for interactive plotting of the resulting geometry[32]. For most of the results of the present study, the first design code[13,14] has been utilized.

The PPW nonlinear transonic analysis code[9-11] solves a finite difference representation of an extended small disturbance form of the nonlinear full potential equation, by a relaxation method. The extensions to the classical

transonic small disturbance potential flow equation are nonlinear terms which appear in the full potential equation, which improve the ability to capture swept shocks on the wing and winglet.

A unique feature of the code is the utilization of multiple, nested, rectangular grids with fine resolution in regions of large flow gradients. A crude global grid is utilized along with finer individual grid systems surrounding each aircraft component (wing, winglet, fuselage, pod, or pylon). All fine grid systems are rectangular and evenly spaced, and overlap several grid points in the crude global grid. The crude grid is rectangular, but is stretched to infinity. Variation in flow field potential is communicated from one grid system to another by interpolation. Use of these multiple, nested grids allows good resolution of the flow field details around a winglet without requiring a very fine grid away from the winglet. In addition, no complex grid generation is required, so that configuration components can very easily be added or removed to study interference effect trends.

The small disturbance formulation has also been used to simplify boundary conditions, which are applied at the nearest neighboring computational grid points. Boundary conditions are corrected by small disturbance theory for variation due to differences in location of the physical boundary and the computational boundary.

A two-dimensional, compressible Bradshaw strip boundary layer calculation may be performed on the wing surfaces using simple sweep theory, and interacted with the outer potential flow. The boundary layer displacement thickness is calculated, and is used to modify the wing surface slope boundary conditions. No boundary layer calculations are performed on the fuselage, winglet, pods, or pylons. An empirical curve fit is used to estimate

displacement thickness in the cove region of a supercritical airfoil.

Configuration forces and moments and spanload distributions are calculated by direct numerical integration of the pressure coefficient distributions. Viscous effects are estimated for the fuselage and winglet using a flat plate skin friction correlation corrected for compressibility effects.

RESULTS

Results of the present preliminary design study will be presented by first describing the linear theory design geometries, and required modifications to these geometries to obtain successfully converged nonlinear transonic flow results at the chosen design point. Then the transonic flow results will be presented; first convergence will be discussed, followed by comparisons of the predicted performance levels, both at the design point, and at off-design conditions.

Linear Theory Designs

The majority of results obtained in the present work have used the first design code[13,14] to define minimum induced drag wing-alone and wing-winglet camber surfaces for each of the eight wing planforms listed in Table 1 at the selected design point. Seven of the resulting incidence distributions for the optimum wing-alone geometries are shown in Fig. 2a, while similar incidence plots for the wing-winglet configurations are shown in Fig. 2b. Optimum wing incidence is characterized by a gradual washout, except in the vicinity of the wing root and wing tip where much more rapid washout is observed. In contrast, wing-winglet incidence follows the wing-alone distribution inboard but shows a dramatic increase in wing tip incidence, while most of the winglet is toed out (negative incidence in Fig. 2b). Also note that the winglet root airfoil is toed in somewhat. This is accompanied by a rather large amount of

camber. These unexpected kinks in wing tip and winglet root incidence were found not to be a result of any poor paneling choices in the linear theory design code. Also, such incidence kinks were not observed in designs obtained for the higher aspect ratio wing-winglet configuration of refs. 19 and 20. These linear theory wing-winglet designs have been modified by removing the highly cambered, high-sweep panel at the winglet root, as well as the increase in incidence at the wing tip. The resulting modified incidence distributions are shown in Fig. 2c, while the original and modified winglet geometries are shown in Fig. 3 for case G. Typical wing-alone design geometries are shown in Fig. 4, while examples of the resulting wing-winglet geometries for two of the $\Lambda = 50°$ wings are shown in Fig. 5. Similar geometry definition has been given for the remaining wing-winglet configurations and typical wing-alone configurations in ref. 30.

PPW Analysis Code Convergence Results

As an initial step in utilizing the PPW nonlinear transonic code to analyze performance of low aspect ratio wing-winglet configurations, the convergence capabilities of this program were studied at the design point, for the eight trapezoidal wing planforms described in Table 1. This was done partially because of concern over convergence difficulties encountered previously by others at low aspect ratio[23]. A second purpose of this study was to establish the viability of using the simple linear theory design methods described above to define the initial low aspect ratio wing-alone and wing-winglet design geometries.

All eight of the wing-alone configurations designed by the linear theory design code were found to yield successfully converged, realistic flowfield solutions at $M = 0.8$, $\alpha = 0.5°$ using the PPW code, without any alteration of

geometry, when no interaction of the viscous boundary layer was used for 160 iterations (100 crude grid, followed by 60 crude-fine grid iterations). Here the term "realistic" is used to indicate a PPW solution without any significant oscillations in the surface pressure coefficient distributions. Angle of attack has been increased by 0.5° because this often has been found to provide better agreement with experimental lift values[11]. Maximum changes in the flow field potential ranged from 1.7×10^{-5} to 6.5×10^{-5}, as shown in Table 2. When wing viscous boundary layer interaction was included, convergence difficulties were observed at the lowest aspect ratio for the higher wing sweep angles. Wing E ($A = 1.75$, $\Lambda = 60°$) would not converge, while the PPW solution for wing D ($A = 1.75$, $\Lambda = 55°$) at $\alpha = .5°$ also diverged, but converged at $\alpha = 0°$. Maximum changes in solution potential with the interacted boundary layer using 300 iterations (100 crude grid and 200 crude-fine grid iterations) ranged from 5.7×10^{-6} to 6.6×10^{-5} for the seven wing-alone configurations.

Table 2. PPW Code Convergence at $M = 0.8$, $C_L \cong .3$ for Wing-Alone Configurations

Config.	Wing A	Wing Λ	160 iterations, no BL $\Delta\Phi_{max}$	300 iterations, with BL $\Delta\Phi_{max}$
A	2.63	50°	5.53×10^{-5}	1.07×10^{-5}
B	2.67	45°	5.18×10^{-5}	1.32×10^{-5}
C	1.75	50°	6.29×10^{-5}	6.64×10^{-5}
D	1.75	55°	5.81×10^{-5}*	5.72×10^{-6}*
E	1.75	60°	1.87×10^{-5}	-------
F	2.20	45°	6.51×10^{-5}	1.46×10^{-5}
G	2.20	50°	1.72×10^{-5}	1.39×10^{-5}
H	2.20	55°	5.53×10^{-5}	6.98×10^{-6}

* $\alpha = 0°$; all other cases at $\alpha = 0.5°$

Thus, it has been found that converged, realistic transonic flow field solutions may be obtained from the PPW code at $M = .8$, $C_L \cong .3$ for a series of trapezoidal low aspect ratio wings of $1.75 \leq A \leq 2.67$, $45° \leq \Lambda \leq 55°$, with $\lambda = 0.2$, where wing camber and twist has been defined by linear theory.

However, much greater difficulty was encountered in obtaining realistic, converged nonlinear PPW solutions for the eight wing-winglet configurations. No converged solutions were obtained for any of these geometries when used exactly as specified by the linear design code. However, converged, realistic solutions were obtained for all but two wing-winglet configurations when the original geometries were modified to reduce loading at the wing tip and winglet root, by omitting the wing-tip incidence kink and the highly swept, highly cambered, toed in winglet root airfoils. Instead, the wing tip and winglet root airfoils were defined using the airfoils inboard on the wing or upward on the winglet. More details of these geometry modifications have been given in ref. 30. The resulting maximum changes in velocity potential for the modified wing-winglet geometries are given in Table 3. The levels of convergence for the higher and intermediate aspect ratio wing-winglet configurations are comparable to those observed for the corresponding wing-alone configuration. It is noted that convergence, as judged by reductions in the change in velocity potential, is a relatively slow process in the PPW code. Even greater difficulty was experienced in obtaining converged PPW solutions for the $A = 1.75$ wing-winglet configurations than for the wing-alone cases. This is believed to most likely be due to inadequacy of the linear design methodology at the lower aspect ratios rather than to any inherent limitation to the PPW code itself. This is based upon further results

Table 3. PPW Code Convergence at M = 0.8, $C_L \cong .3$ for Wing-Winglet Configurations

Config.	Wing A	Wing Λ	160 iterations, no BL $\Delta\Phi_{max}$	300 iterations, with BL $\Delta\Phi_{max}$
A	2.63	50°	5.37×10^{-5}	1.04×10^{-5}
B	2.67	45°	5.95×10^{-5}	1.07×10^{-5}
C	1.75	50°	--------	--------
D	1.75	55°	1.09×10^{-4}*	--------
E	1.75	60°	--------	--------
F	2.20	45°	6.70×10^{-5}	1.57×10^{-5}
G	2.20	50°	7.07×10^{-5}	1.39×10^{-5}
H	2.20	55°	5.87×10^{-5}	--------

* $\alpha = 0°$; all other cases at $\alpha = 0.5°$

presented in ref. 30, where the winglet for wing C (A = 1.75, Λ = 50°) was toed out somewhat near the wing root, and convergence was obtained.

PPW Analysis Code Performance Comparisons at Design Point

The potential for winglets to reduce drag for low aspect ratio wings at a transonic cruise design point has been assessed by comparing the lift-to-drag ratios computed by the PPW code for each wing-winglet configuration with the calculated L/D for the corresponding optimum wing-alone configuration at essentially the same lift at the design point of M = .8, $C_L \cong 0.3$, as shown in Table 4. The percentage differences between calculated wing-alone and wing-winglet lift coefficients have also been shown. Lift coefficients have generally been matched to within approximately ± 1%. All lift and drag coefficients in this comparison have omitted the fuselage force coefficients, so comparisons have been made between the wing plus winglet force coefficients and the wing forces for the corresponding wing-alone configuration. All lift and drag force coefficients have been calculated using the configuration wing

area as the reference area. Thus force coefficient ratios are directly interpreted as ratios of forces. Note that, as previously mentioned, the wing-winglet configurations have slightly larger areas (2.25%) and projected spans (3.88%) than the corresponding wing-alone geometries. Thus, the far field theory predicts a potential for a 16.9% reduction in induced drag when the projected span is allowed to vary and the wing area is used as the wing-winglet reference area. If projected span is held fixed, then the predicted reduction in induced drag is 13%.

Predicted increases in lift-to-pressure drag (induced drag plus wave drag) are between 13.1 and 16.7% for runs without any boundary layer interaction for 160 iterations. No clear trend in predicted percentage L/D increases is observed as wing aspect ratio or leading edge sweep angle is varied. When the wing boundary layer interaction is included and 300 iterations are used, calculated wing-winglet lift-to-pressure drag is 14.6 to 15.8% higher than for the corresponding wing-alone configuration at essentially the same lift. For these four configurations, calculated wing-winglet lift-to-total drag is 11.5 to 13.3% higher than calculated wing lift-to-total drag at the same lift. Again there is no apparent variation of the predicted percentage L/D increases with wing aspect ratio or wing leading edge sweep.

The PPW code was modified to use the calculated wing and winglet spanloads to calculate a bending moment coefficient about the wing root to allow some comparisons of the structural penalty due to the winglet. For the four configurations for which 300 iterations, interacted boundary layer solutions have been obtained, this calculated bending moment coefficient at the design point was increased 5-7% for the wing-winglet case relative to the

corresponding wing-alone case[30]. These percentage increases in bending moment are of the same order as those calculated by Heyson, et al.[6] for winglets on wings of similar aspect ratio.

Typical calculated upper surface wing-alone pressure coefficient distributions are shown in Fig. 6 for the A = 2.63 and A = 2.20, Λ = 50° configurations using 160 iterations without boundary layer interaction. Results for the other wing-alone configurations all look quite similar[30]. The corresponding wing upper surface pressure coefficient distributions for the A = 2.63 and A = 2.20, Λ = 50° wing-winglet configurations, again for 160 iterations and no boundary layer interaction, are shown in Fig. 7. They are nearly identical to the wing-alone results except near the aft end of the wing tip in the vicinity of the winglet. Here the presence of the winglet results in larger velocities and more negative pressure coefficient values. Wing pressure distributions for all other wing-winglet configurations appear quite similar[30]. Examples of the calculated winglet pressure coefficients at ξ = 0.163, 0.488, 0.650, and 0.975, where ξ is the fractional distance from the winglet root to the winglet tip, are shown for the same two wing-winglet solutions in Figs. 8 and 9. Similar results have been obtained for all other winglets.[30]. Smooth, nearly rectangular winglet pressure distributions are obtained at A = 2.63, but a shock is observed near mid chord over the lower 50% of the winglet at A = 2.20. In addition, a suction peak is observed on the inboard surface at the winglet leading edge near the winglet root, indicating that this winglet should be toed out more. For the assumed a = 1.0 rectangular chord loading there also appears to be a trailing edge shock everywhere along the winglet ($C_p^* \cong -.4$ at M = .8). Winglet pressure coefficients have been shown in Figs.

Table 4. PPW Code Predicted Lift-to-Drag Increases Due to 0.15(b/2) Winglets at M = 0.8, $C_L \cong 0.3$

Config.	Wing A	Wing Λ	160 iterations, no BL C_L/C_{Dp} Increase	160 iterations, no BL ΔC_L	300 iterations, with BL C_L/C_{Dp} Increase	300 iterations, with BL C_L/C_{Dtot} Increase	300 iterations, with BL ΔC_L
A	2.63	45°	13.1%	0.9%	14.9%	11.5%	-0.8%
B	2.67	50°	14.4%	-1.87%	15.0%	11.8%	-1.2%
D	1.75	55°	16.4%*	-.02%*	---	---	---
F	2.20	45°	16.5%	-.99%	15.8%	13.3%	-0.9%
G	2.20	50°	16.7%	.05%	14.6%	12.1%	0.7%
H	2.20	55°	15.7%	-1.23%	---	---	---
C	1.75	50°	14.9%	-.20%	---	---	---

* $\alpha = 0°$; all other cases at $\alpha = 0.5°$

8 and 9 for both the 160 iterations, no boundary layer solutions and the better-converged, more realistic solutions for 300 iterations with the interacted boundary layer. Very little difference is observed at A = 2.63. However, mid-chord shocks are weakened and moved slightly aft, and trailing edge shocks are weakened slightly, for the solution including the interacted boundary layer for the more heavily loaded winglet on the A = 2.20 wing. Similar trends have been seen for the effect of including the boundary layer on shock location for transport wing configurations in ref. 28.

Designs using a = 0.8 and a = 0.9 chord loadings were successful in reducing the severity of the observed trailing edge pressure recovery. However, mid-chord winglet shocks were strengthened so that overall predicted drag levels were not greatly different than those computed using

the rectangular chord loading. This is seen in Fig. 10, where the predicted drag polars and (L/D) versus C_L at M = 0.8 are shown for six different design geometries using wing planform F (A = 2.20, Λ = 45°). Results are shown for three wing-alone designs using a = 1.0, 0.9, and 0.8 chord loadings, and three corresponding wing-winglet designs, again using a = 1.0, 0.9, and 0.8. Calculated pressure distributions are shown in Fig. 11 for the three wing-winglet designs at α = 0°, $C_L \cong 0.27$. Pressure recovery on the upper surface is most gradual for the a = 0.8 design geometry. For this geometry the Bradshaw strip boundary layer calculation in PPW predicts no boundary layer separation on the wing upper surface. For a = 1.0 or 0.9 boundary layer separation is predicted near the wing tip at (x/c) = 0.98-0.99.

Insight into the quality of the linear theory wing designs at the selected design point, as well as into the effects of the wing-winglet geometry modifications, has been gained through inspection of the predicted spanload distributions. Here, spanload has been presented as $c_\ell c/(c_{av}C_L)$. As shown in Fig. 12, the linear theory wing-alone designs analyzed in the PPW code yield essentially an elliptical spanload for the isolated wing case; calculated span efficiency factors are very close to the optimum value of 1.0 (e = 0.999 for all isolated wings). The linear theory design code spanload was also elliptical. Addition of the fuselage shifts the loading outboard. This is seen in Fig. 13 to be due to the lift loss due to the fuselage. Typical calculated span efficiency factors for these wing-body spanloads are $e \cong 0.97$ to 0.98.

Corresponding wing-body-winglet spanloads at M = 0.8, α = 0.5° are shown in Fig. 14. Again, spanload is reduced due to the fuselage, and the

resulting loading is shifted outboard relative to the isolated wing case. However, there are also indentations in the calculated spanload distributions at the wing tip and at the winglet root which are the result of the geometry modifications in these regions. Essentially, these geometry modifications were required to unload the wing tips and winglet root below the levels required by the linear theory design methodology. This had the effect of maintaining a flow field in the wing-winglet juncture which was only slightly supersonic, so that any shocks which resulted were weakened.

Further examples of calculated pressure coefficient distributions obtained for a longer winglet of length equal to 0.25(b/2) on wing planform H ($A = 2.20$, $\Lambda = 55°$) have been presented in Fig. 15. This configuration has a potential for a 25.4% reduction in induced drag coefficient relative to the shorter span wing-alone configuration, based on the far field theory of refs. 17 and 13. Winglet leading edge sweep is 45°, taper ratio equals 0.5, and cant is 15°. The design process and resulting geometry both were quite similar to those for the shorter 0.15 (b/2) winglet configurations, with the exception that winglet twist had to be altered by trial-and-error to obtain converged, smooth pressure coefficient solutions[30]. Winglet airfoils were toed out more at the winglet root, but toed in more near the winglet tip, and wing tip incidence was reduced while wing root incidence was increased relative to the linear theory design values ($\Delta\varepsilon_{\text{wing root}} = 0.5°$, $\Delta\varepsilon_{\text{wing tip}} = -0.5°$, $\Delta\varepsilon_{\text{winglet}} = -1.6°, -0.6°, 2.7°, 4.6°$)[30]. This solution is at $M = 0.8$, $\alpha = 0.5°$ for 300 iterations with the interacted boundary layer. For this run, $\Delta\Phi_{max} = 3.43 \times 10^{-5}$, and wing-winglet lift coefficient is 0.2% low relative to the wing-alone results[30]. The calculated lift-to-pressure drag ratio is increased 19.4% relative to the wing-alone case, while

calculated wing-winglet lift-to-total drag ratio is increased 15.4% compared to the wing-alone case[30]. Much smaller drag reductions at equal lift, of 14.9% in C_{Dp} and 11.9% in C_{Dtot} have been computed for a lower sweep (30°), long winglet; this is due to the occurrence of strong shocks on the inboard winglet surface (Fig. 16) which results from a larger interference effect for the lower sweep winglet. Thus, it appears that winglet leading edge sweep angle should not be significantly lower than the leading edge sweep angle of the wing, consistent with Whitcomb's original findings for higher aspect ratio wings[1].

PPW Predicted Performance - Off Design

The calculated performance benefits of approximately a 15% increase in wing-winglet lift-to-pressure drag and a 12% increase in wing-winglet lift-to-total drag for all configurations, at the design point of M = 0.8, $C_L \cong 0.3$, is very significant. However, it is also of interest to be able to quantify the wing-winglet performance benefits at off-design conditions. Such performance predictions versus angle of attack at M = 0.8 have been obtained in the current study for all wing-alone and wing-winglet configurations for which converged wing-winglet solutions were obtained (wings A, B, F, and G). In addition, predicted performance variation versus Mach number has been studied for the A = 2.63, Λ = 50° wing-winglet configuration (wing A).

Predicted performance of wing-alone and wing-winglet configurations A, B, F, and G at M = 0.8 versus angle of attack is summarized in Figs. 17-20, respectively. Shown are the lift, pitching moment, and wing root bending moment coefficients versus angle of attack, as well as the drag polar and L/D versus C_L. All calculated PPW force and moment coefficients

presented in these figures have been presented in tabular form in the Appendix. Generally, performance results for all four configurations look similar, except of course, that the drag coefficients are higher and L/D is lower for the lower aspect ratio configurations (A = 2.20; cases F and G). Figure 21 summarizes the predicted performance at M = 0.8 for the long, 45° sweep winglet installed on wing H (A = 2.20, Λ = 55°).

For all ten configurations (five wing-alone and five wing-winglet geometries) the lift coefficient, pitching moment coefficient and wing root bending moment coefficients vary essentially linearly with angle of attack. Lift coefficients for wing-winglet configurations are typically slightly lower (order of 1%) than for the corresponding wing-alone configuration at the same angle of attack. This may be the result of the geometry modifications at the wing tip and winglet root which were required to limit the shock strengths in the juncture regions of all wing-winglet configurations. Lift curve slopes are typically slightly greater for wing-winglet configurations than for the corresponding wing-alone case. Converged PPW solutions could not be obtained for any of the wing-winglet configurations at higher angles of attack than are shown in the figures or Appendix. Generally, this inability to obtain converged wing-winglet solutions occurred at C_L only slightly larger than 0.3 ($\alpha \cong 1°$). Note that the results shown at higher C_L values in Fig. 17 for wing-winglet configuration A were only obtained after a trial-and-error alteration of the wing tip and winglet root geometry as shown in the Appendix to further unload these regions at the higher overall lift levels.

Pitching moment coefficients calculated about the wing apex are not altered greatly by the winglets, but are slightly more negative. Wing root

bending moment coefficient, on the other hand, is significantly increased by the addition of the winglets. Wing root bending moment coefficients have been calculated by integrating the PPW spanloads, as explained in ref. 30. Generally, at the design point, wing-winglet configurations A-G have from 5.5 to 6.7% larger values of C_B than for the corresponding wing-alone geometry, while the longer winglets (0.25 (b/2)) result in a 10-11% increase in wing root bending moment coefficient. Similar percent increases are observed in Figs. 17-21 at other lift levels. The predicted drag polars of all wing-winglet configurations are shifted to lower drag relative to the corresponding wing-alone case, with a resultant increase in L/D at the same C_L.

The effect of incidence on the normalized spanload, $c_\ell c/(c_{av}C_L)$, is shown in Fig. 22 at M = 0.8 for wing-winglet configuration A (wing A = 2.63, Λ = 50°). Generally as α is increased the loading is increased inboard and decreases outboard both on the wing and on the winglet. The pressure coefficient distributions on the wing and winglet of configuration A at M = 0.8 for varying α are summarized in Fig. 23. As α is increased a suction peak develops near the leading edge of the winglet near the winglet root.

Off design performance at varying Mach number has been assessed only for wing-alone and wing-winglet configurations A (wing A = 2.63, Λ = 50°). Detailed performance predictions versus angle of attack for this configuration are presented in Figs. 24 and 25 at M = 0.7 and 0.75 respectively. Comparing Figs. 17, 24 and 25, as Mach number is increased, C_L, C_m, and C_B are all increased between $0.7 \leq M \leq 0.8$. Also, predicted drag coefficient actually decreases between M = .7 and .8, so that (L/D)

increases as Mach number is increased in this range.

Off design performance for these configurations at Mach numbers above the design Mach number has also been addressed, as summarized in Figs. 26-28. Typical wing upper surface pressure distributions for the wing-winglet configuration are shown in Fig. 26 at $\alpha = -1^\circ$ or -1.5° for Mach numbers up to 0.95, while typical winglet pressure coefficient distributions are shown in Fig. 27 for the same range of Mach numbers. For these results, $C_L \cong 0.2$; solutions at higher lift levels could not be obtained at the highest Mach number. As would be expected, winglet shock strength is increased as Mach number is increased, while at the same time a shock also develops on the wing upper surface. An interesting double shock pattern is predicted at M = 0.95 near the mid-span of the winglet (Fig. 27). The effect of this increased shock strength on calculated drag at a constant lift coefficient is shown in Fig. 28. Both wing-alone and wing-winglet predicted drag coefficients are shown for varying Mach number at fixed values of lift coefficient of $C_L = 0.3$, 0.25, and 0.2. These curves have been obtained by first generating drag polars at each Mach number, and then cross-plotting these results. It was not found to be possible to obtain successfully converged solutions for the wing-alone geometry above M = 0.825, and the maximum lift coefficient levels for which converged results could be obtained for the wing-winglet configuration were found to gradually decrease as Mach number was increased. It is not known whether these convergence problems were a rough indication that the actual flow field would likely experience shock-induced flow separation, or whether they were instead due to the PPW finite difference formulation. In spite of these difficulties, at $C_L = 0.2$ and 0.25 there is a clear

indication of drag rise for the wing-winglet configuration at about M = 0.9. However, it is expected that actual drag increments above M = 0.9 are underpredicted, since the wing boundary layer calculation predicts that separation will occur just aft of the shocks for this geometry.

DISCUSSION

All of the present PPW nonlinear performance predictions support the much simpler trends discussed under Design Philosophy above, using a far field drag model. The predicted percentage drag coefficient reductions of the wing-winglet designs at the design point are largely independent of wing planform (aspect ratio and leading edge sweep), and tend to scale directly proportional to the ratio of winglet length divided by wing semispan. Both of these trends are predicted by the simple far field theory. Of course, these conclusions will remain valid only so long as smooth, attached flow can be maintained on both the wing and winglet. Some limited efforts to obtain PPW solutions at higher lift coefficient for the configurations discussed in the present study have usually led to diverging, unstable solutions. This indicates in some general sense that the actual flow field would be too highly loaded on the winglet inboard surface or near the wing tip, so that shock-induced flow separation would be expected in these regions at higher lift coefficients. This could negate any drag reductions due to the winglet at high lift. However, it does appear possible to increase winglet toe out and unload the wing tip by reducing tip incidence, as has been done for wing-winglet A (Fig. 17) above $\alpha = 1.5°$, as C_L is increased, thereby maintaining attached flow over a wider range of lift coefficients. Thus it may be necessary to utilize

variable wing tip and/or winglet geometry to maintain attached flow conditions over a range of lift coefficients.

Analysis of the predicted performance versus angle of attack presented in Figs. 17-21, 24 and 25 yields the predicted percentage increases in L/D shown in Table 5. Predicted percentage increases in L/D due to a winglet generally increase somewhat as C_L is decreased. The longer winglet again is seen to yield a larger increase in L/D. Finally, even with the reduced loading at the wing tip and winglet root for configuration A at higher lift coefficient values of 0.35 and 0.4, there is still a significant increase (8-10%) in L/D due to a winglet. These results show there appears to be significant drag reduction potential for winglets installed on low aspect ratio wings even up to $C_L \cong .42$ at $M = .8$.

While the present results are very encouraging there is some concern over the level of accuracy of the drag levels computed by integration of the pressure distributions in the PPW code (ref. 11, p. 139) or that this accuracy might be significantly reduced at low aspect ratio, or for nonplanar configurations. For example, there is no complete treatment of the three dimensional boundary layers which form in the wing-winglet and wing-body junctures. Also, the flow fields on the body and on the winglets are not interacted with any viscous boundary layer calculation. To date no complete assessment of these concerns has been made. However, it is noted that the predicted pressure drag reductions at the design point (Table 4) are in all instances somewhat less than the maximum achievable reduction in induced drag as predicted by the far field drag model.

Table 5. PPW Predicted Percentage Lift-to-Total Drag Increases Due to Winglets at Various Lift Levels

Config.	$\ell/(b/2)$	M	$C_L = .2$	$C_L = .25$	$C_L = .3$	$C_L = .35$*	$C_L = .4$*
A	0.15	0.8	15.7%	14.7%	11.5%	9.8%	8.2%
B	0.15	0.8	16.7%	14.2%	11.8%	--	--
F	0.15	0.8	19.1%	16.3%	13.3%	--	--
G	0.15	0.8	--	15.9%	12.1%	--	--
L45	0.25	0.8	--	19.2%	19.4%	--	--
A	0.15	0.75	16.8%	13.8%	11.2%	--	--
A	0.15	0.70	14.7%	13.5%	11.3%	--	--

* Wing tip incidence reduced and winglet root toe out increased; see Appendix.

Some insight into accuracy of the PPW code calculated drag has been obtained by plotting the calculated PPW pressure drag coefficient in drag counts versus Mach number for an uncambered, untwisted wing as shown in Fig. 29. For these results, the wing has a taper ratio of 0.2, an aspect ratio of 2.5, a wing leading edge sweep of 44°, and an NACA 64A006 thickness distribution. Calculated pressure drag is essentially zero (less than one count) for the wing-alone for $0.1 \leq M \leq 0.9$. Above $M = 0.9$ there is a very steep increase in C_{Dp}, indicating the onset of drag rise. Also shown in Fig. 29 are similar pressure drag results for the same wing with a short winglet ($\ell = 0.15(b/2)$, $\Lambda = 45°$). Here, due to interference effects, the wing tip and winglet root incidences had to be reduced by trial-and-error until a wing-plus-winglet lift coefficient of zero was obtained. For these slightly twisted, uncambered wing-winglet geometries (wing tip and winglet root incidence varied slightly with Mach number), the calculated pressure drag is essentially identical to that of the wing-alone

at $C_L = 0$. Thus, there is no evidence of any difference in the accuracy of the PPW drag coefficient calculation by pressure integration for the wing-winglet or wing-alone configurations, at least for these thickness dominated flows. The small C_{Dp} values shown in Fig. 29 at M = 0.8 are less than 1% of the calculated drag coefficient levels for configurations A, B, F, and G at the selected design point of M = 0.8, $C_L \cong 0.3$. Hence, these errors are not believed to significantly affect the basic conclusions of the present study.

CONCLUSIONS

A preliminary numerical design study has been performed to assess the potential for drag reduction at a transonic cruise design point for winglets installed on low aspect ratio wings. All initial design geometries have been generated using linearized potential flow theory. These initial geometries have been modified as required to overcome linear flow limitations, and then performance has been analyzed using the PPW numerical nonlinear potential flow model. For wings of aspect ratios ranging from 2.67 to 1.75 and leading edge sweep angles from 45 to 60°, realistic converged flow predictions have been obtained using the nonlinear analysis code at M = 0.8, $C_L \cong 0.3$ without modification to the linear-theory designs. Realistic converged flow solutions were also obtained from the nonlinear analysis code for wing-winglet designs generated for a 50° leading edge sweep winglet of length equal to 15% of the wing semispan, installed on the higher aspect ratio wing planforms. Here converged transonic flow solutions were only obtained when winglet root toe out and wing tip incidence were systematically altered to reduce the winglet and wing tip loading levels relative to those required by the linear theory design

methods. Converged solutions were not obtained for the $A = 1.75$ wing-winglet configurations, and difficulty was often experienced in obtaining convergence at lift levels above $C_L \cong 0.3$.

For the 0.15(b/2), 50° leading edge sweep winglets, the predicted pressure drag coefficient reductions at the design point were about 15% while total drag coefficient reductions were about 12%, relative to the wing-alone design at the same lift. These predicted percentage reductions were largely independent of the basic wing aspect ratio and wing leading edge sweep. For the 0.25(b/2), 45° leading edge sweep winglet a pressure drag coefficient reduction of 19% and a total drag coefficient reduction of 15% were predicted. Thus, it has been concluded that, at least for winglet lengths below 25% of the wing semispan, the fractional pressure drag reduction due to a winglet approaches the induced drag reduction predicted by a simple far field induced drag model. This drag model predicts the fractional induced drag coefficient reduction, $1-1/k$, is simply related to the ratio of winglet length to wing semispan, in that $k \cong 1 + \ell/(b/2)$.

These percent reductions in drag coefficient due to a winglet were found to be maintained as Mach number was varied from 0.7 to 0.9 for one of the wing geometries studied, for a wing of $A = 2.63$, $\Lambda = 50°$. However, as Mach number is increased above about 0.9 the onset of drag rise is predicted for this wing-winglet configuration at $0.2 \leq C_L \leq 0.25$.

For this same wing-winglet configuration it was also possible to obtain total drag coefficient reductions of 8-10% at $M = 0.8$ at higher lift coefficients (up to $C_L = 0.42$). This was achieved by further unloading of the wing-winglet juncture region by simply reducing the wing tip incidence

and increasing winglet root toe out as required.

Thus, the simple basic premise which motivated the present study appears to be valid. Winglets appear to have the potential to achieve significantly larger drag force reductions when applied to low aspect ratio wings rather than at higher aspect ratio. This is because the percentage drag coefficient reduction at equal lift is relatively independent of wing aspect ratio, while the lift-to-drag ratio increases with aspect ratio. Thus, the lower aspect ratio configuration develops a much larger drag force at equal lift and wing loading.

ACKNOWLEDGMENTS

The present study has been conducted using the NASA Langley Research Center computer facilities. NASA has provided access to the Langley computer facility via TELENET, as well as the required computer run time. Several discussions with Charlie Boppe at Grumman, and Ed Waggoner and Pam Phillips at NASA Langley were extremely helpful in learning to utilize the PPW code. Early discussions with Leroy Spearman at NASA Langley helped to clarify the basic concept. Finally, thanks are also due to Dr. Richard W. Barnwell at Langley for initially suggesting this problem to the first author.

REFERENCES

1. Whitcomb, R. T., "A Design Approach and Selected Wind-Tunnel Results at High Subsonic Speeds for Wing-Tip Mounted Winglets," NASA TN D-8260, July 1976.

2. Flechner, S. G., Jacobs, P. F., and Whitcomb, R. T., "A High Subsonic Speed Wind-Tunnel Investigation of Winglets on a Representative Second-Generation Jet Transport Wing," NASA TN D-8264, July 1976.

3. Asai, K., "Theoretical Considerations in the Aerodynamic Effectiveness of Winglets," J. of Aircraft, Vol. 22, No. 7, July 1985, pp. 635-637.

4. Reynolds, P. T., Gertsen, W. M., and Voorhees, C. G., "Gates Learjet Model 28/29, the First 'Longhorn' Learjet," Paper AIAA-78-1445, Presented at AIAA Aircraft Systems and Technology Conference, Los Angeles, CA, August 21-23, 1978.

5. Cary, M. D., "A Parametric Analysis of Winglet Effects," M.S. Thesis, Air Force Inst. Tech., Wright-Patterson AFB, OH, December 1976.

6. Heyson, H. H., Riebe, G. D., and Fulton, C. L., "Theoretical Parametric Study of the Relative Advantages of Winglets and Wing-Tip Extensions," NASA TP-1020, 1977.

7. Gingrich, P. B., Child, R. D., and Panageas, G. N., "Aerodynamic Configuration Development of the Highly Maneuverable Aircraft Technology Remotely Piloted Research Vehicle," NASA CR-143841, June 1977.

8. Laiosa, J., "Prediction of HiMAT RPRV Component Interference Effects at Transonic Speeds," Paper AIAA-85-0213, Presented at AIAA 23rd Aerospace Sciences Meeting, Reno, NV, January 14-17, 1985.

9. Boppe, C. W. and Stern, M. A., "Simulated Transonic Flows for Aircraft with Nacelles, Pylons, and Winglets," Paper AIAA-80-0130, Presented at AIAA 18th Aerospace Sciences Meeting, Pasadena, CA, January 14-16, 1980.

10. Boppe, C. W., "Transonic Flow Field Analysis for Wing-Fuselage Configurations," NASA CR-3243, May 1980.

11. Boppe, C. W., "Aerodynamic Analysis for Aircraft With Nacelles, Pylons, and Winglets at Transonic Speeds," NASA CR-4066, April 1987.

12. Hackett, J. E., "Vortex Drag and Its Reduction," Paper Number 8, AGARD-R-723, Presented at Aircraft Drag Prediction and Reduction Short Course, Von Karman Institute, Belgium, May 20-23, 1985.

13. Kuhlman, J. M., "Higher Order Farfield Drag Minimization for a Subcritical Wing Design Code," J. of Aircraft, Vol. 17, No. 9, September 1980, pp. 648-655.

14. Kuhlman, J. M. and Shu, J.-Y., "Computer Program Documentation for a Subcritical Wing Design Code Using Higher Order Far-Field Drag Minimization," NASA CR-3457, September 1981.

15. Kuhlman, J. M., "Iterative Optimal Subcritical Aerodynamic Design Code Including Profile Drag," Paper AIAA-83-0012, Presented at AIAA 21st Aerospace Sciences Meeting, Reno, NV, January 10-13, 1983.

16. Kuhlman, J. M., "Numerical Optimization Techniques for Bound Circulation Distribution for Minimum Induced Drag of Nonplanar Wings: Basic Formulations," NASA CR-3154, June 1979.

17. Lundry, J. L. and Lissaman, P.B.S., "A Numerical Solution for the Minimum Induced Drag of Nonplanar Wings," J. of Aircraft, Vol. 5, No. 1, January-February 1968, pp. 17-21.

18. Spearman, M. L. and Monta, W. J., "Effects of External Stores on the Aerodynamic Characteristics of a 60° Delta-Wing Fighter Model at Mach 1.60 to 2.87," NASA TM- 74090, December 1977.

19. Kuhlman, J. M., "Optimized Aerodynamic Design Process for Subsonic Transport Wing Fitted with Winglets," NASA CR-159180, December 1979.

20. Kuhlman, J. M., "Longitudinal Aerodynamic Characteristics of a Wing-Winglet Model Designed at M = 0.8, C_L = 0.4 Using Linear Aerodynamic Theory," NASA CR-172186, July 1983.

21. "Janes' All the Worlds Aircraft, 1984-85 75th Anniversary Issue," Janes' Publishing Co., London, England, 1985.

22. Mann, M. J., Campbell, R. L., and Ferris, J. C., "Aerodynamic Design for Improved Maneuverability by Use of Three-Dimensional Transonic Theory," NASA TP-2282, February 1984.

23. Bhateley, I. C., Mann, M. J., and Ballhaus, W. F., "Evaluation of Three-Dimensional Transonic Methods for the Analysis of Fighter Configurations," Paper AIAA-79-1528, Presented at AIAA 12th Fluid and Plasma Dynamics Conference, Williamsburg, VA, July 23-25, 1979.

24. "Special Report: Advanced Fighter Technology," Aviation Week and Space Technology, June 23, 1986, pp. 48-176.

25. Vincent, J., "New Technologies for a European Fighter," Aerospace America, Vol. 24, No. 6, June 1986, pp. 34-36.

26. Langereux, P., "Rafale Will Keep Tricolor Flying," Aerospace America, Vol. 24, No. 6, June 1986, pp. 26-30.

27. Erickson, G. E. and Rogers, L. W., "Experimental Investigation at Low- and High-Subsonic Speeds of a Moderately Swept Fighter Wing with Deflected Leading-Edge Flaps," Presented at Vortex Flow Aerodynamics Conference, NASA Langley Research Center, Hampton, VA, October 8-10, 1985, NASA CP-2417, pp. 141-168.

28. Waggoner, E. G., "Computational Transonic Analysis for a Supercritical Transport Wing-Body Configuration," Paper AIAA-80-0129, Presented at AIAA 18th Aerospace Sciences Meeting, Pasadena, CA, January 14-16, 1980.

29. Bradley, R. G. and Bhateley, I. C., "Computational Aerodynamic Design of Fighter Aircraft-Progress and Pitfalls," Paper AIAA-83-2063, Presented at AIAA Atmospheric Flight Mechanics Conference, Gatlinburg, TN, August 15-17, 1983.

30. Liaw, P., "The Use of Winglets on Low Aspect Ratio Wings for Drag Reduction at Transonic Speeds," M.S. Thesis, Mechanical and Aerospace Engineering Department, West Virginia University, Morgantown, WV, June 1987.

31. Luckring, J. M., "Some Recent Applications of the Suction Analogy to Asymmetric Flow Situations," Proceedings of Vortex-Lattice Utilization Workshop, NASA Langley Research Center, Hampton, VA, May 17-18, 1976, NASA SP-405, pp. 219-236.

32. Hall, J. F., Neuhart, D. H., and Walkley, K. B., "An Interactive Graphics Program for Manipulation and Display of Panel Method Geometry," NASA CR-166098, March 1983.

Wing Fitted with 0.15(b/2), λ = 0.5, Λ = 50° Winglet
Without Winglet Twist Alteration

Configuration A
M = 0.8

	(Wing)					(Winglet)					
α	C_L	C_{Dp}	C_{Df}	C_M	C_{RBM}	C_L	C_{Dp}	C_{Df}	C_M	C_{RBM}	DELTA PHI MAX
1.0°	.30272	.01624	.00241	-.33660	.16172	.00403	-.00221	.00014	-.00582	.00503	9.71×10^{-6}(crude)
0.5°	.27934	.01337	.00242	-.31443	.15089	.00388	-.00200	.00014	-.00561	.00499	1.04×10^{-5}(crude)
0°	.25573	.01079	.00244	-.29195	.13695	.00373	-.00181	.00014	-.00540	.00463	1.35×10^{-5}(crude)
-1.0°	.20604	.00628	.00248	-.24400	.11115	.00338	-.00141	.00014	-.00492	.00418	1.43×10^{-5}(crude)
-1.5°	.18239	.00474	.00250	-.22203	.09850	.00313	-.00118	.00014	-.00459	.00386	7.29×10^{-6}(crude)

Wing Fitted with 0.15(b/2), λ = 0.5, Λ = 50° Winglet
With Wing And Winglet Twist Alteration

Configuration A
M = 0.8

	(Wing)					(Winglet)					
α	C_L	C_{Dp}	C_{Df}	C_M	C_{RBM}	C_L	C_{Dp}	C_{Df}	C_M	C_{RBM}	DELTA PHI MAX
3.5°	.41350	.03364	.00241	-.44215	.21757	.00430	-.00301	.00014	-.00619	.00542	1.95×10^{-5}(crude)
(ε_{wing}=-.7°, -.7°, -2.5; ε_{wlet}= -2°, -1.1°, 0°, 0°)											
3°	.38784	.02903	.00240	-.41640	.20432	.00416	-.00273	.00014	-.00600	.00524	6.46×10^{-5}(tag)
(ε_{wing}=-.7°, -.7°, -2.4°; ε_{wlet}=-1.9°, -1°, 0°, 0°)											
2.5°	.36552	.02527	.00240	-.39515	.19263	.00411	-.00255	.00014	-.00592	.00515	1.51×10^{-5}(crude)
(ε_{wing}= -.6°, -.6°, -2.3°; ε_{wlet}= -1.6°, -.8°, 0°, 0°)											
2°	.34813	.02268	.00240	-.37989	.18472	.00412	-.00248	.00014	-.00594	.00516	1.25×10^{-5}(crude)
($\varepsilon_{w\text{-}tip}$= -1.6°; ε_{wlet}= -1°, -.5°, 0°, 0°)											
1.5°	.32627	.01953	.00240	-.35945	.17367	.00405	-.00235	.00014	-.00584	.00507	1.31×10^{-4}(tag)
($\varepsilon_{w\text{-}tip}$= -.5°; ε_{wlet}= -1°, -.5°, 0°, 0°)											

Wing-Alone A: $\lambda = 0.2$, $\Lambda = 50°$, AR = 2.63
M = 0.8

α	C_L	C_{Dp}	C_{Df}	C_M	C_{RBM}	DELTA PHI MAX	e
3.5°	.42688	.03556	.00241	-.45020	.21861	2.12×10^{-4}(fine)	.978
3°	.40517	.03150	.00239	-.43036	.20763	1.15×10^{-4}(fine)	.977
2.5°	.38164	.02739	.00239	-.40806	.19568	2.01×10^{-5}(crude)	.976
2°	.35812	.02351	.00239	-.38568	.18393	2.36×10^{-5}(crude)	.974
1.5°	.33432	.01992	.00239	-.36302	.17195	2.04×10^{-5}(crude)	.972
1°	.30944	.01646	.00239	-.33885	.15948	9.00×10^{-6}(crude)	.970
0.47°	.28548	.01346	.00241	-.31650	.14712	1.07×10^{-5}(crude)	.969
-.5°	.23973	.00878	.00244	-.27368	.12377	1.40×10^{-5}(crude)	.965
-1.5°	.19131	.00495	.00248	-.22800	.09903	1.07×10^{-5}(crude)	.960

Wing Fitted with 0.15(b/2), $\lambda = 0.5$, $\Lambda = 50°$ Winglet
Without Winglet Twist Alteration

Configuration A

M = 0.75

	(Wing)					(Winglet)					
α	C_L	C_{Dp}	C_{Df}	C_M	C_{RBM}	C_L	C_{Dp}	C_{Df}	C_M	C_{RBM}	DELTA PHI MAX
1.5°	.31452	.01880	.00237	-.34565	.16719	.00402	-.00218	.00014	-.00582	.00502	1.80×10^{-5}(crude)
1°	.29025	.01542	.00238	-.32146	.15439	.00384	-.00199	.00014	-.00556	.00479	1.58×10^{-5}(crude)
0.5°	.26836	.01275	.00240	-.30111	.14315	.00375	-.00182	.00014	-.00544	.00466	1.78×10^{-5}(crude)
0°	.24522	.01016	.00241	-.27887	.13114	.00360	-.00164	.00014	-.00524	.00446	9.92×10^{-6}(crude)
-.5°	.22076	.00777	.00243	-.25485	.11822	.00337	-.00144	.00014	-.00492	.00418	1.28×10^{-5}(crude)
-1°	.19704	.00581	.00245	-.23216	.10585	.00320	-.00127	.00014	-.00468	.00395	1.28×10^{-5}(crude)
-1.5°	.17310	.00414	.00248	-.20929	.09320	.00297	-.00106	.00014	-.00436	.00366	1.56×10^{-5}(crude)

Wing-Alone A: $\lambda = 0.2$, $\Lambda = 50°$, AR = 2.63

M = 0.75

α	C_L	C_{Dp}	C_{Df}	C_M	C_{RBM}	DELTA PHI MAX	e
1.5°	.31904	.01894	.00236	-.34508	.16381	3.66×10^{-5}(crude)	.973
1°	.29767	.01590	.00236	-.32522	.15291	1.71×10^{-5}(crude)	.972
0.5°	.27455	.01294	.00238	-.30304	.14134	1.15×10^{-5}(crude)	.970
0°	.25240	.01054	.00239	-.28247	.12988	1.35×10^{-5}(crude)	.969
-1°	.20754	.00646	.00243	-.24079	.10691	8.80×10^{-6}(crude)	.965
-1.5°	.18276	.00457	.00245	-.21672	.09416	1.70×10^{-5}(crude)	.965
-2°	.15997	.00331	.00248	-.19578	.08226	1.49×10^{-5}(crude)	.964

Wing Fitted with 0.15(b/2), λ = 0.5, Λ = 50° Winglet
Without Winglet Twist Alteration

Configuration A

M = 0.7

	(Wing)					(Winglet)					
α	C_L	C_{Dp}	C_{Df}	C_M	C_{RBM}	C_L	C_{Dp}	C_{Df}	C_M	C_{RBM}	DELTA PHI MAX
2.5°	.34521	.02464	.00234	-.37172	.18255	.00408	-.00231	.00014	-.00590	.00511	2.24×10^{-5}(crude)
2°	.32411	.02115	.00234	-.35168	.17161	.00398	-.00216	.00014	-.00576	.00498	3.43×10^{-5}(crude)
1.5°	.30218	.01775	.00235	-.33042	.16031	.00388	-.00201	.00014	-.00562	.00484	1.56×10^{-5}(crude)
1°	.28195	.01504	.00236	-.31201	.14988	.00375	-.00186	.00014	-.00545	.00467	1.80×10^{-5}(crude)
.85°	.27424	.01400	.00236	-.30399	.14575	.00372	-.00182	.00014	-.00539	.00462	1.83×10^{-5}(crude)
0°	.23666	.00968	.00239	-.26821	.12626	.00345	-.00153	.00014	-.00502	.00427	1.13×10^{-5}(crude)
-.5°	.21397	.00748	.00241	-.24647	.11443	.00327	-.00136	.00014	-.00479	.00405	1.31×10^{-5}(crude)
-1°	.19118	.00560	.00243	-.22475	.10235	.00308	-.00117	.00014	-.00451	.00379	8.10×10^{-6}(crude)
-1.5°	.16807	.00401	.00245	-.20276	.09021	.00286	-.00097	.00014	-.00421	.00352	7.53×10^{-6}(crude)

Wing-Alone A: λ = 0.2, Λ = 50° , AR = 2.63

M = 0.7

α	C_L	C_{Dp}	C_{Df}	C_M	C_{RBM}	DELTA PHI MAX	e
2.5°	.34865	.02478	.00232	-.36986	.17847	2.19×10^{-5}(crude)	.978
2°	.32714	.02113	.00232	-.34925	.16761	1.55×10^{-5}(crude)	.976
1.5°	.30728	.01816	.00233	-.33125	.15740	2.56×10^{-5}(crude)	.975
1°	.28652	.01524	.00234	-.31200	.14695	2.15×10^{-5}(crude)	.974
.5°	.26509	.01254	.00235	-.29190	.13605	1.93×10^{-5}(crude)	.972
0°	.24423	.01023	.00237	-.27281	.12546	1.61×10^{-5}(crude)	.970
-1°	.19951	.00604	.00240	-.23048	.10251	1.42×10^{-5}(crude)	.968
-1.5°	.17733	.00448	.00243	-.20987	.09103	9.96×10^{-6}(crude)	.967
-2°	.15414	.00308	.00245	-.18792	.07898	9.82×10^{-6}(crude)	.966

Wing Fitted with 0.15(b/2), $\lambda = 0.5$, $\Lambda = 50°$ Winglet
Without Winglet Twist Alteration

Configuration B

M = 0.8

	(Wing)					(Winglet)					
α	C_L	C_{Dp}	C_{Df}	C_M	C_{RBM}	C_L	C_{Dp}	C_{Df}	C_M	C_{RBM}	DELTA PHI MAX
.75°	.29486	.01548	.00220	-.29749	.15744	.00425	-.00230	.00013	-.00527	.00528	1.91×10^{-5}(crude)
0.5°	.28272	.01400	.00221	-.28726	.15093	.00416	-.00218	.00013	-.00517	.00517	2.17×10^{-5}(tag)
.25°	.27114	.01266	.00221	-.27785	.14497	.00408	-.00207	.00013	-.00508	.00506	1.36×10^{-5}(crude)
.0°	.25894	.01132	.00222	-.26765	.13858	.00399	-.00197	.00013	-.00498	.00495	9.96×10^{-6}(crude)
-.5°	.23433	.00887	.00223	-.24698	.12572	.00381	-.00176	.00013	-.00476	.00471	1.38×10^{-5}(tag)
-1°	.20915	.00669	.00225	-.22567	.11245	.00360	-.00154	.00013	-.00451	.00444	8.55×10^{-6}(crude)
-1.5°	.18511	.00499	.00226	-.20609	.10007	.00338	-.00133	.00013	-.00426	.00417	7.89×10^{-6}(crude)
-1.75°	.17248	.00421	.00227	-.19554	.09338	.00326	-.00121	.00013	-.00411	.00401	7.93×10^{-6}(crude)
-2.0°	.15987	.00347	.00228	-.18500	.08679	.00314	-.00110	.00013	-.00397	.00386	8.99×10^{-6}(crude)

Wing-Alone B: $\lambda = 0.2$, $\Lambda = 45°$, AR = 2.67

M = 0.8

α	C_L	C_{Dp}	C_{Df}	C_M	C_{RBM}	DELTA PHI MAX	e
.75°	.30218	.01548	.00217	-.29977	.15441	1.18×10^{-5}(crude)	.979
.5°	.29024	.01407	.00218	-.29004	.14840	1.32×10^{-5}(crude)	.978
0°	.26566	.01127	.00219	-.26943	.13577	1.70×10^{-5}(crude)	.977
-.5°	.24144	.00893	.00220	-.24952	.12325	1.45×10^{-5}(crude)	.976
-1°	.21732	.00688	.00221	-.22988	.11096	1.06×10^{-5}(crude)	.975
-1.5°	.19278	.00511	.00223	-.20975	.09826	9.47×10^{-6}(crude)	.973
-2°	.16806	.00369	.00225	-.18958	.08546	6.72×10^{-6}(crude)	.970

Wing Fitted with 0.15(b/2), λ = 0.5, Λ = 50° Winglet
Without Winglet Twist Alteration

Configuration F

M = 0.8

	(Wing)					(Winglet)					
α	C_L	C_{Dp}	C_{Df}	C_M	C_{RBM}	C_L	C_{Dp}	C_{Df}	C_M	C_{RBM}	DELTA PHI MAX
.65°	.29104	.01814	.00205	-.26348	.15481	.00447	-.00262	.00013	-.00464	.00557	1.82×10^{-5}(fine)
.5°	.28474	.01725	.00205	-.25900	.15153	.00442	-.00255	.00013	-.00459	.00551	1.57×10^{-5}(fine)
0°	.26315	.01436	.00206	-.24335	.14031	.00426	-.00232	.00013	-.00444	.00530	1.35×10^{-5}(crude)
-.5°	.24126	.01175	.00207	-.22745	.12881	.00407	-.00208	.00013	-.00426	.00505	1.38×10^{-5}(crude)
-1°	.21938	.00943	.00208	-.21163	.11738	.00388	-.00185	.00013	-.00407	.00480	1.17×10^{-5}(crude)
-1.5°	.19753	.00740	.00210	-.19592	.10597	.00367	-.00162	.00013	-.00387	.00454	2.45×10^{-5}(tag)
-2°	.17558	.00569	.00211	-.18029	.09453	.00344	-.00137	.00013	-.00364	.00424	8.91×10^{-6}(crude)
-2.5°	.15291	.00423	.00213	-.16390	.08258	.00318	-.00111	.00013	-.00339	.00391	8.23×10^{-6}(crude)
-2.75°	.14141	.00363	.00214	-.15560	.07652	.00305	-.00098	.00013	-.00326	.00374	8.05×10^{-6}(crude)

Wing-Alone F: λ = 0.2, Λ =45° , AR = 2.20

M = 0.8

α	C_L	C_{Dp}	C_{Df}	C_M	C_{RBM}	DELTA PHI MAX	e
1°	.31218	.02063	.00202	-.27576	.15925	1.49×10^{-5}(crude)	.982
0.5°	.29181	.01761	.00203	-.26151	.14888	1.46×10^{-5}(crude)	.981
0°	.27130	.01485	.00203	-.24713	.13843	1.32×10^{-5}(crude)	.980
-.5°	.25058	.01233	.00204	-.23257	.12785	1.16×10^{-5}(crude)	.980
-1°	.22975	.01008	.00205	-.21797	.11721	1.04×10^{-5}(crude)	.979
-1.5°	.20880	.00808	.00206	-.20330	.10646	9.23×10^{-6}(crude)	.978
-2°	.18761	.00635	.00208	-.18847	.09555	8.87×10^{-6}(crude)	.977
-2.25°	.17685	.00560	.00209	-.18093	.08999	8.71×10^{-6}(crude)	.976

Wing Fitted with 0.15(b/2), λ = 0.5, Λ = 50° Winglet
Without Winglet Twist Alteration

Configuration G

M = 0.8

	(Wing)					(Winglet)					
α	C_L	C_{Dp}	C_{Df}	C_M	C_{RBM}	C_L	C_{Dp}	C_{Df}	C_M	C_{RBM}	DELTA PHI MAX
1°	.30693	.01991	.00230	-.30581	.16415	.00415	-.00275	.00013	-.00506	.00518	1.26×10^{-5}(crude)
.5°	.28677	.01700	.00231	-.28958	.15262	.00404	-.00251	.00013	-.00493	.00490	1.39×10^{-5}(crude)
0°	.26355	.01388	.00232	-.26921	.14144	.00388	-.00229	.00013	-.00475	.00482	1.31×10^{-5}(crude)
-.5°	.24255	.01145	.00233	-.25202	.13043	.00372	-.00206	.00013	-.00457	.00461	1.62×10^{-5}(crude)
-1°	.21853	.00888	.00235	-.23084	.11765	.00355	-.00186	.00013	-.00437	.00439	9.87×10^{-6}(crude)
-1.25°	.20859	.00795	.00236	-.22301	.11253	.00346	-.00176	.00013	-.00427	.00428	2.77×10^{-5}(crude)

Wing-Alone G: λ = 0.2, Λ = 50°, AR = 2.2

M = 0.8

α	C_L	C_{Dp}	C_{Df}	C_M	C_{RBM}	DELTA PHI MAX	e
1°	.30782	.01951	.00227	-.30140	.15736	1.32×10^{-5}(crude)	.980
.5°	.28877	.01684	.00228	-.28665	.14757	1.93×10^{-5}(crude)	.979
0°	.26707	.01397	.00229	-.26837	.13665	9.67×10^{-6}(crude)	.978
-.5°	.24576	.01140	.00230	-.25065	.12577	1.30×10^{-5}(crude)	.977
-1°	.22442	.00921	.00232	-.23312	.11473	1.29×10^{-5}(crude)	.977

Wing Fitted with 0.15(b/2), $\lambda = 0.5$, $\Lambda = 50°$ Winglet
With Winglet Twist Alteration

Configuration G , $\varepsilon_{winglet} = -3°, -.5°, 0°, 0°$

M = 0.8

	(Wing)					(Winglet)					
α	C_L	C_{Dp}	C_{Df}	C_M	C_{RBM}	C_L	C_{Dp}	C_{Df}	C_M	C_{RBM}	DELTA PHIMAX
1°	.30681	.01993	.00230	-.30575	.16401	.00404	-.00280	.00013	-.00494	.00505	1.28×10^{-5} (crude)
.5°	.28614	.01693	.00231	-.28882	.15234	.00392	-.00259	.00013	-.00480	.00488	1.36×10^{-5} (crude)
-.5°	.24078	.01119	.00233	-.24969	.12933	.00360	-.00213	.00013	-.00443	.00446	2.44×10^{-5} (crude)
-1°	.21793	.00883	.00235	-.23014	.11725	.00342	-.00192	.00013	-.00422	.00423	1.05×10^{-5} (crude)
-1.5°	.19517	.00675	.00237	-.21078	.10521	.00321	-.00168	.00013	-.00397	.00396	1.88×10^{-5} (crude)

Wing H Fitted with 0.25(b/2), λ = 0.5, Λ = 50° Winglet
With Wing And Winglet Twist Alteration

Configuration L45 ε_{wing} = .5°, 0°, ---, 0°, -.5°
ε_{wlet} = -1.6°, -.4°, 2.8°, 4.6°

M = 0.8

	(Wing)					(Winglet)					
α	C_L	C_{Dp}	C_{Df}	C_M	C_{RBM}	C_L	C_{Dp}	C_{Df}	C_M	C_{RBM}	DELTA PHI MAX
0.5°	.27631	.01624	.00256	-.31360	.14902	.00730	-.00325	.00022	-.01062	.01037	1.91×10^{-5}(fine)
0°	.25356	.01323	.00258	-.29046	.13703	.00692	-.00287	.00022	-.01009	.00983	2.57×10^{-5}(fine)
-.5°	.23406	.01106	.00260	-.27226	.12661	.00658	-.00254	.00022	-.00962	.00932	3.60×10^{-5}(tag)
-1°	.21132	.00868	.00262	-.24959	.11465	.00614	-.00210	.00022	-.00901	.00867	1.66×10^{-5}(crude)

Wing-Alone H: λ = 0.2, Λ = 55° AR = 2.2

M = 0.8

α	C_L	C_{Dp}	C_{Df}	C_M	C_{RBM}	DELTA PHI MAX	e
1°	.30335	.01887	.00253	-.33396	.15471	7.13×10^{-6}(crude)	.979
.5°	.28300	.01598	.00254	-.31442	.14423	6.98×10^{-6}(crude)	.978
0°	.26256	.01340	.00255	-.29489	.13377	7.47×10^{-6}(crude)	.978
-.5°	.24305	.01123	.00257	-.27680	.12372	6.75×10^{-6}(crude)	.977
-1°	.22005	.00887	.00260	-.25393	.11193	1.29×10^{-5}(crude)	.976

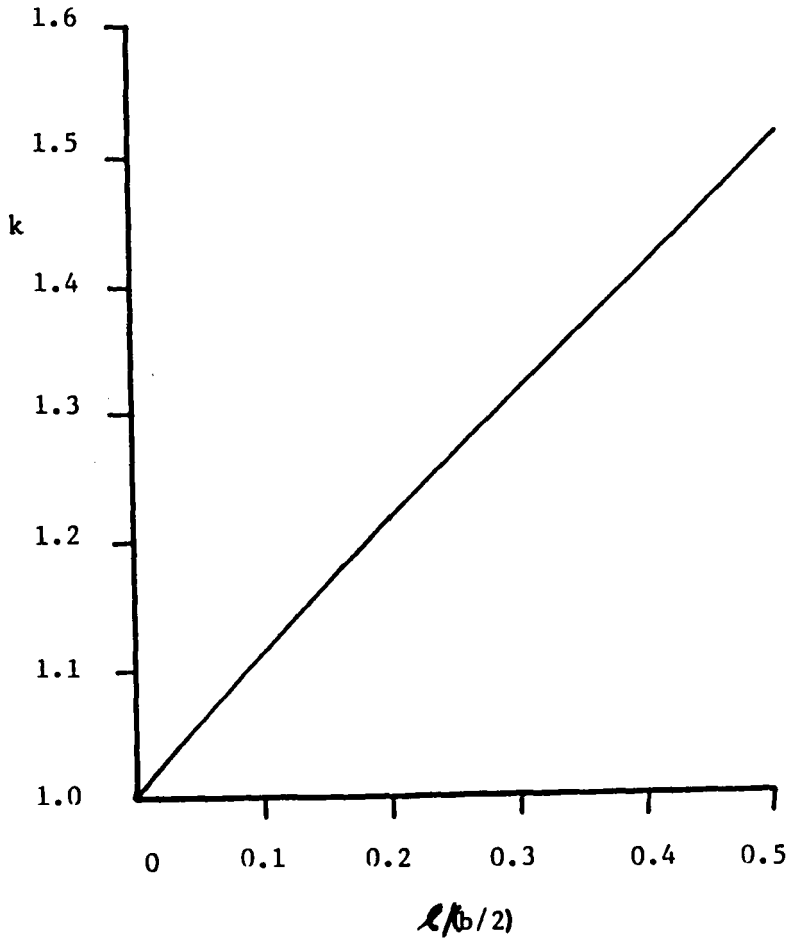

Fig. 1a. Predicted performance benefits of winglets based on far field theory[13,16]: induced drag efficiency, k, versus endplate or winglet length, ℓ.

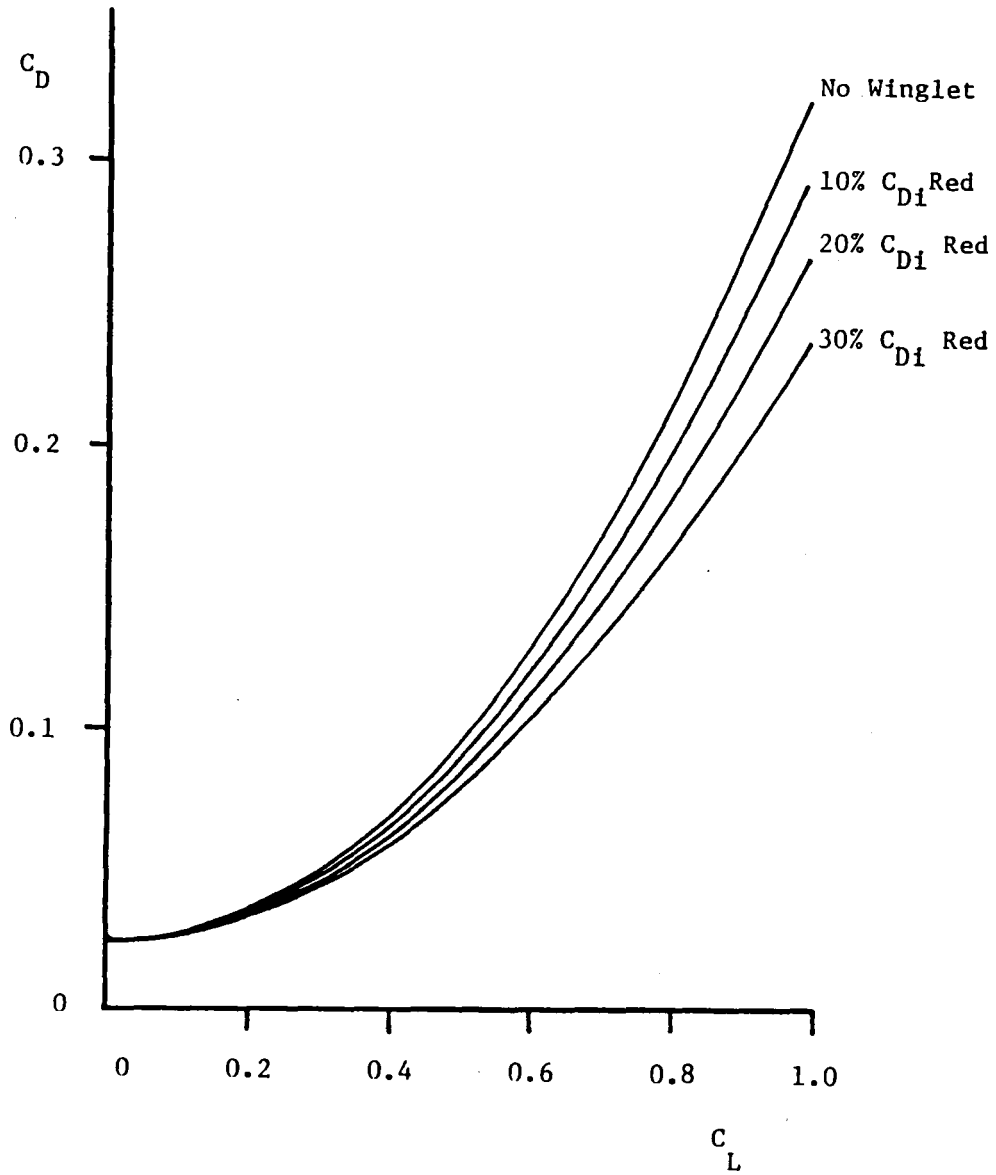

Fig. 1b. Predicted performance benefits of winglets based on far field theory[13,16]: maximum effect of winglets on drag of A = 2.2 fighter model at M = 1.6[18].

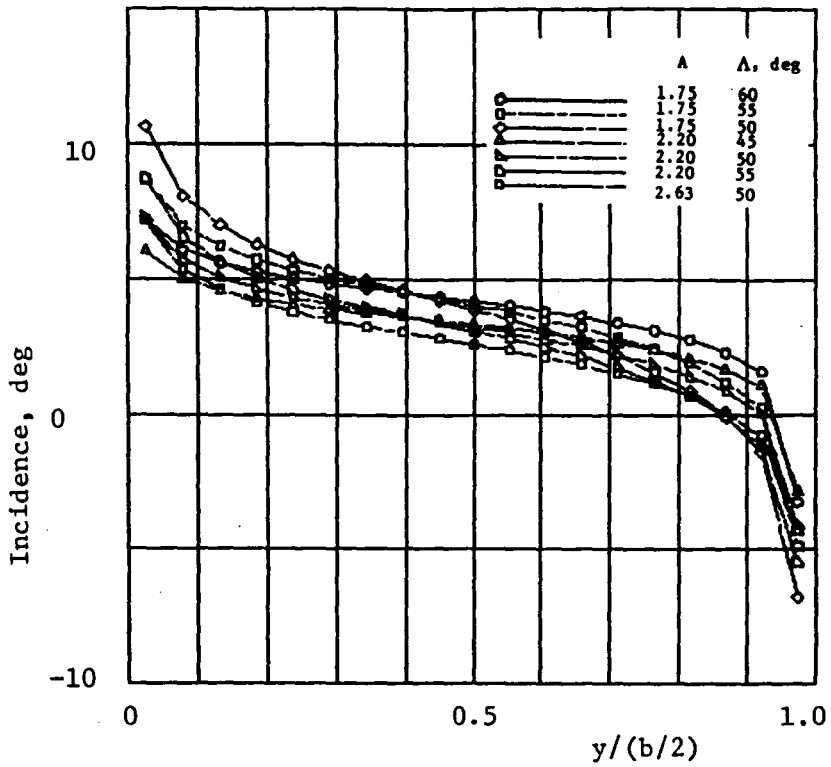

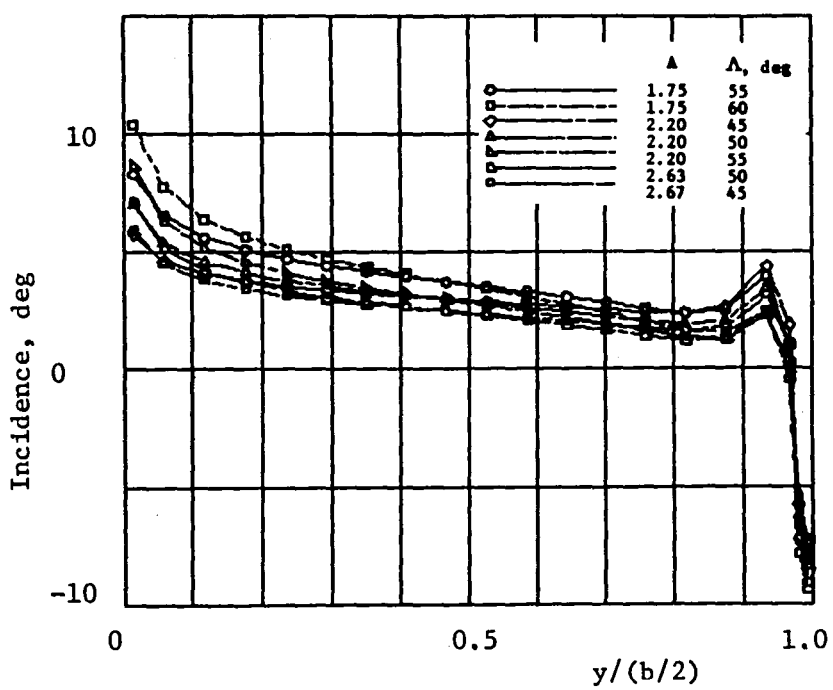

Fig. 2. Incidence distributions for linear theory minimum induced drag designs at M = 0.8, $C_L \cong 0.3$ for configurations of Table 1:
a) Wing-alone
b) Wing-winglet

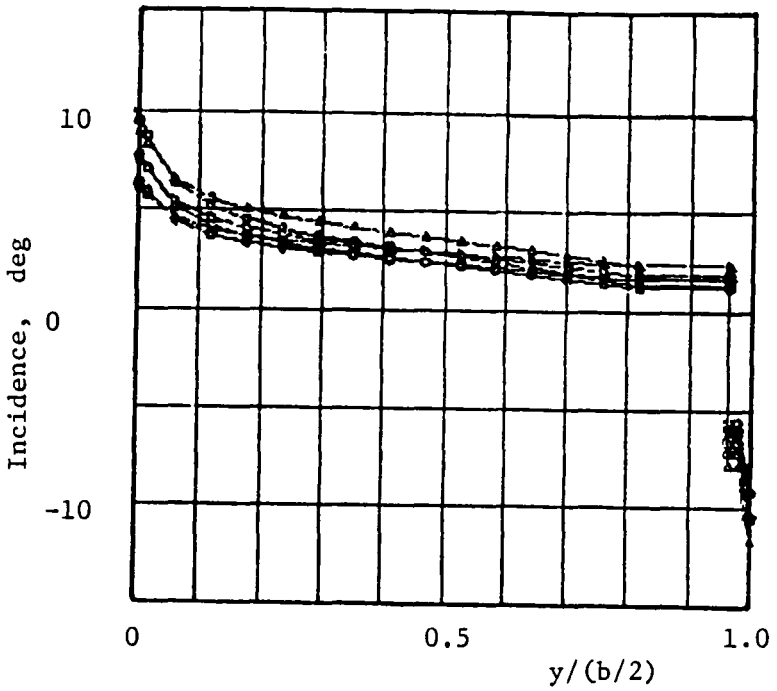

Fig. 2. Incidence distributions for linear theory minimum induced drag designs at M = 0.8, $C_L \cong 0.3$ for configurations of Table 1:
c) Wing-winglet after modification

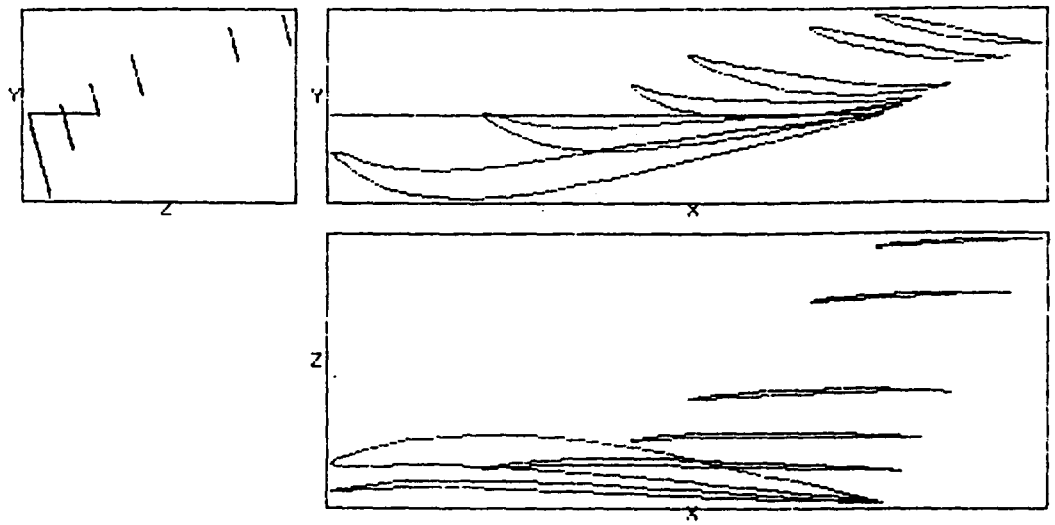

A

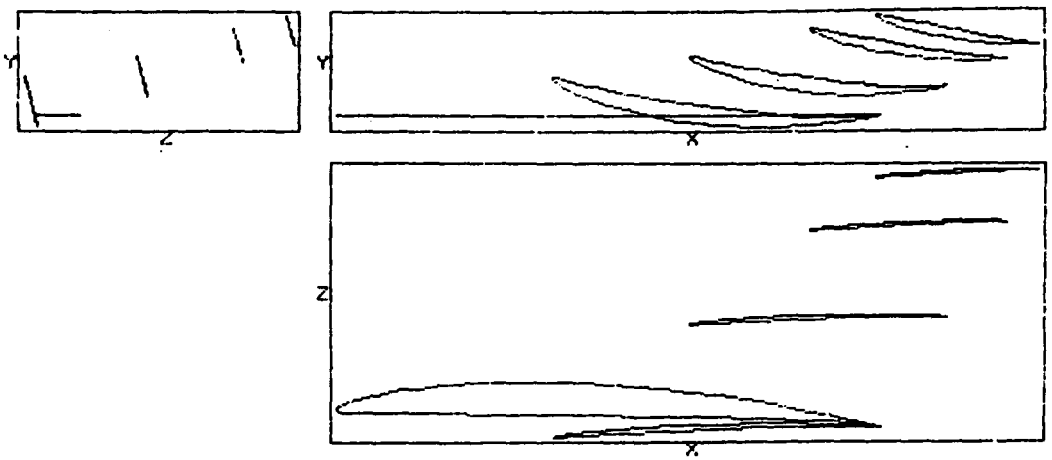

B

Fig. 3. Wing tip-winglet geometry for wing G (A = 2.20, Λ = 50°, λ = 0.2) fitted with 0.15(b/2) winglet:
a) Original geometry
b) Modified geometry

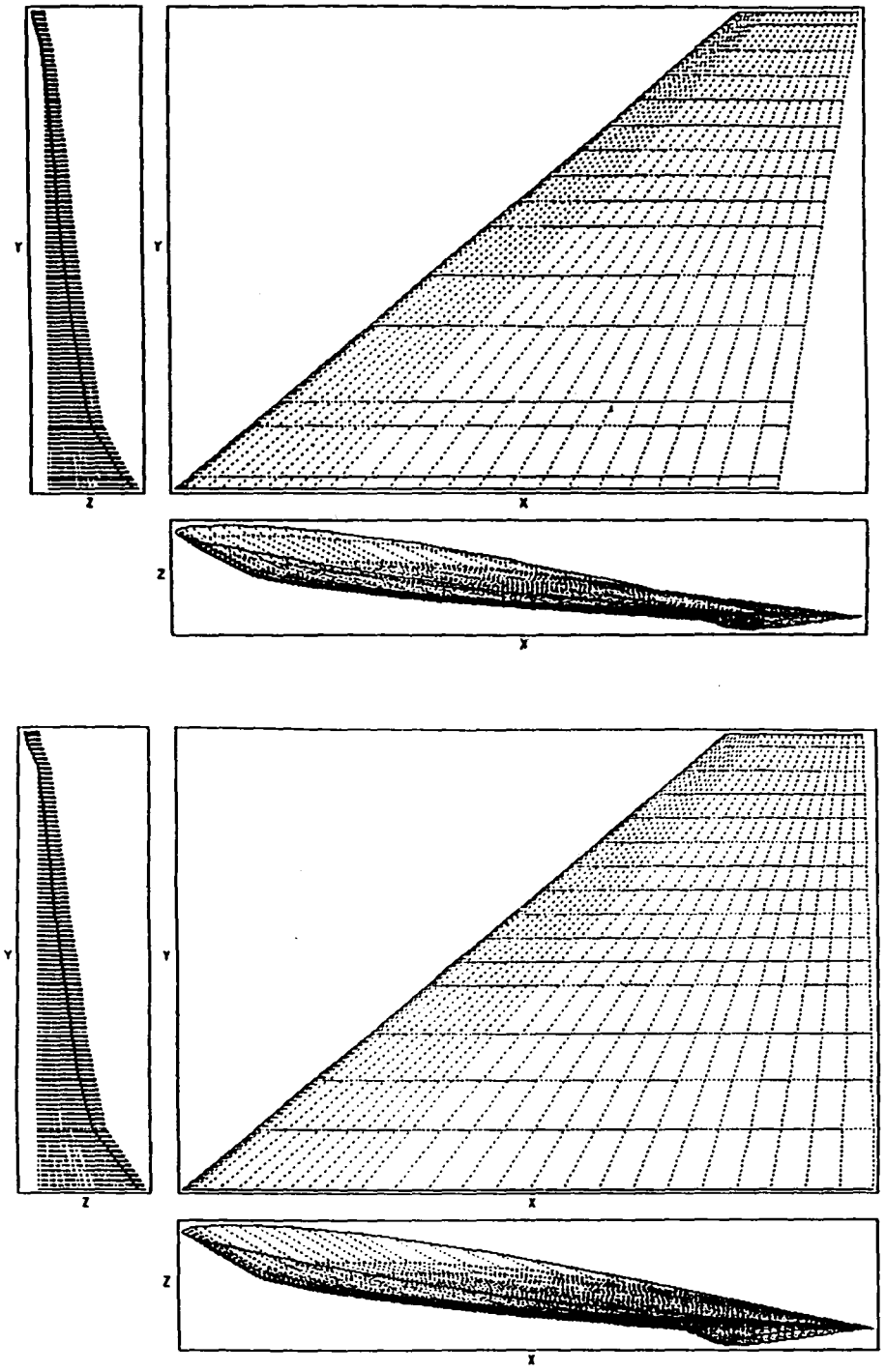

Fig. 4. Wing-alone geometry for M = 0.8, $C_L \cong 0.3$:
a) Wing A (A = 2.63, Λ = 50°, λ = 0.2)
b) Wing G (A = 2.20, Λ = 50°, λ = 0.2)

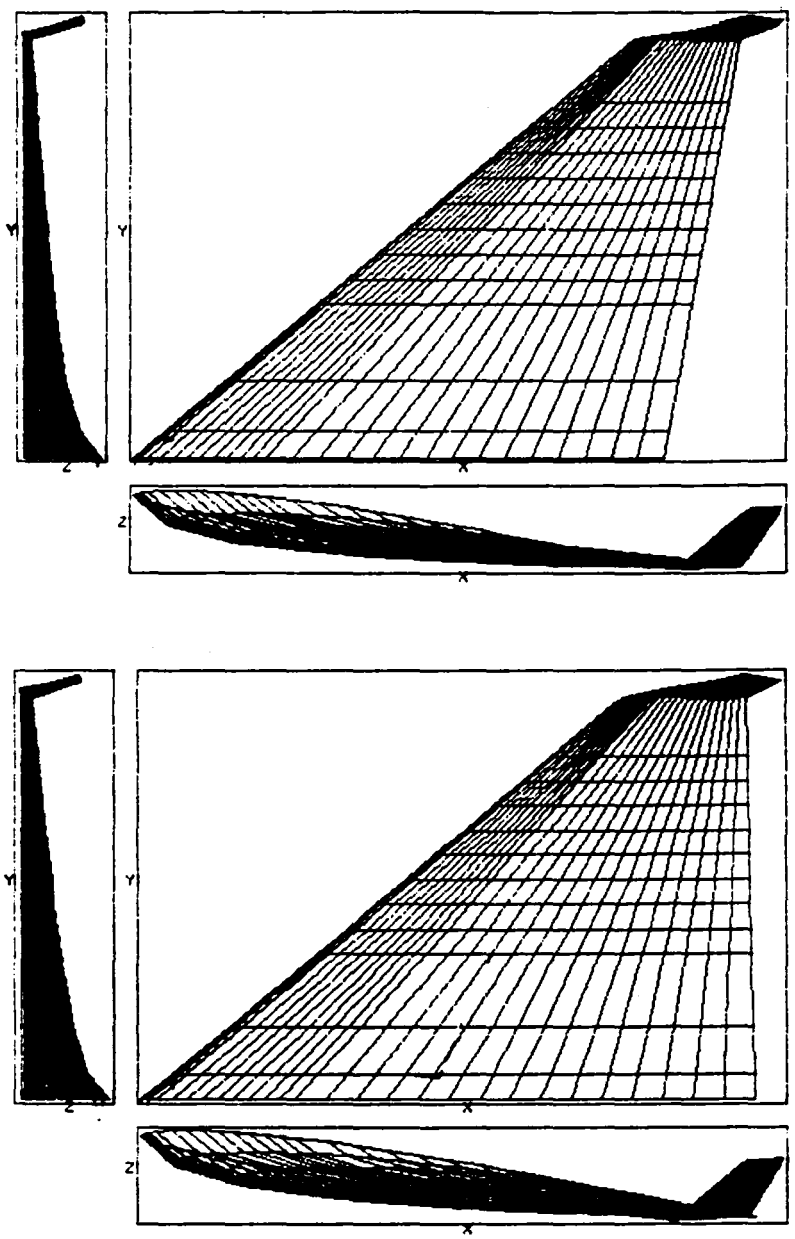

Fig. 5. Wing-winglet geometry for M = 0.8, $C_L \cong 0.3$; 0.15(b/2) winglets:
a) wing A (A = 2.63, Λ = 50°, λ = 0.2)
b) wing G (A = 2.20, Λ = 50°, λ = 0.2)

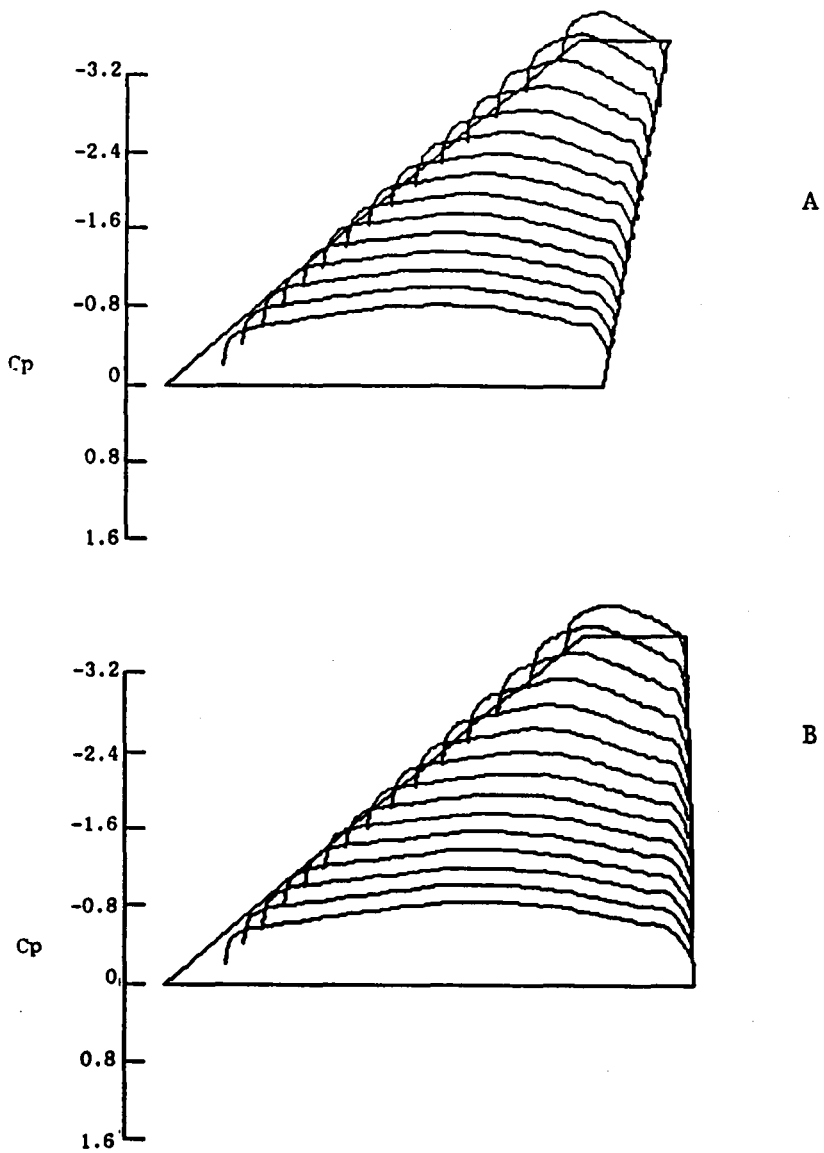

Fig. 6. Calculated upper surface pressure coefficient distributions for wing-alone designs at M = 0.8, α = 0.5°, $C_L \approx 0.3$; 160 iterations, no boundary layer:

a) wing A (A = 2.63, Λ = 50°, λ = 0.2)

b) wing G (A = 2.20, Λ = 50°, λ = 0.2)

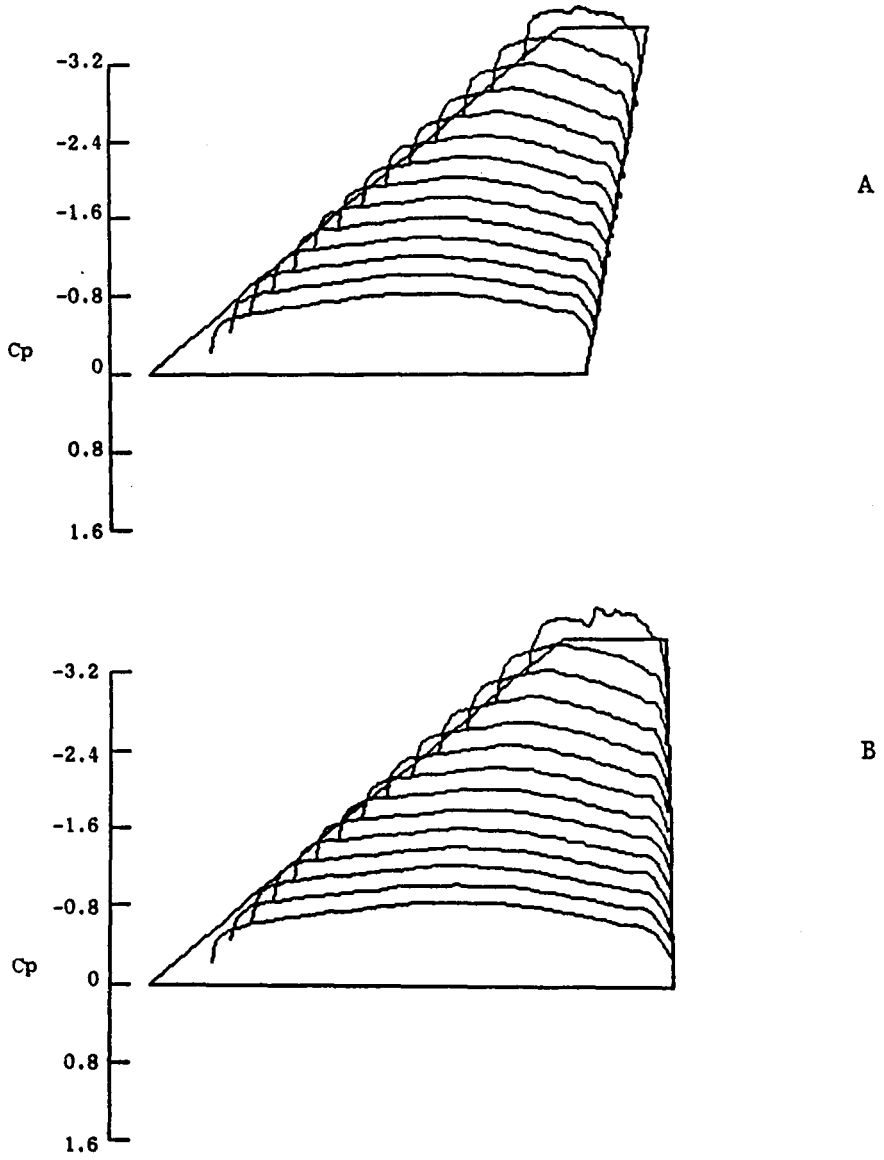

Fig. 7. Calculated upper surface pressure coefficient distributions for wing of wing-winglet designs at M = 0.8, α = 0.5°, $C_L \cong 0.3$; 160 iterations, no boundary layer:

a) wing A (A = 2.63, Λ = 50°, λ = 0.2)
b) wing G (A = 2.20, Λ = 50°, λ = 0.2)

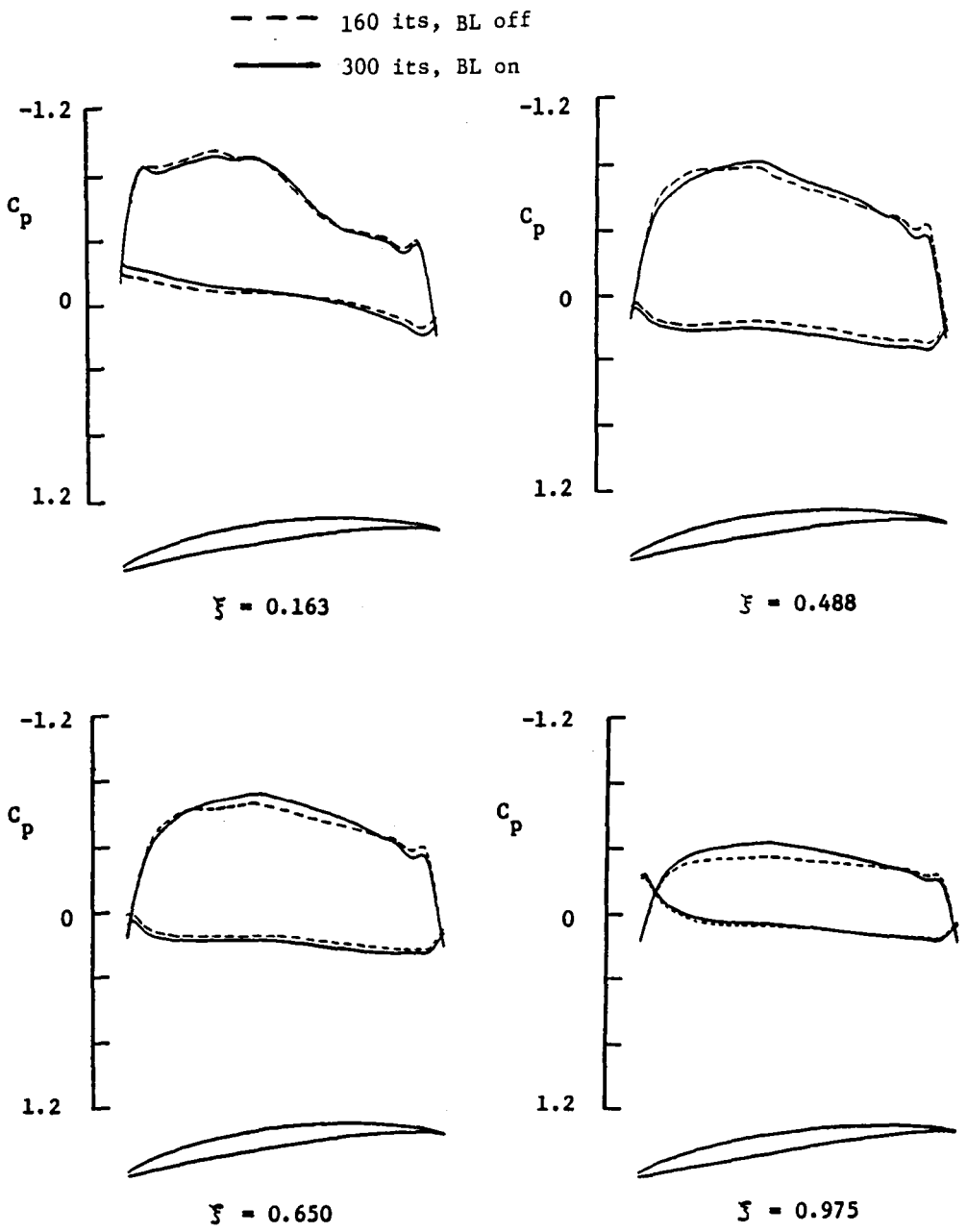

Fig. 8. Calculated winglet pressure coefficient distributions for wing A fitted with 0.15(b/2) winglet at M = 0.8, α = 0.5°, $C_L \cong 0.3$.

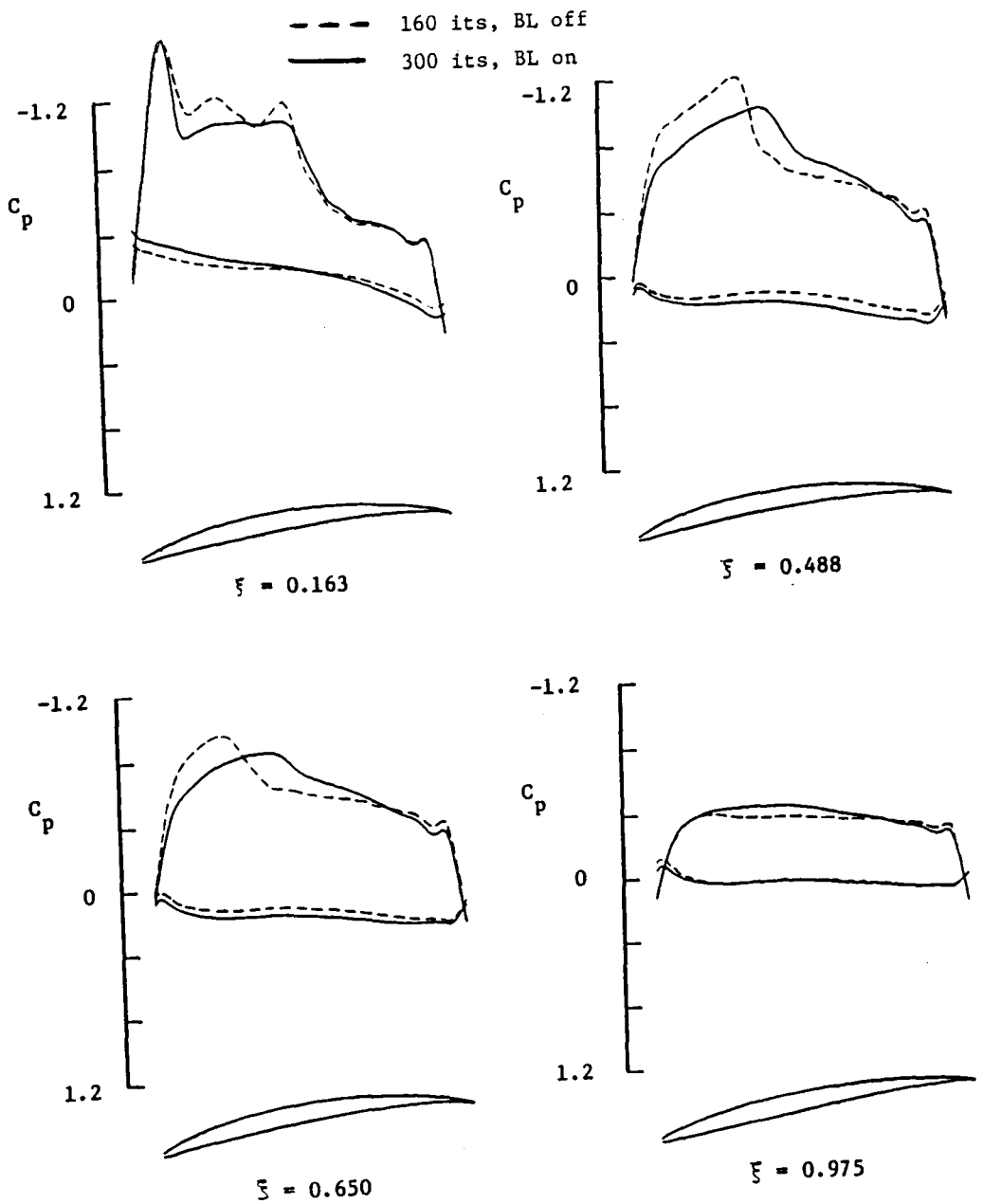

Fig. 9. Calculated winglet pressure coefficient distributions for wing G fitted with 0.15(b/2) winglet at M = 0.8, α = 0.5°, $C_L \cong 0.3$.

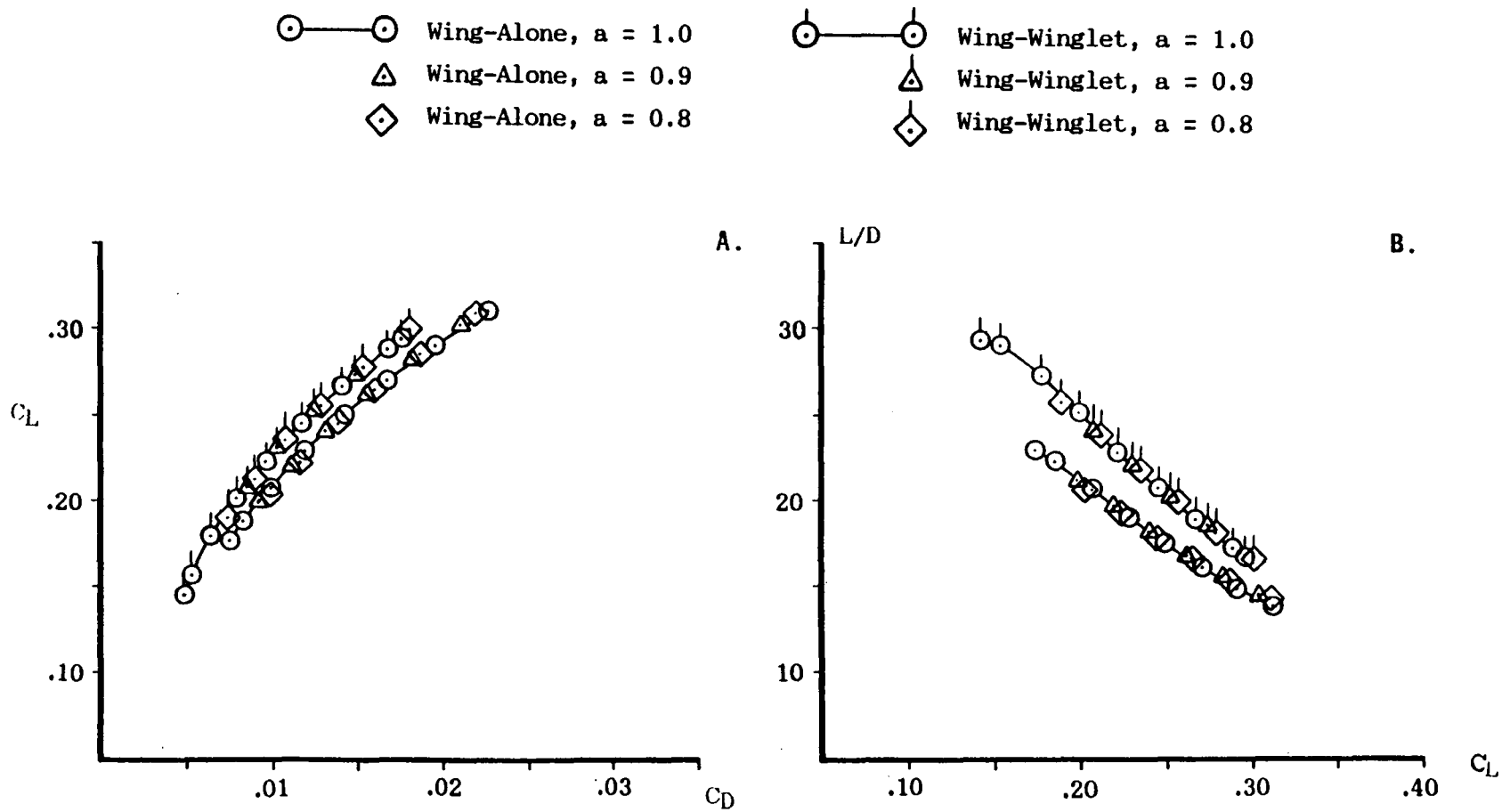

Fig. 10 Predicted performance of wing-alone and wing-winglet F ($A = 2.20$, $\Lambda = 45^{o}$) at $M = 0.8$; 300 iterations with boundary layer interaction, for various chord loading shape functions

a) C_L versus C_D

b) L/D_{tot} versus C_L

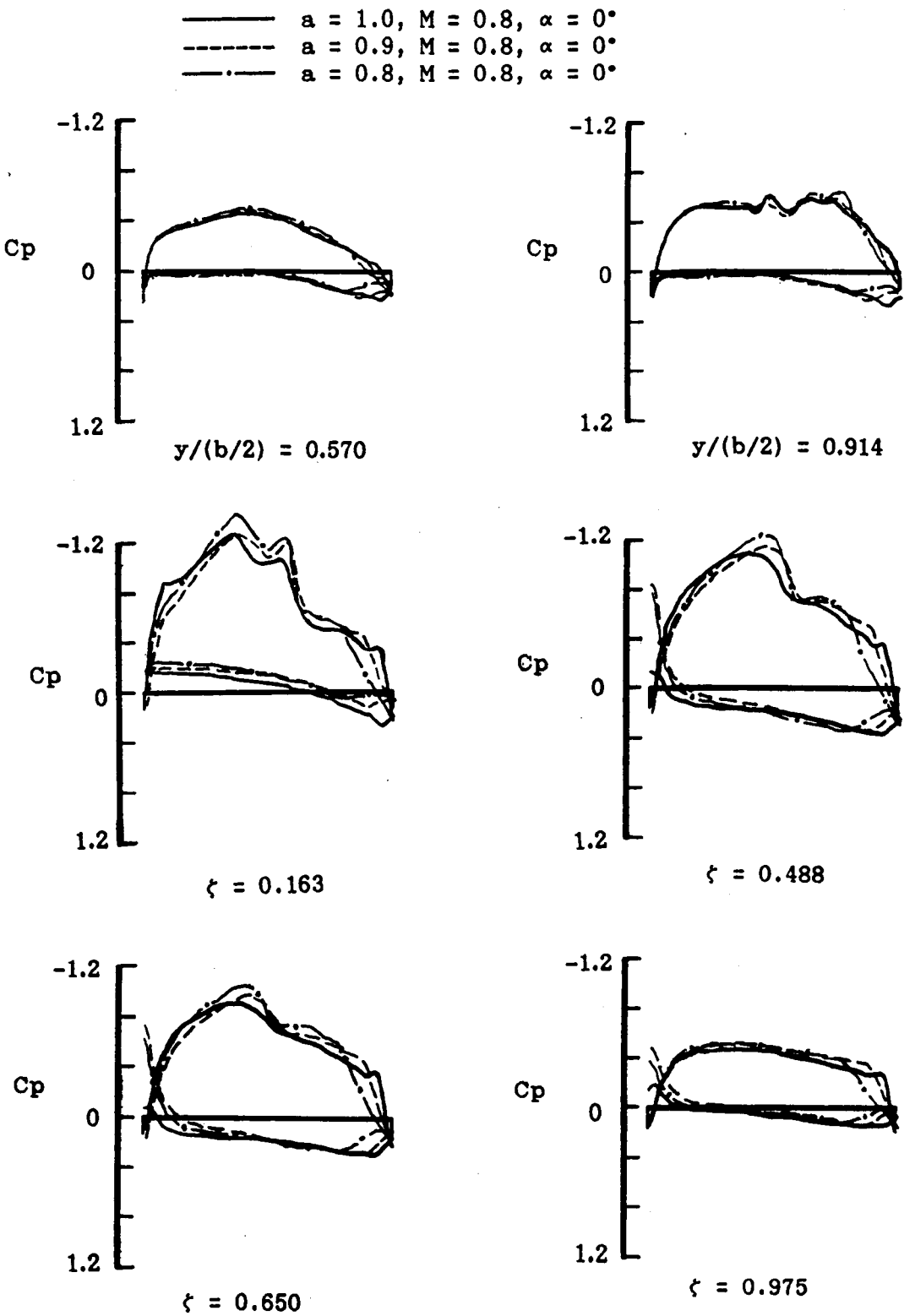

Fig. 11 Calculated wing and winglet pressure coefficient distributions for wing F fitted with 0.15 (b/2) winglet at M = 0.8, $C_L \cong 0.27$, for various chord loading shape functions.

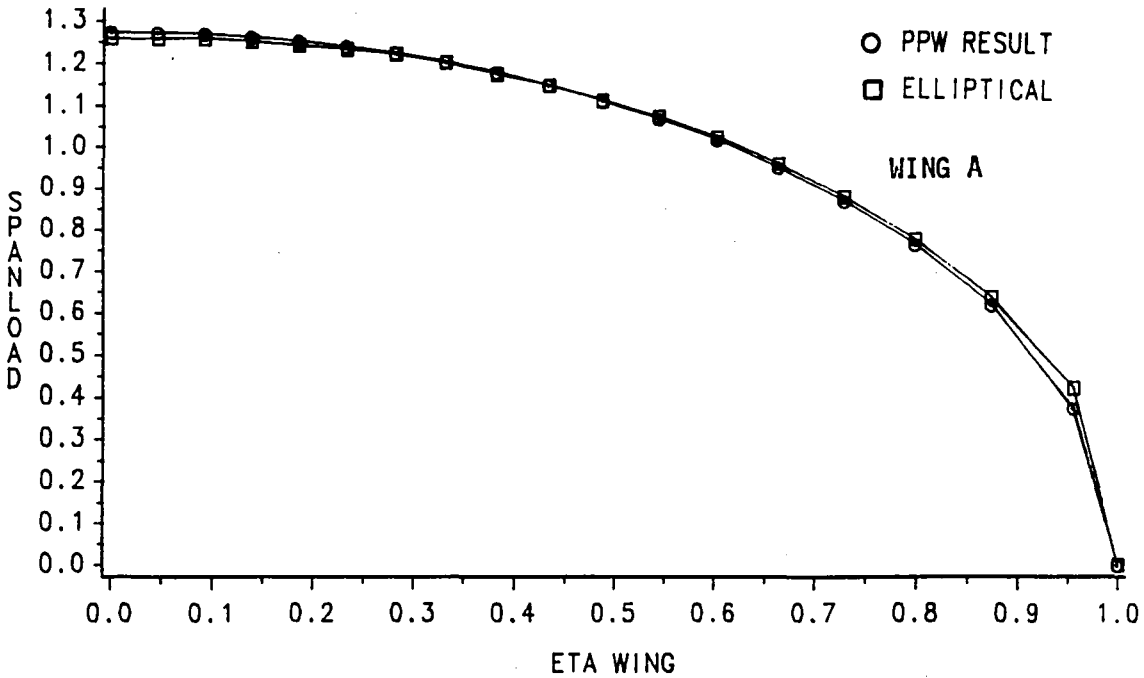

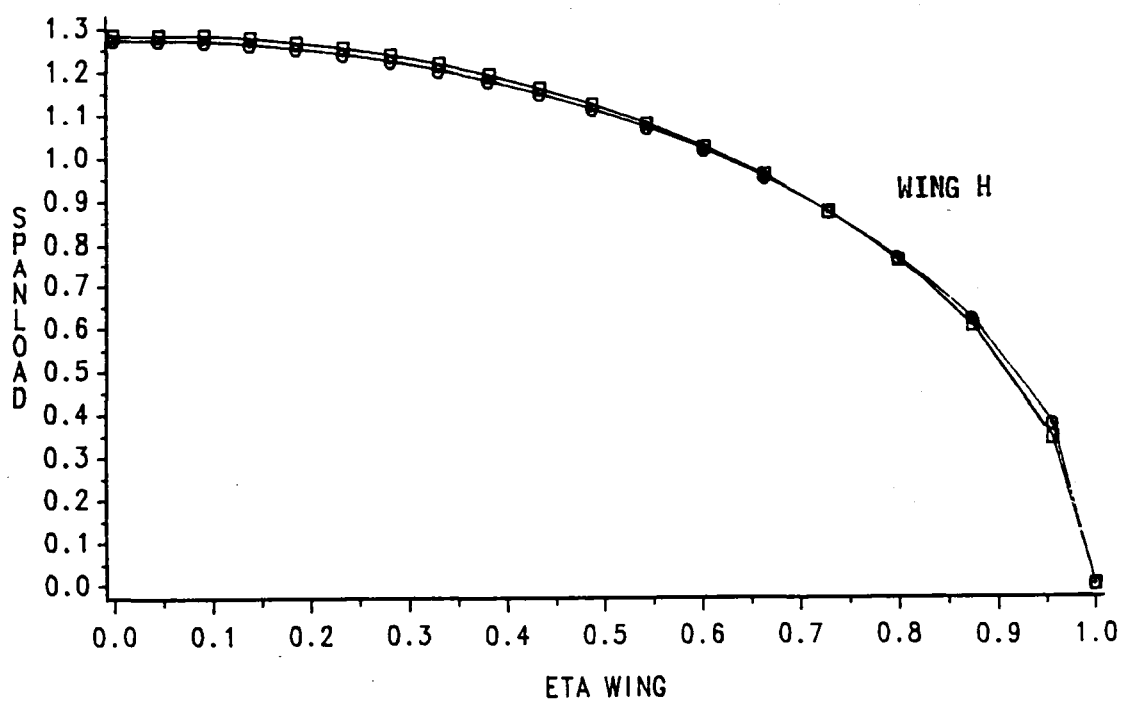

Fig. 12. Calculated PPW spanload for wing-alone geometries A and H without fuselage at M = 0.8, α = 0.5° (C_L = 0.397).

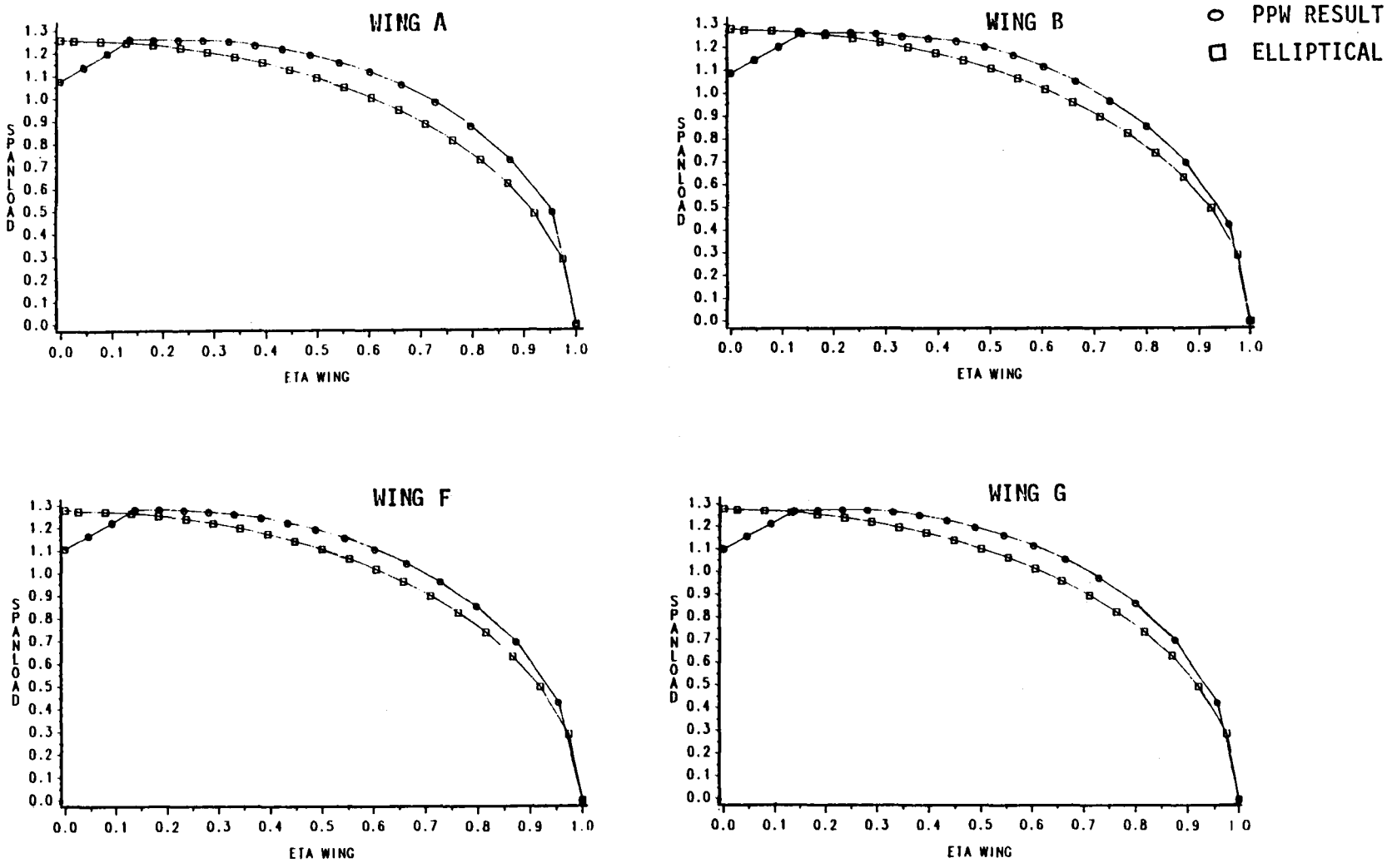

Fig. 13. Calculated PPW spanloads for wing-alone geometries, A, B, F, and G with fuselage at M = 0.8, α = 0.5° ($C_L \cong 0.28$).

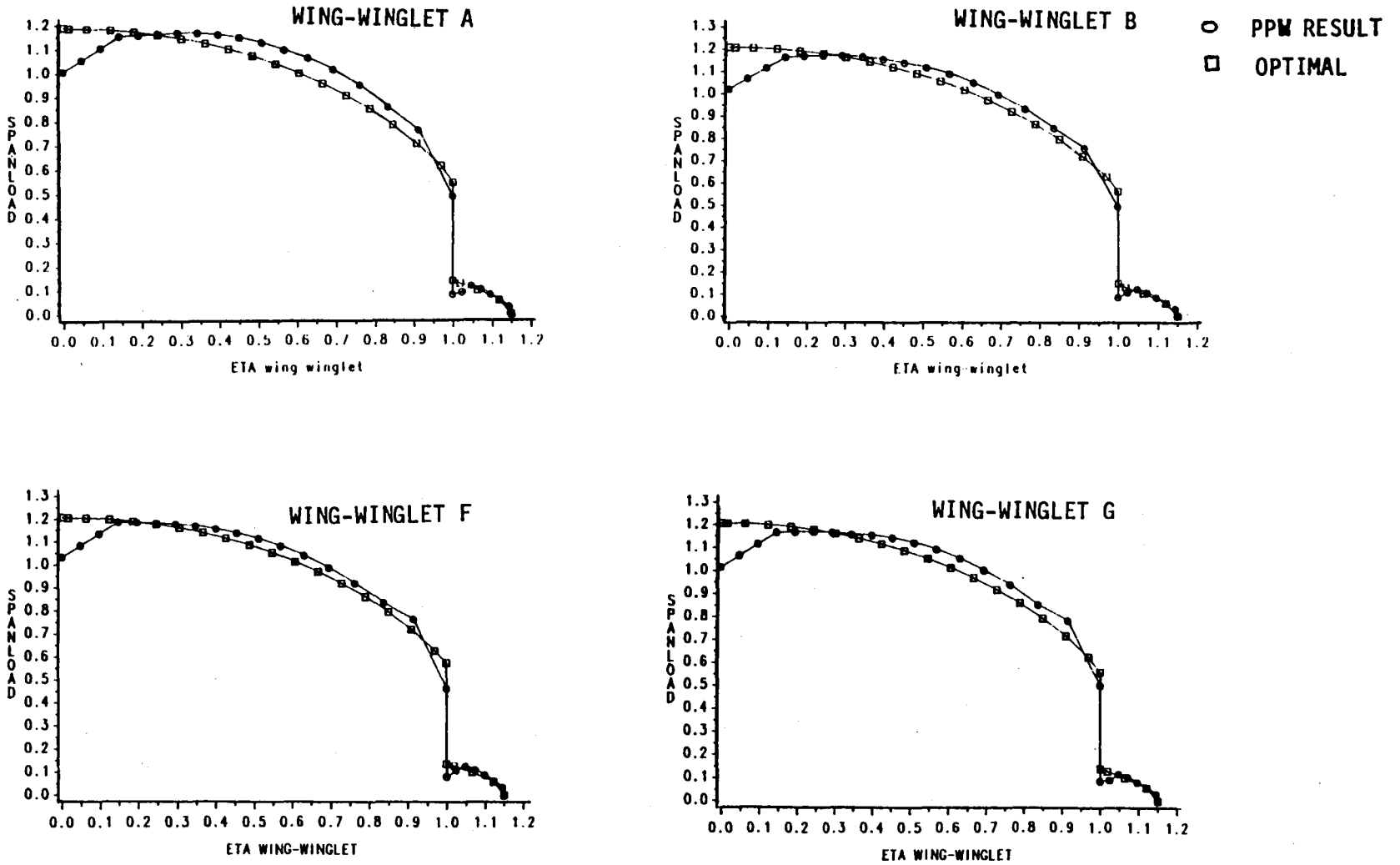

Fig. 14. Calculated PPW spanloads for modified wing-winglet geometries A, B, F, and G with fuselage at M = 0.8, α = 0.5° ($C_L \cong 0.28$).

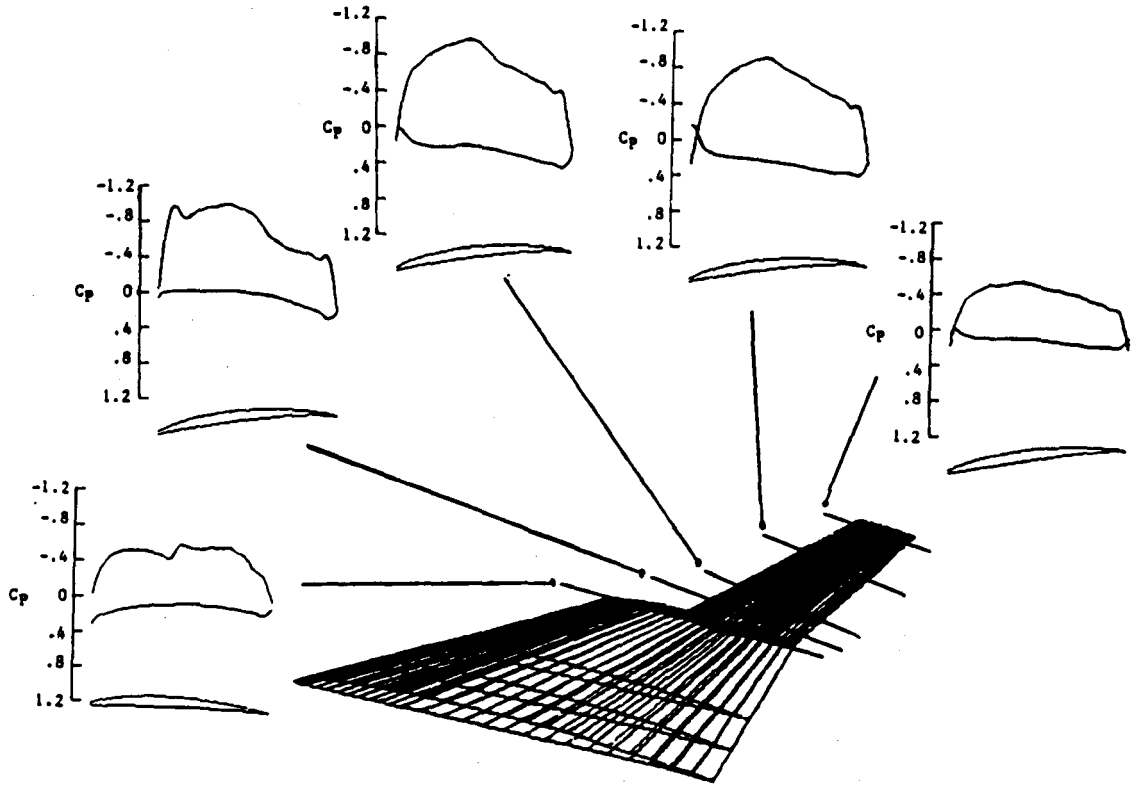

Fig. 15. Calculated pressure coefficient distributions for wing H (A = 2.20, Λ = 55°, λ = 0.2) fitted with 0.25(b/2), Λ = 45° winglet at M = 0.8, α = 0.5°, C_L = 0.3; 300 iterations, with boundary layer interaction.

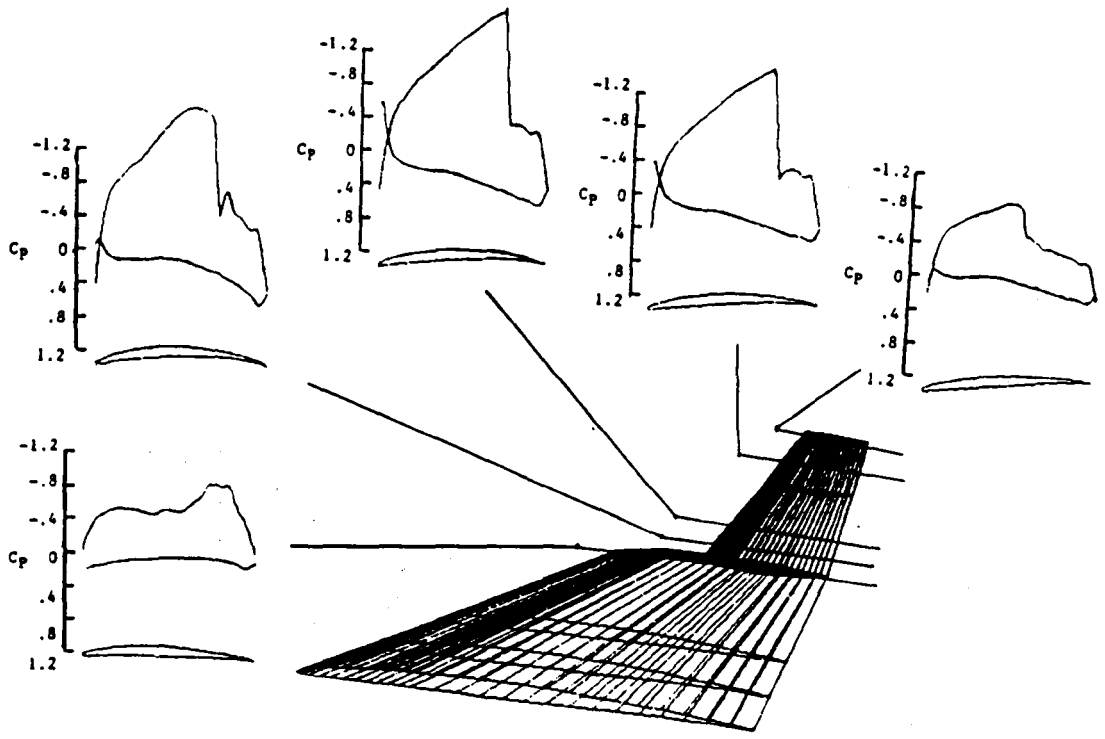

Fig. 16. Calculated pressure coefficient distributions for wing H (A = 2.20, Λ = 55°, λ = 0.2) fitted with 0.25(b/2), λ = 30° winglet at M = 0.8, α = 0.5°, $C_L \cong 0.3$; 300 iterations, with boundary layer interaction.

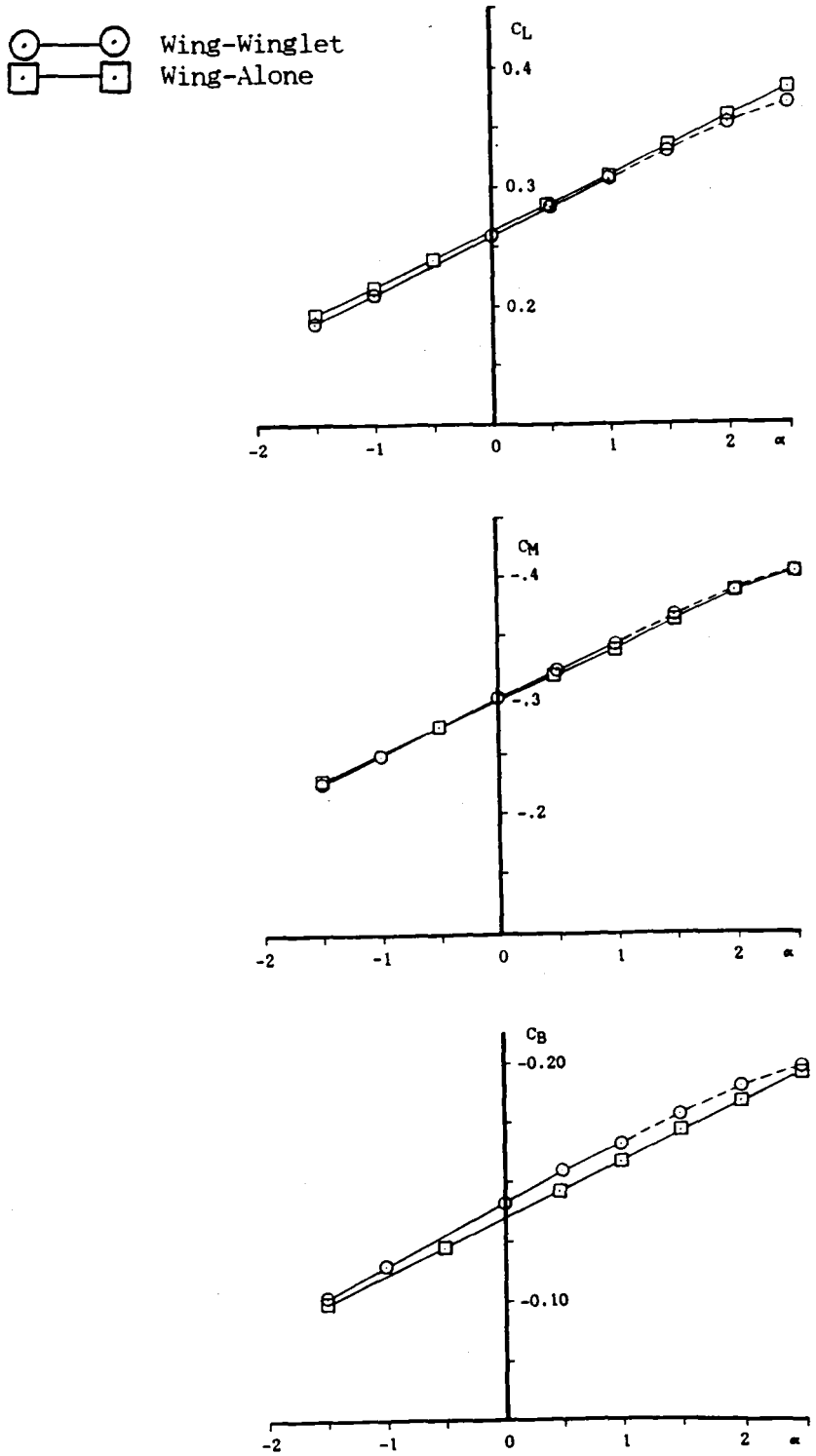

Fig. 17. Predicted performance of wing-alone and wing-winglet A at M = 0.8; 300 iterations with boundary layer interaction:

a) C_L versus α
b) C_m versus α
c) C_B versus α

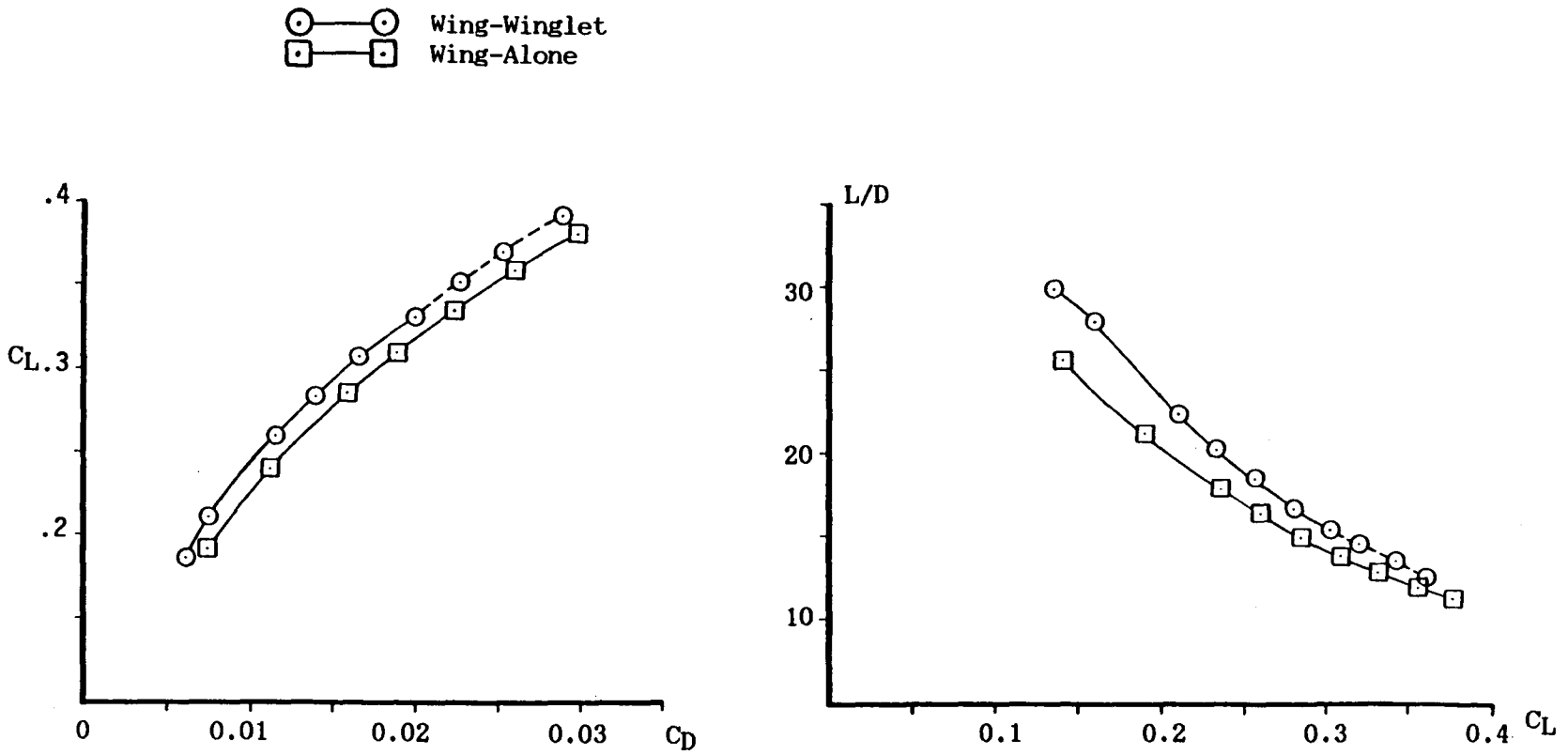

Fig. 17. Predicted performance of wing-alone and wing-winglet A at M = 0.8; 300 iterations with boundary layer interaction:
d) C_L versus C_D
e) L/D_{tot} versus C_L

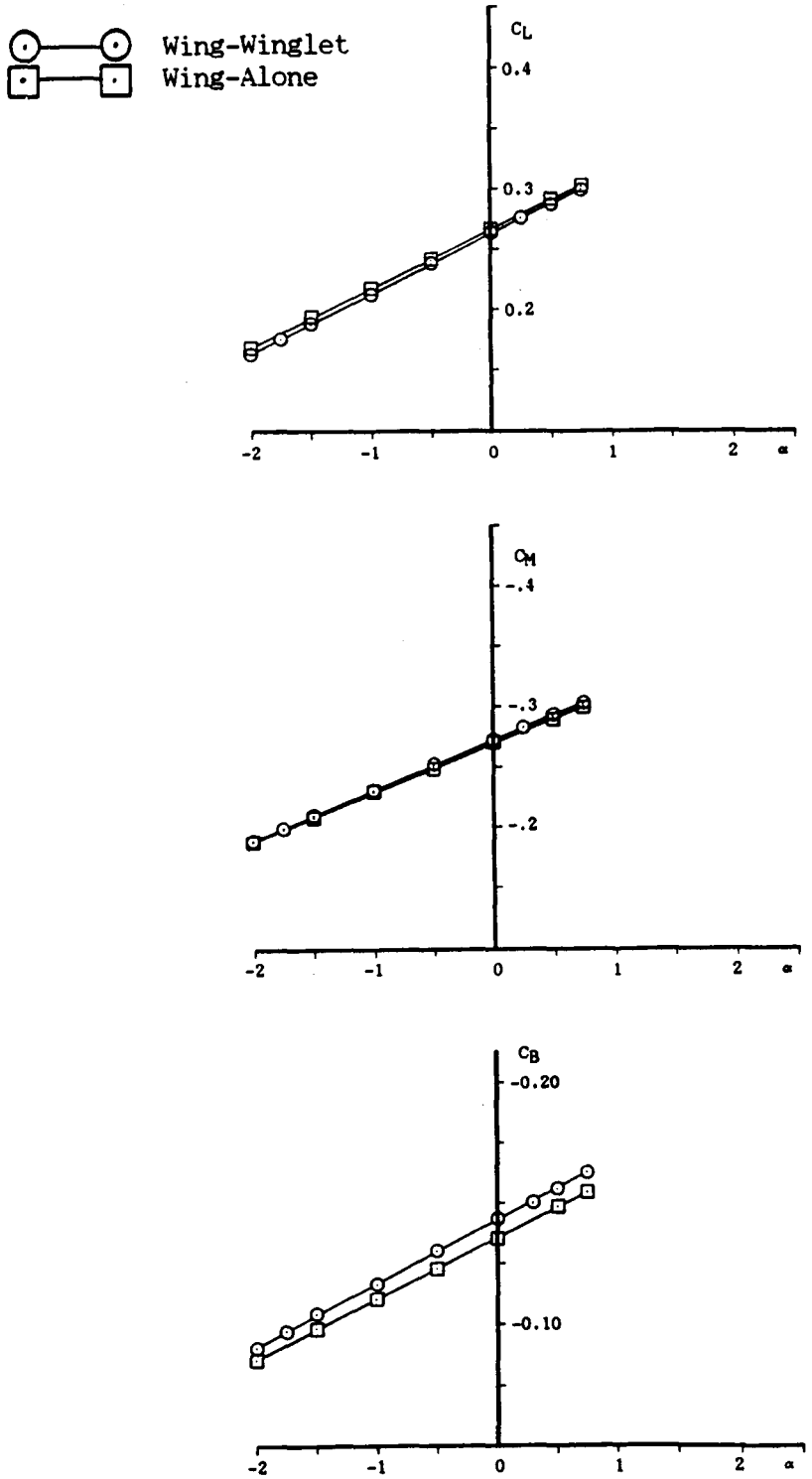

Fig. 18. Predicted performance of wing-alone and wing-winglet B at M = 0.8; 300 iterations with boundary layer interaction:

a) C_L versus α
b) C_m versus α
c) C_B versus α

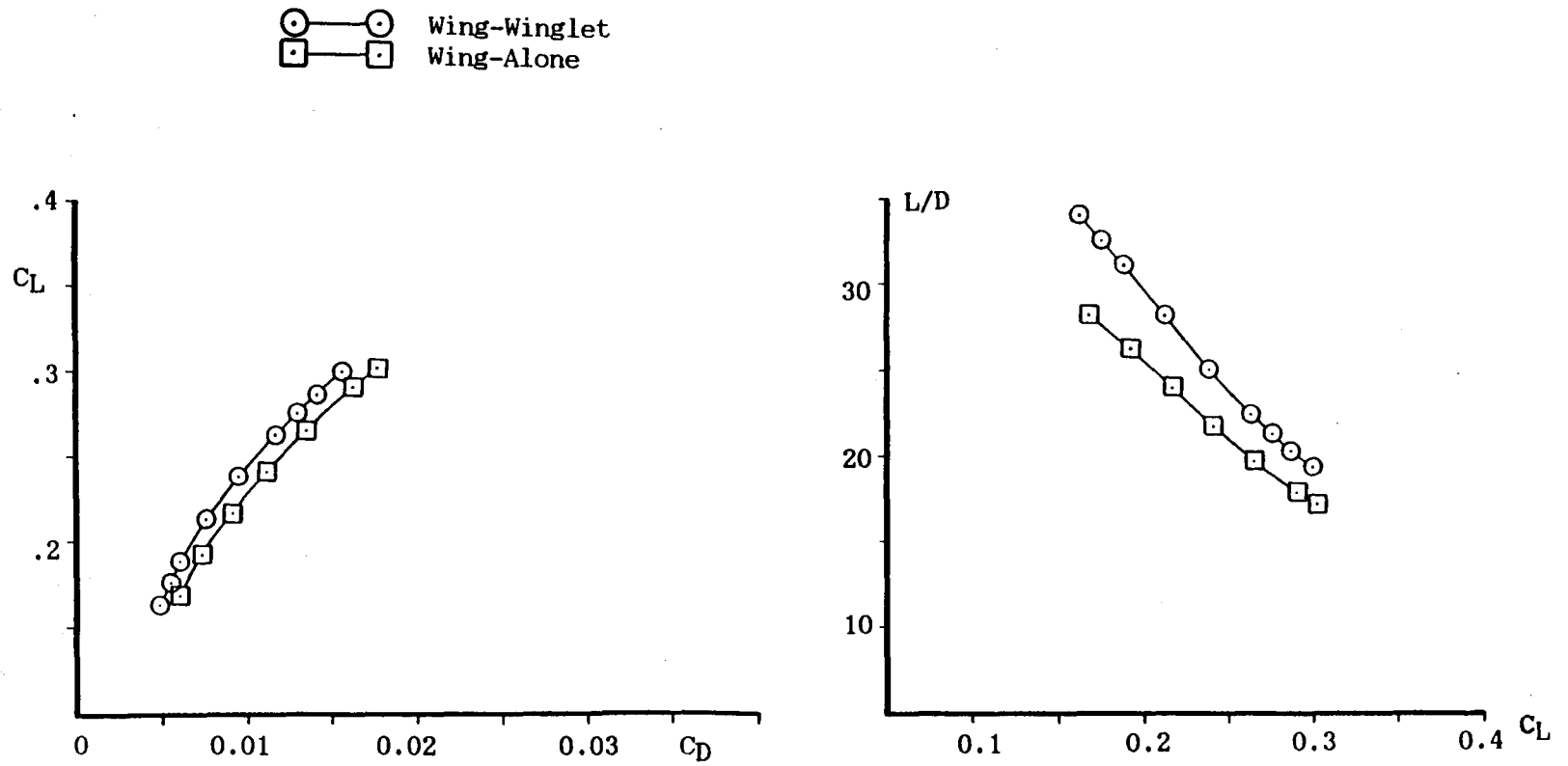

Fig. 18. Predicted performance of wing-alone and wing-winglet B at M = 0.8; 300 iterations with boundary layer interaction:
d) C_L versus C_D
e) L/D_{tot} versus C_L

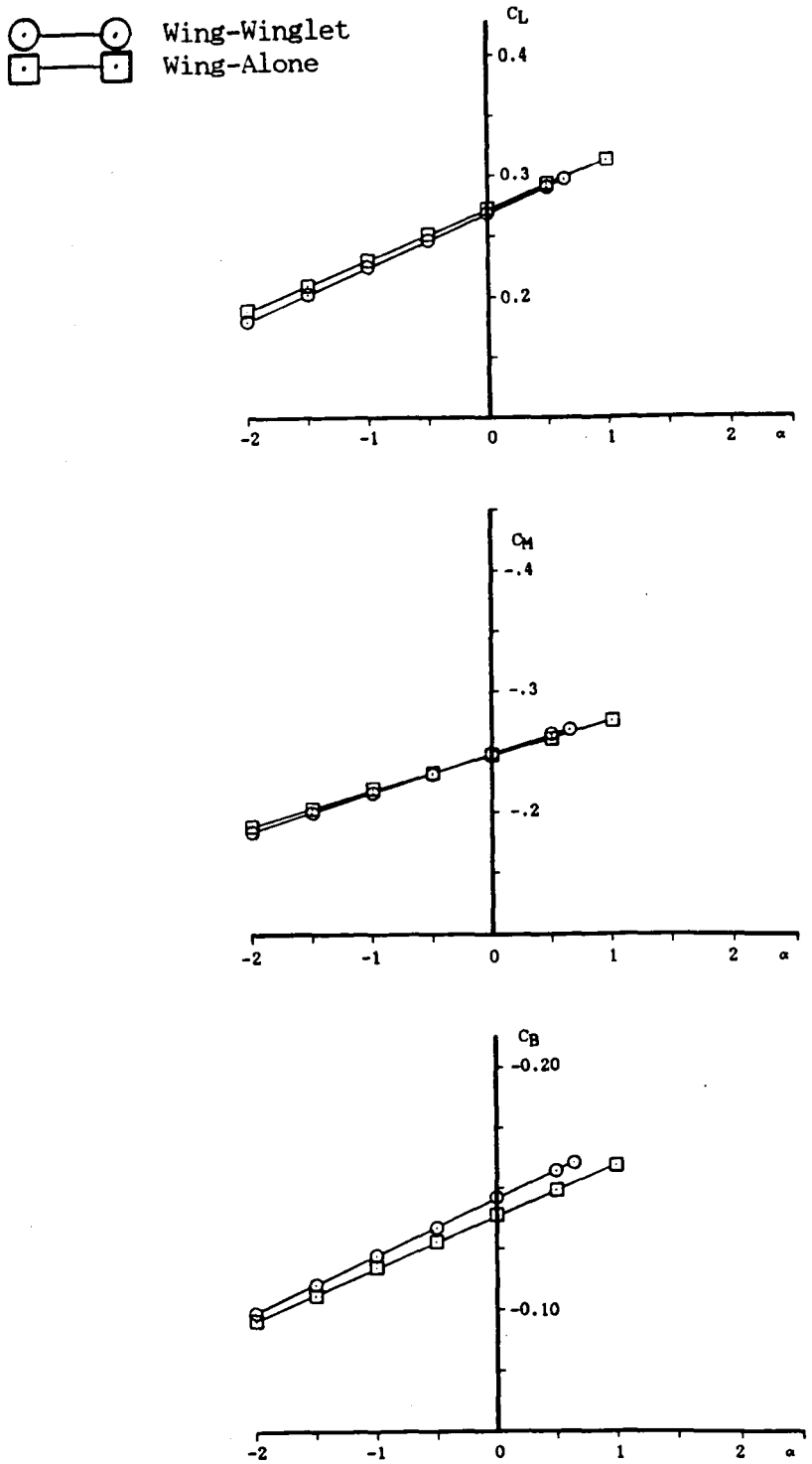

Fig. 19. Predicted performance of wing-alone and wing-winglet F at M = 0.8; 300 iterations with boundary layer interaction:

a) C_L versus α
b) C_m versus α
c) C_B versus α

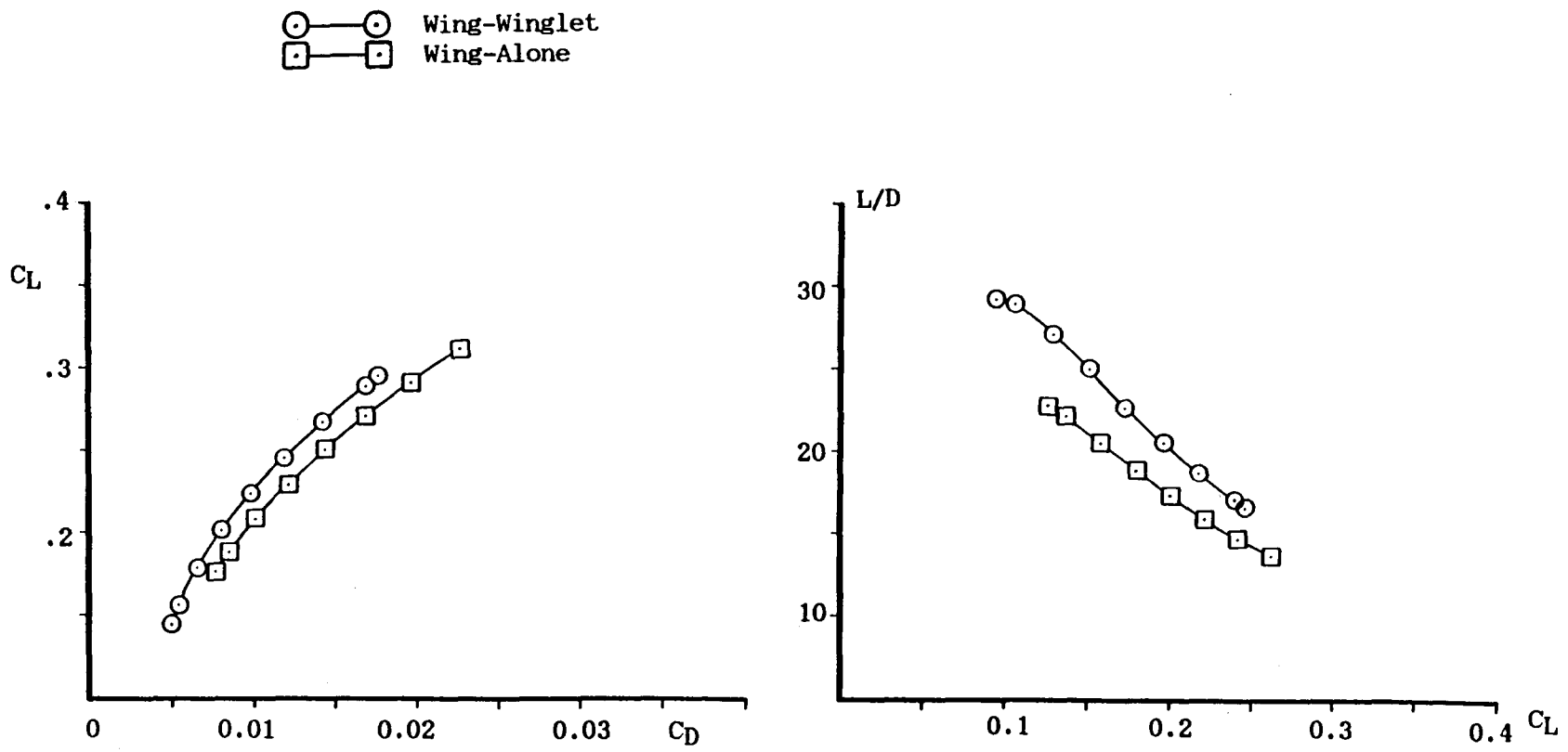

Fig. 19. Predicted performance of wing-alone and wing-winglet F at M = 0.8; 300 iterations with boundary layer interaction:
d) C_L versus C_D
e) L/D_{tot} versus C_L

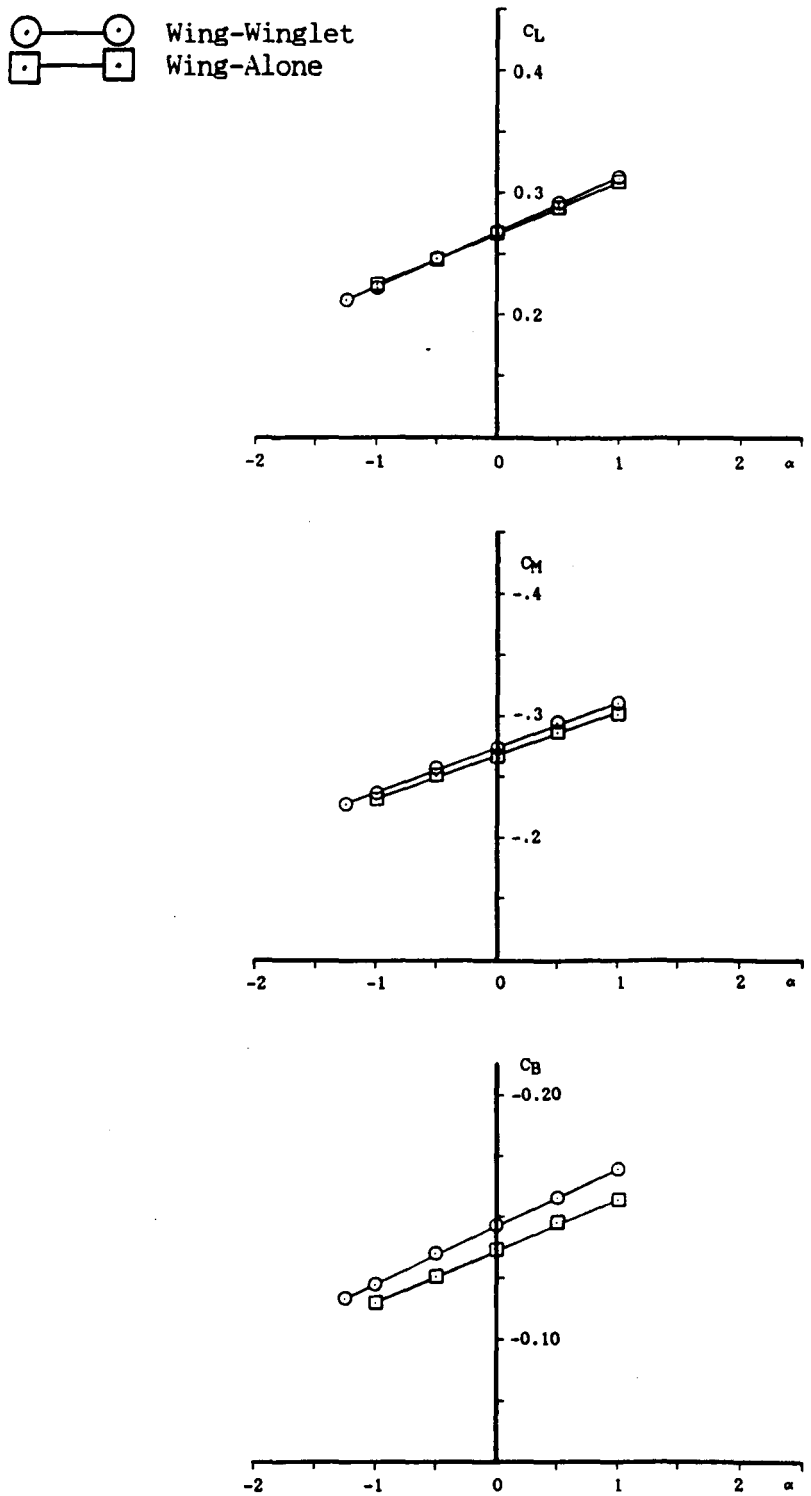

Fig. 20. Predicted performance of wing-alone and wing-winglet G at M = 0.8; 300 iterations with boundary layer interaction:

a) C_L versus α
b) C_m versus α
c) C_B versus α

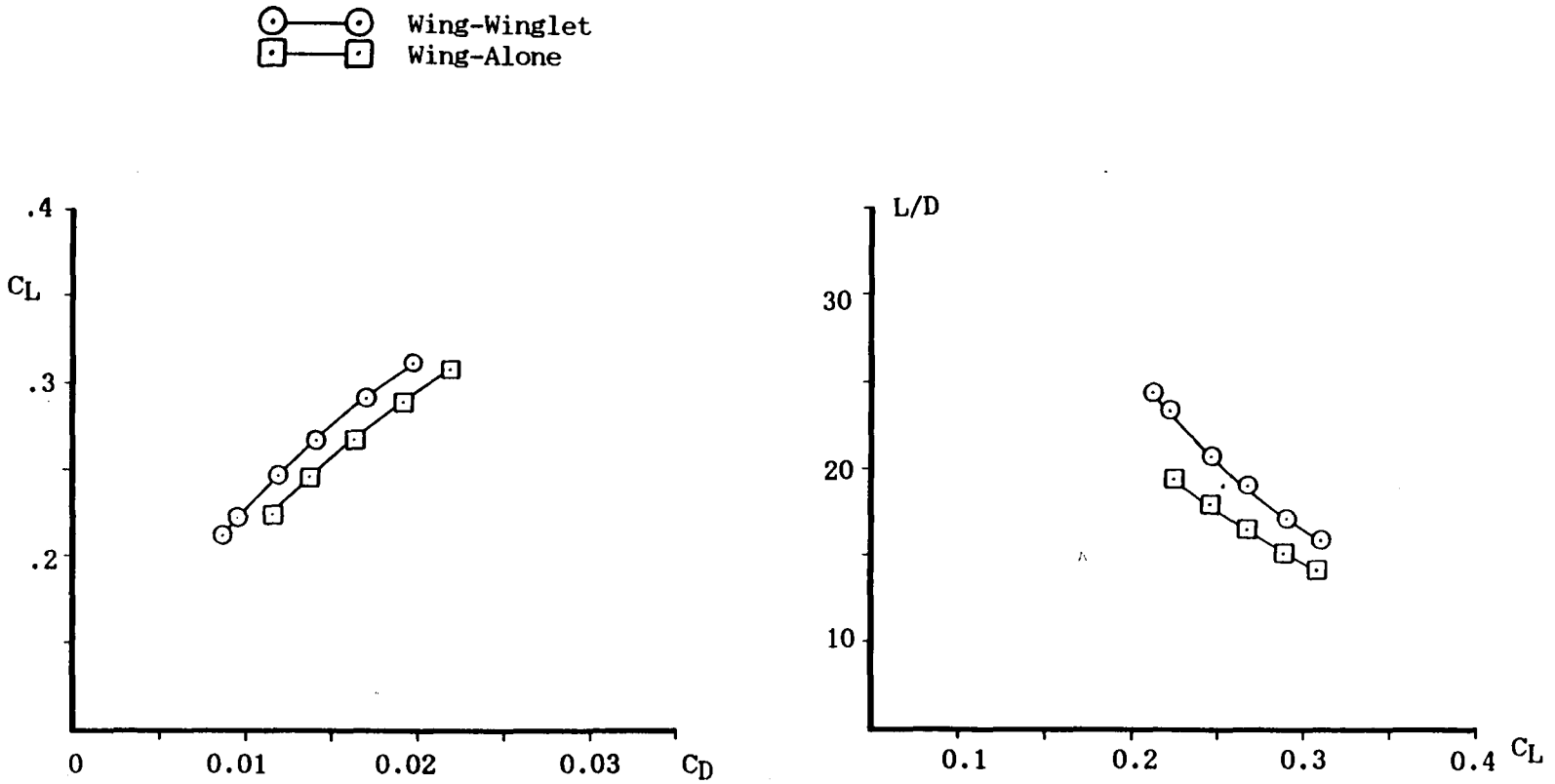

Fig. 20. Predicted performance of wing-alone and wing-winglet G at M = 0.8; 300 iterations with boundary layer interaction:
d) C_L versus C_D
e) L/D_{tot} versus C_L

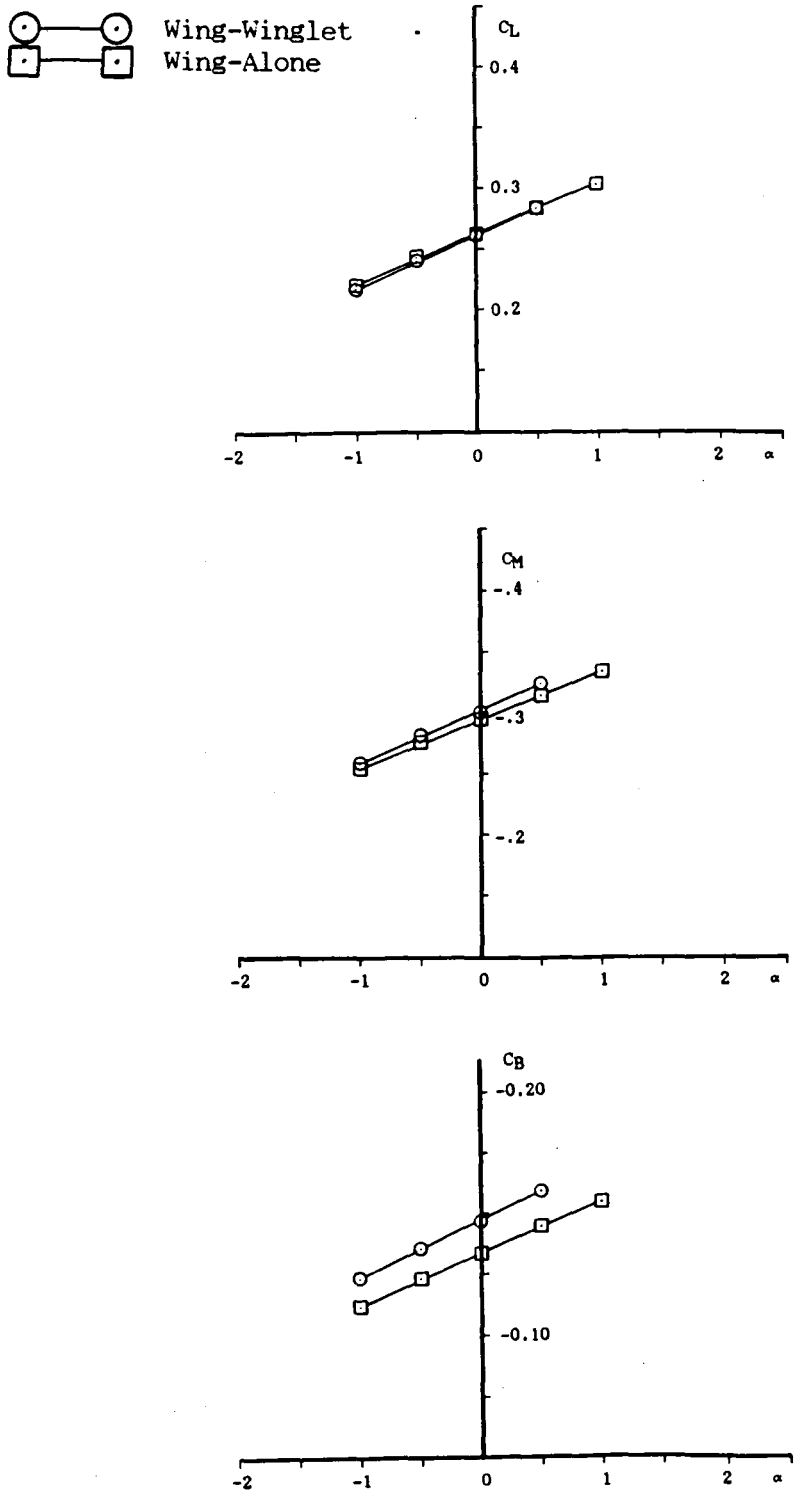

Fig. 21. Predicted performance of wing-alone and wing-winglet H fitted with 0.25(b/2), Λ = 45° winglet at M = 0.8; 300 iterations with boundary layer interaction:

a) C_L versus α
b) C_m versus α
c) C_B versus α

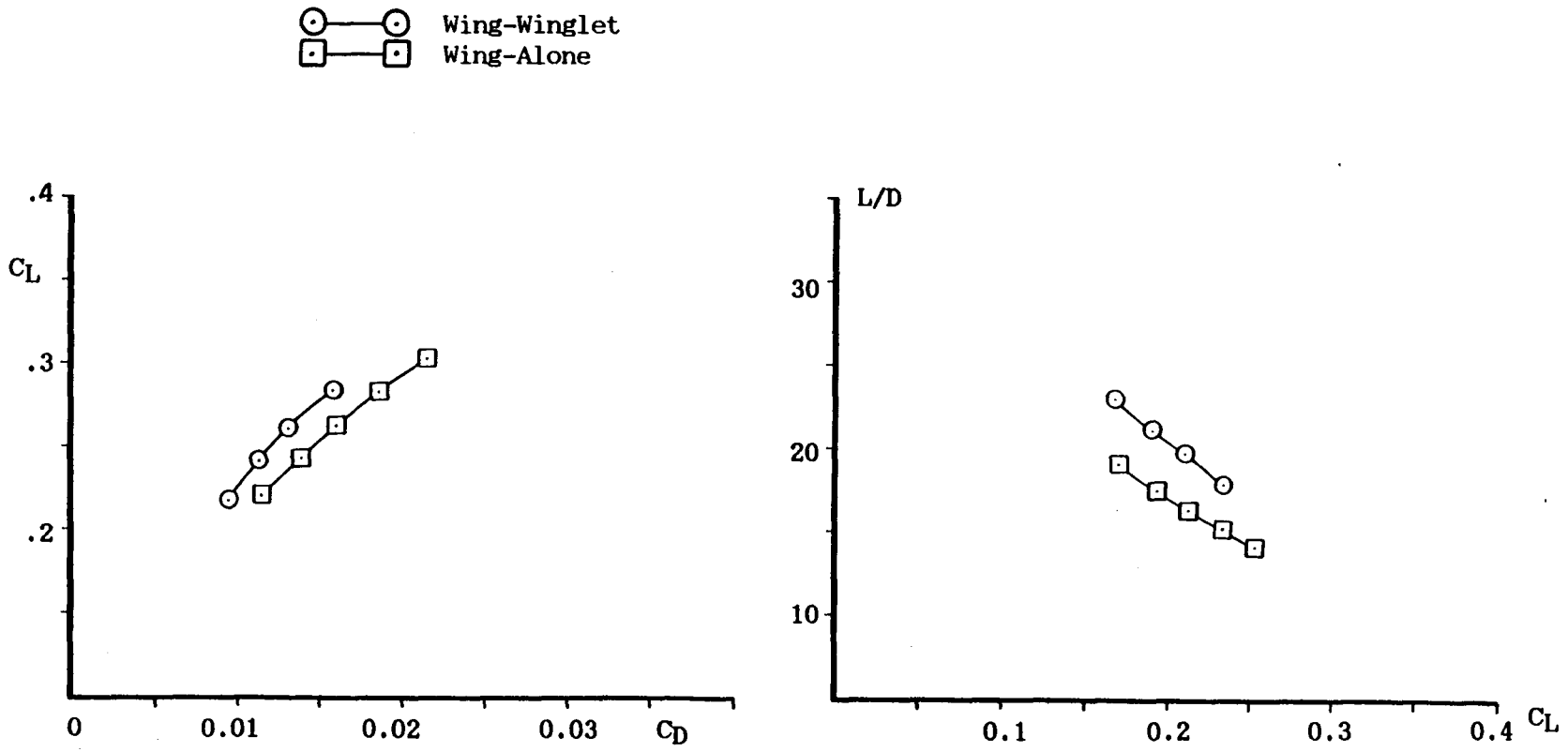

Fig. 21. Predicted performance of wing-alone and wing-winglet H fitted with 0.25(b/2), Λ = 45° winglet at M = 0.8; 300 iterations with boundary layer interaction:

d) C_L versus C_D

e) L/D_{tot} versus C_L

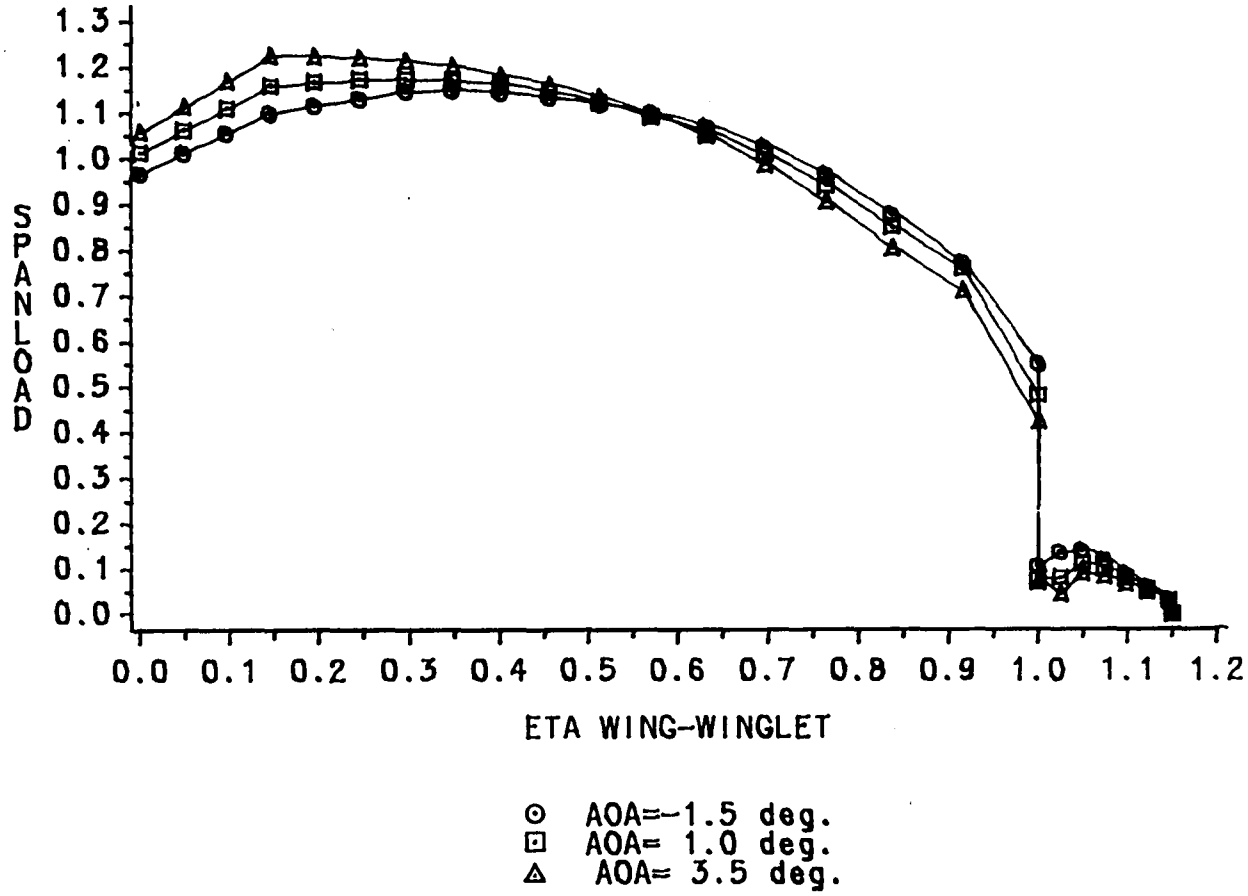

Fig. 22. Calculated PPW spanloads for modified wing-winglet geometry A with fuselage at M = 0.8 versus α.

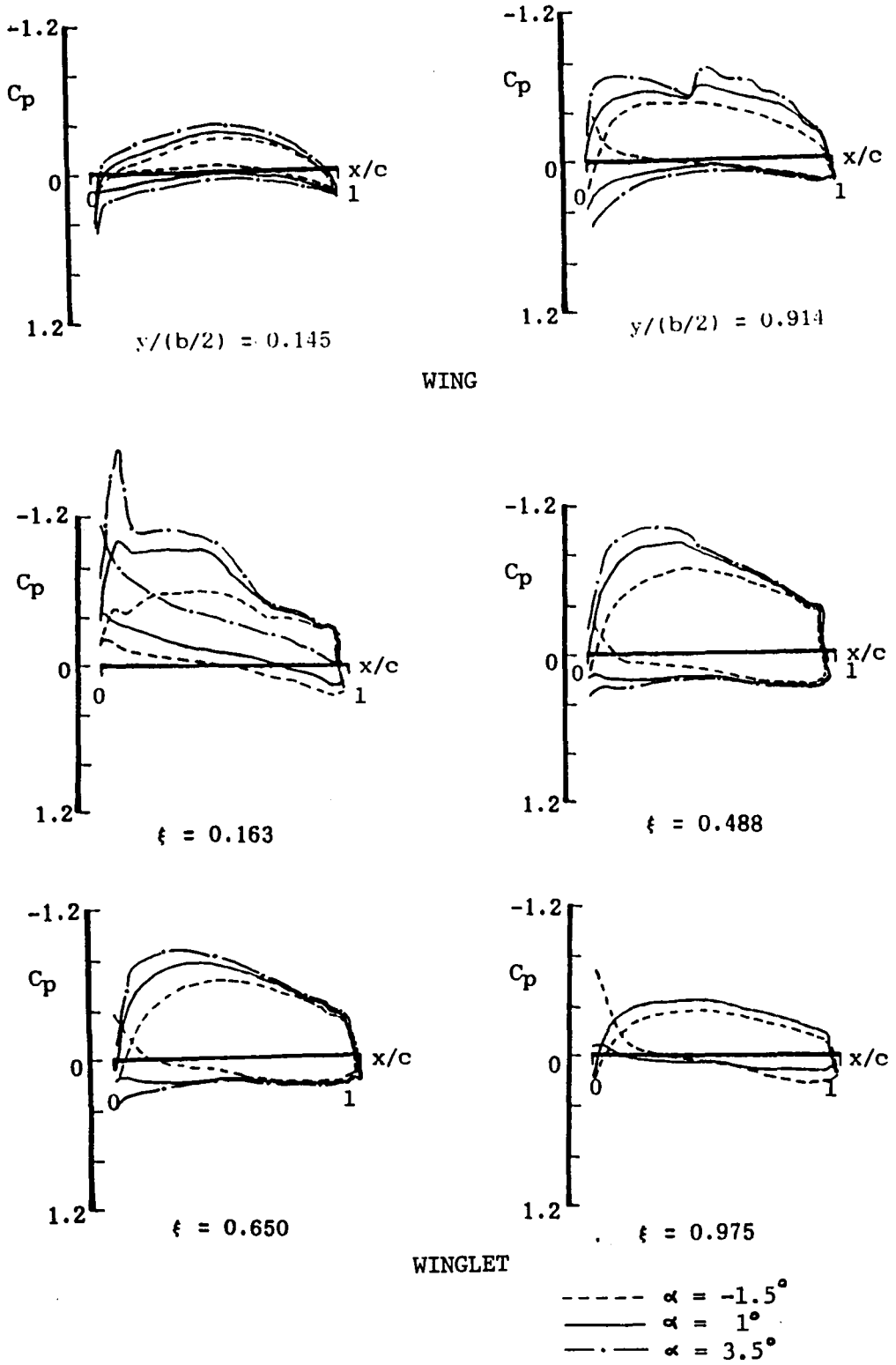

Fig. 23. Calculated wing and winglet pressure coefficient distributions for wing A fitted with 0.15(b/2) winglet at M = 0.8 versus α .

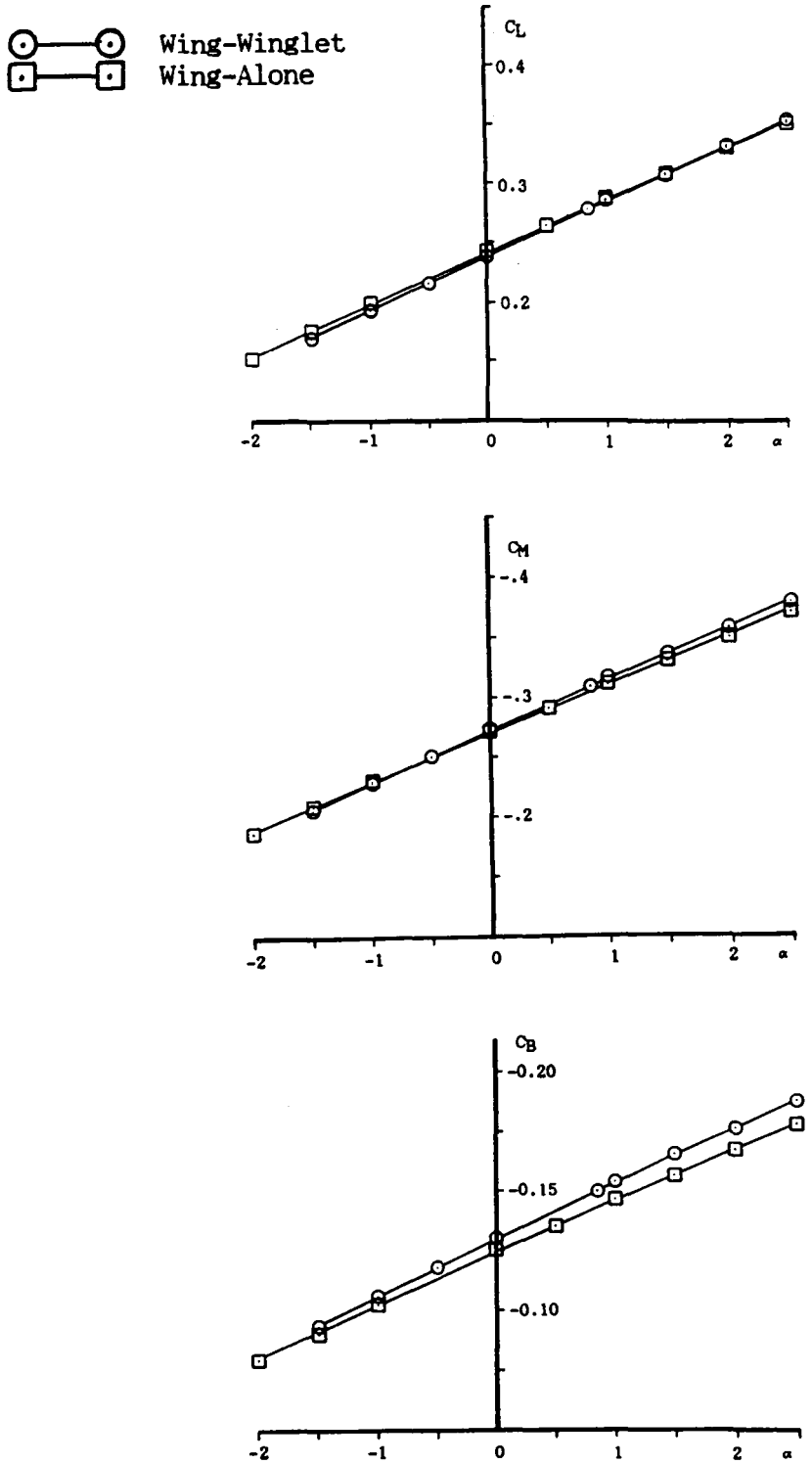

Fig. 24. Predicted performance of wing-alone and wing-winglet A at M = 0.7; 300 iterations with boundary layer interaction:
a) C_L versus α
b) C_m versus α
c) C_B versus α

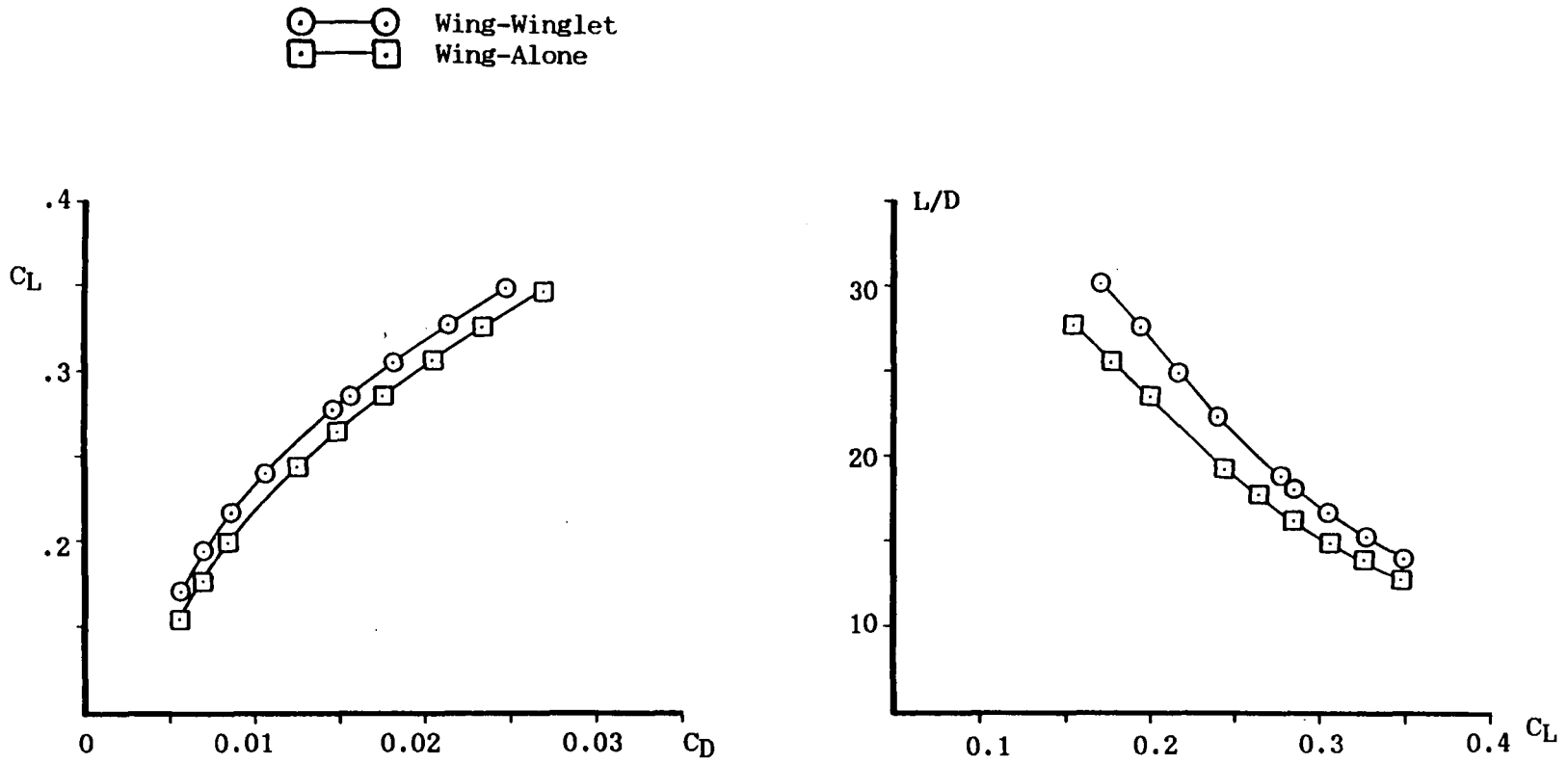

Fig. 24. Predicted performance of wing-alone and wing-winglet A at M = 0.7; 300 iterations with boundary layer interaction:
d) C_L versus C_D
e) L/D_{tot} versus C_L

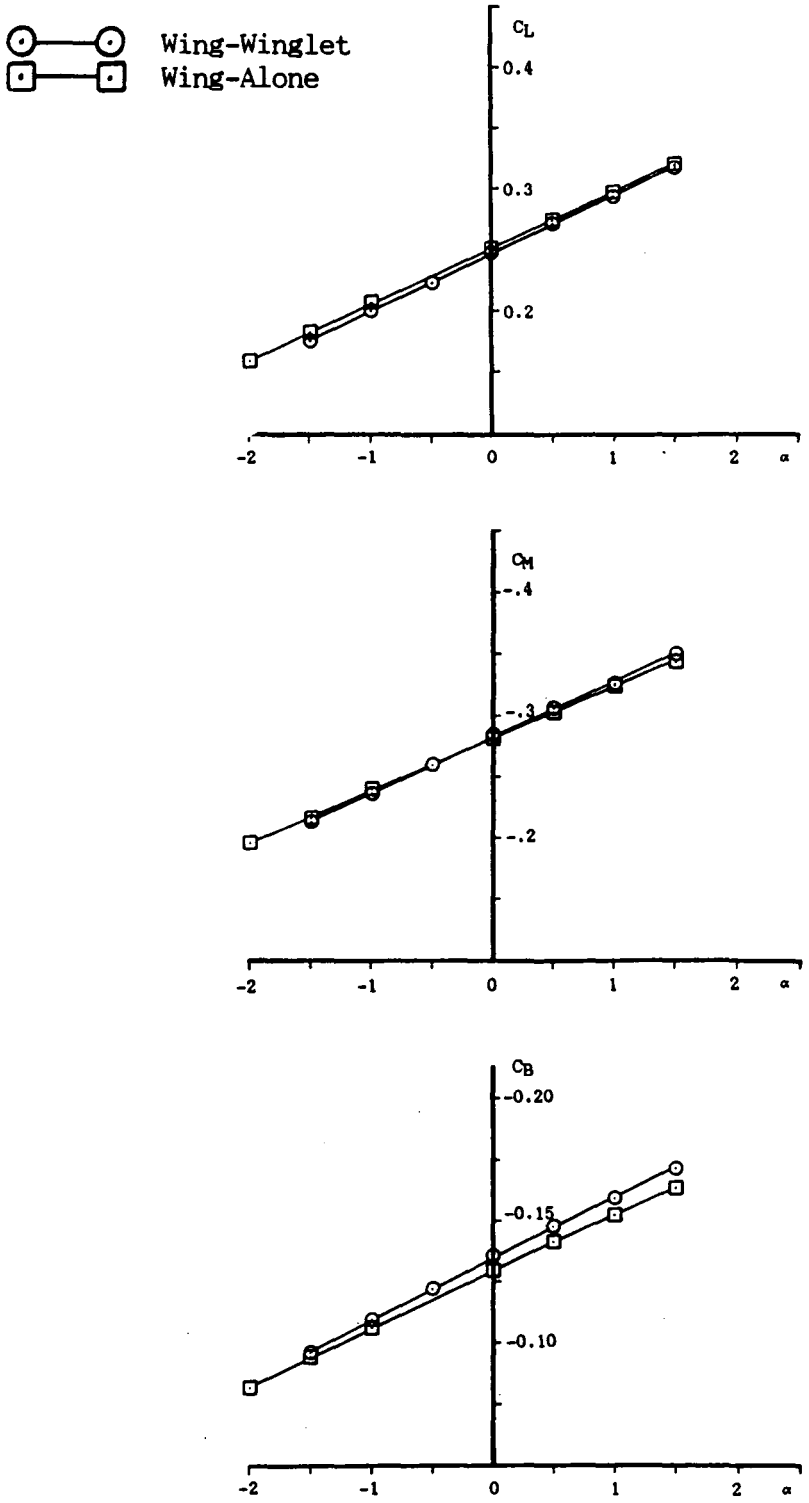

Fig. 25. Predicted performance of wing-alone and wing-winglet A at M = 0.75; 300 iterations with boundary layer interaction:

a) C_L versus α
b) C_m versus α
c) C_B versus α

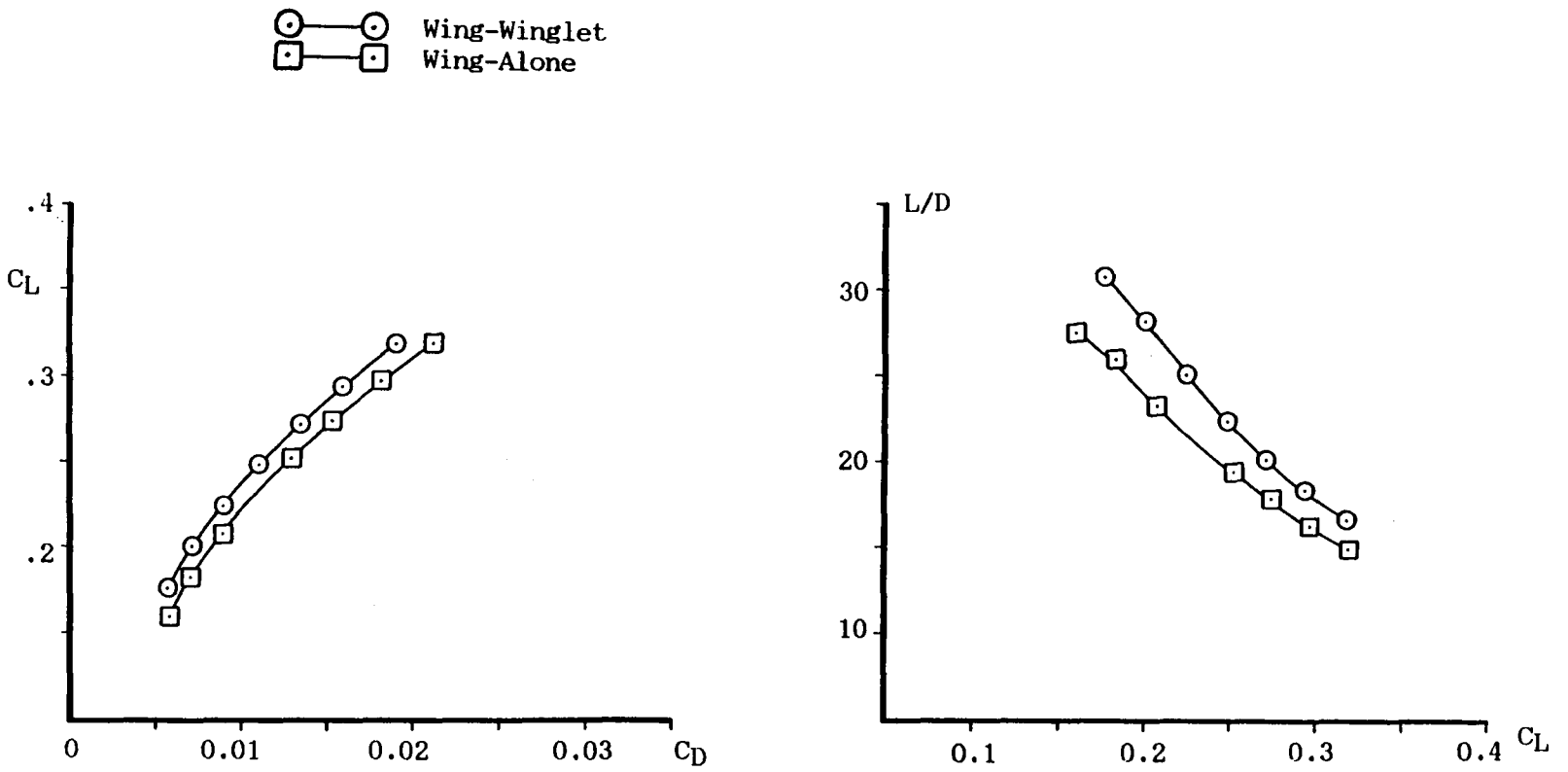

Fig. 25. Predicted performance of wing-alone and wing-winglet A at M = 0.75; 300 iterations with boundary layer interaction:
d) C_L versus C_D
e) L/D_{tot} versus C_L

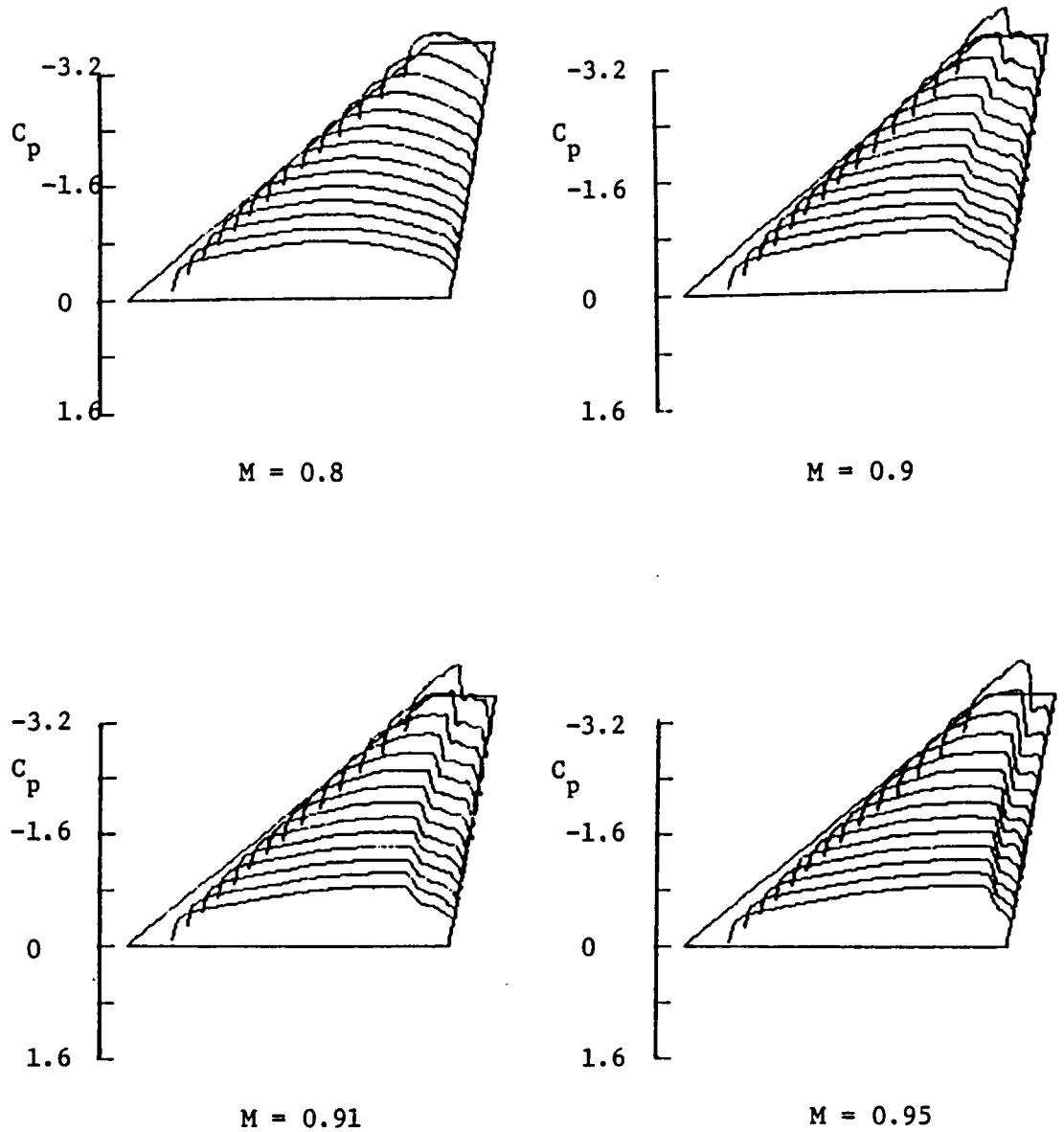

Fig. 26. Calculated upper surface pressure coefficient distributions for wing of wing-winglet A at $C_L \cong 0.2$, versus Mach number.

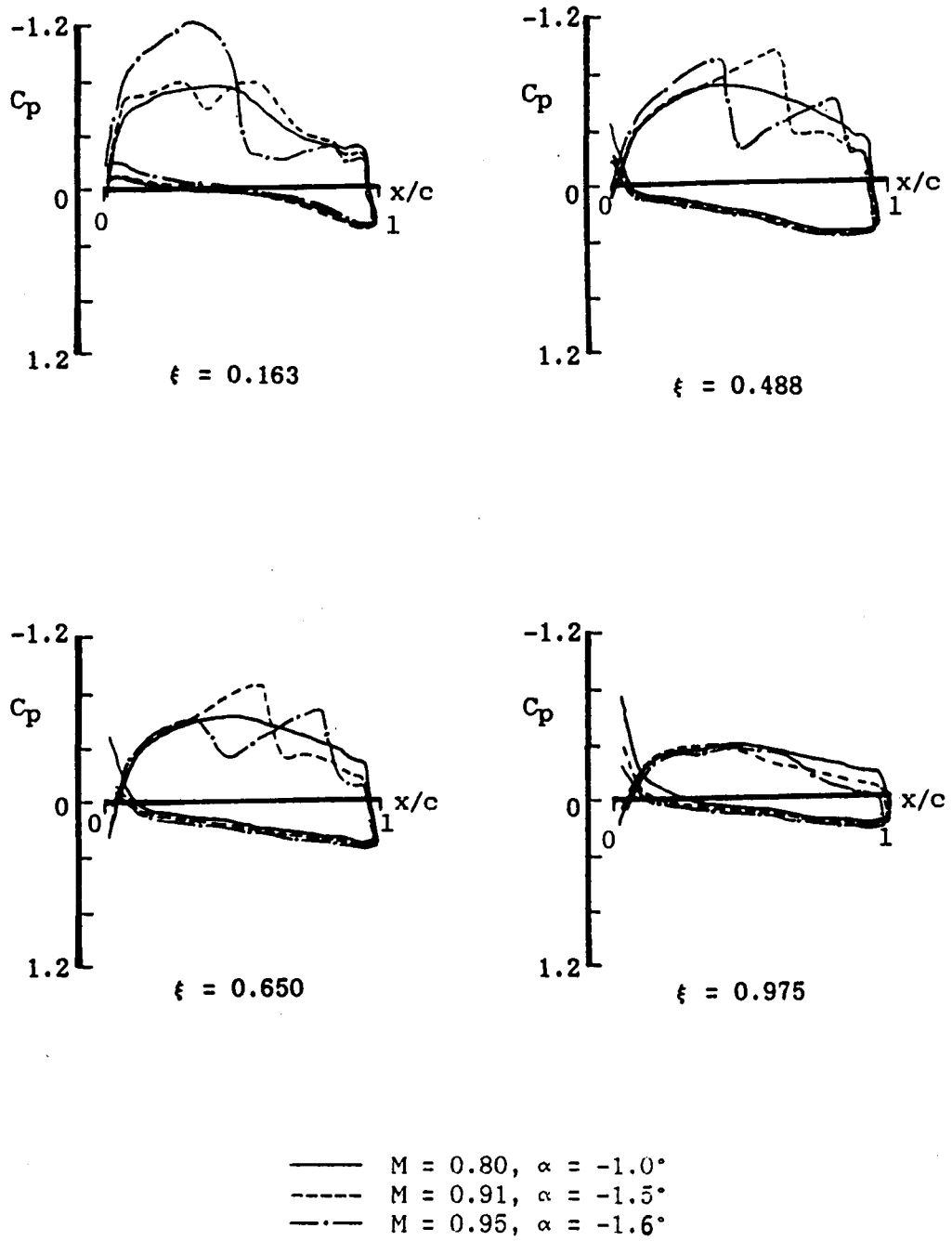

Fig. 27. Calculated winglet pressure coefficient distributions for wing A fitted with 0.15(b/2) winglet at $C_L \cong 0.2$, versus Mach number.

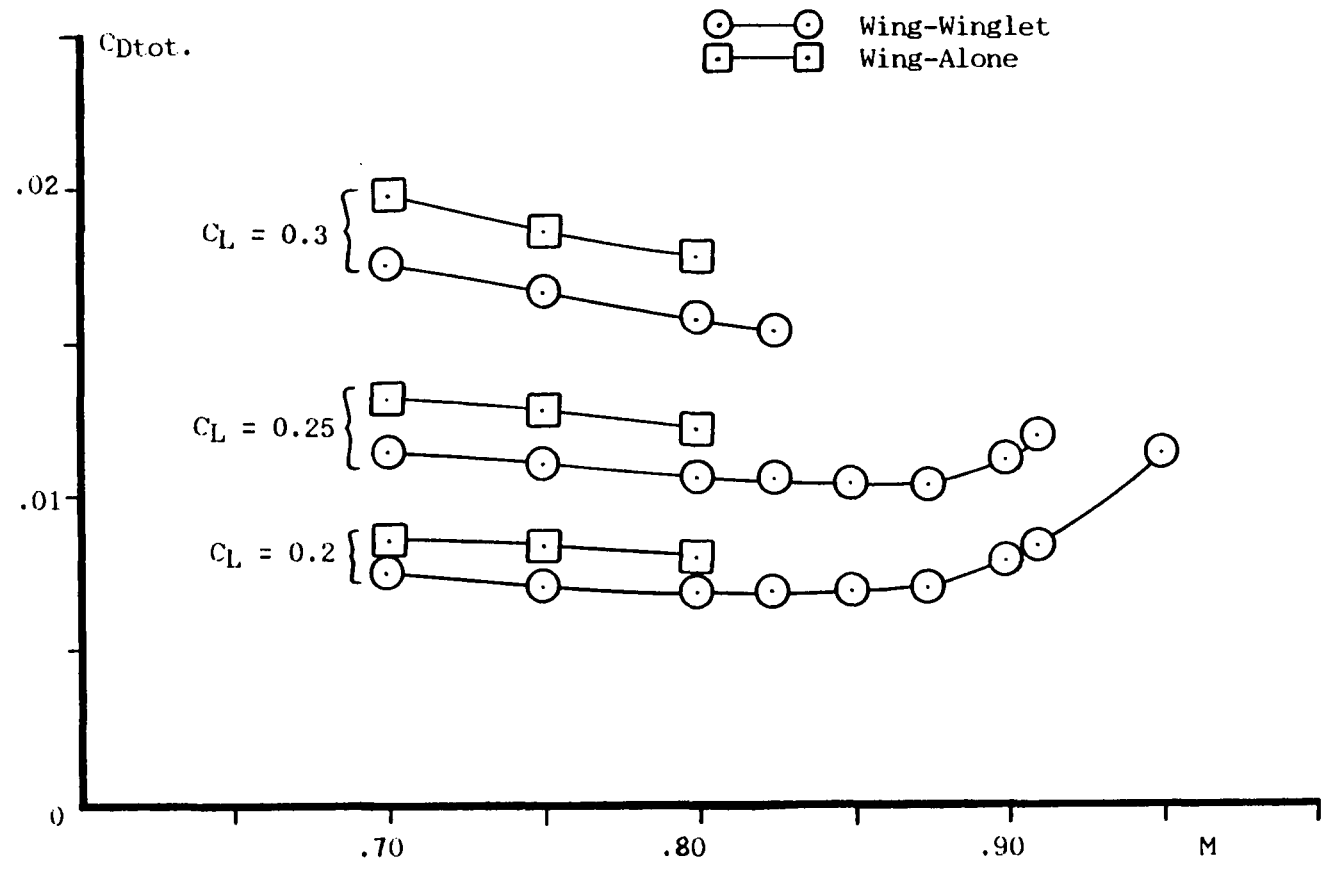

Fig. 28. Calculated drag coefficient versus Mach number at various C_L values; wing-alone and wing-winglet A; 300 iterations with boundary layer interaction.

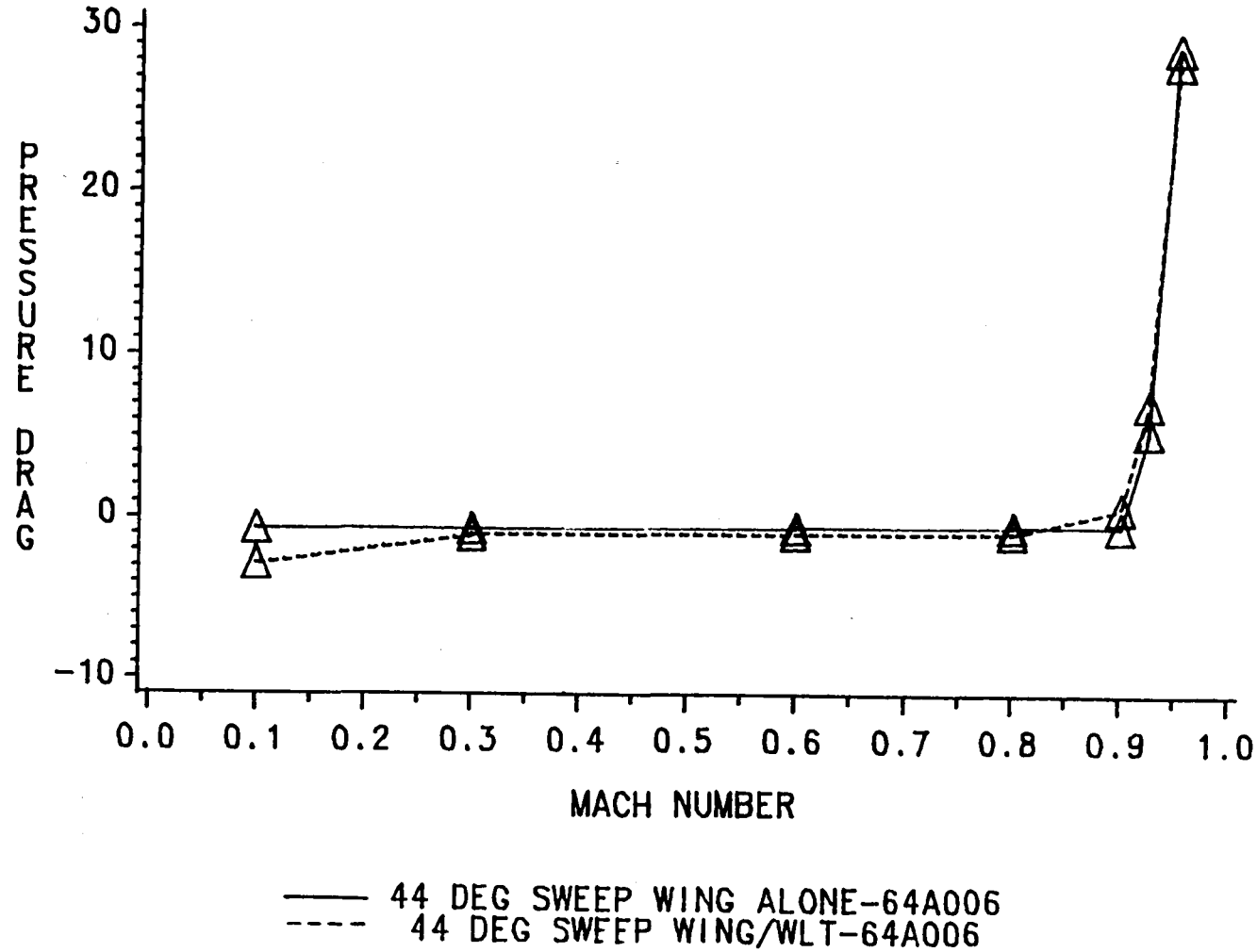

Fig. 29. Calculated pressure drag coefficient at $C_L = 0$ for $A = 2.5$, $\Lambda = 44°$, $\lambda = 0.2$ wing-alone and wing-winglet, without camber or twist.

NASA
National Aeronautics and Space Administration

Report Documentation Page

1 Report No	2 Government Accession No	3 Recipient's Catalog No
NASA CR-4174		

4 Title and Subtitle

Theoretical/Numerical Study of Feasibility of Use of Winglets on Low Aspect Ratio Wings at Subsonic and Transonic Mach Numbers To Reduce Drag

5 Report Date

August 1988

6 Performing Organization Code

7 Author(s)

John M. Kuhlman, Paul Liaw, and Michael J. Cerney

8 Performing Organization Report No

10 Work Unit No

505-60-21-02

9 Performing Organization Name and Address

West Virginia University
Department of Mechanical and Aerospace Engineering
Morgantown, WV 26506-6101

11 Contract or Grant No

NAG1-625

13 Type of Report and Period Covered

Contractor Report
Jan. 1986-Aug. 1987

12 Sponsoring Agency Name and Address

National Aeronautics and Space Administration
Langley Research Center
Hampton, VA 23665-5225

14 Sponsoring Agency Code

15 Supplementary Notes

Langley Technical Monitor: James M. Luckring

16 Abstract

A numerical design study has been conducted to assess the drag reduction potential of winglets installed on a series of low aspect ratio wings at a design point of $M = 0.8$, $C_L = 0.3$. Wing-winglet and wing-alone design geometries have been obtained for wings of aspect ratios between 1.75 and 2.67, having leading edge sweep angles between 45° and 60°. Winglet length has been fixed at 15% of wing semispan.

To assess the relative performance between wing-winglet and wing-alone configurations, the PPW nonlinear extended small disturbance potential flow code has been utilized. This model has proven in the present study to yield plausible transonic flow field simulations for the series of low aspect ratio configurations selected. Predicted decreases in pressure drag coefficient for the wing-winglet configurations relative to the corresponding wing-alone planform are about 15% at the design point. Predicted decreases in wing-winglet total drag coefficient are about 12%, relative to the corresponding wing-alone design. Longer winglets (25% of the wing semispan) yielded decreases in the pressure drag of up to 22% and total drag of up to 16.4%. These predicted drag coefficient reductions are comparable to reductions already demonstrated by actual winglet designs installed on higher aspect ratio transport type aircraft.

17 Key Words (Suggested by Author(s))

Aerodynamics
Transonic Flow
Induced Drag Reduction
Low Aspect Ratio
Winglets

18 Distribution Statement

Unclassified - Unlimited

Subject Category 02

19 Security Classif (of this report)	20 Security Classif (of this page)	21 No of pages	22 Price
Unclassified	Unclassified	88	A05

For sale by the National Technical Information Service, Springfield, Virginia 22161-2171

End of Document